Interfacing thermal atoms with integrated photonic waveguides

Ralf Ritter

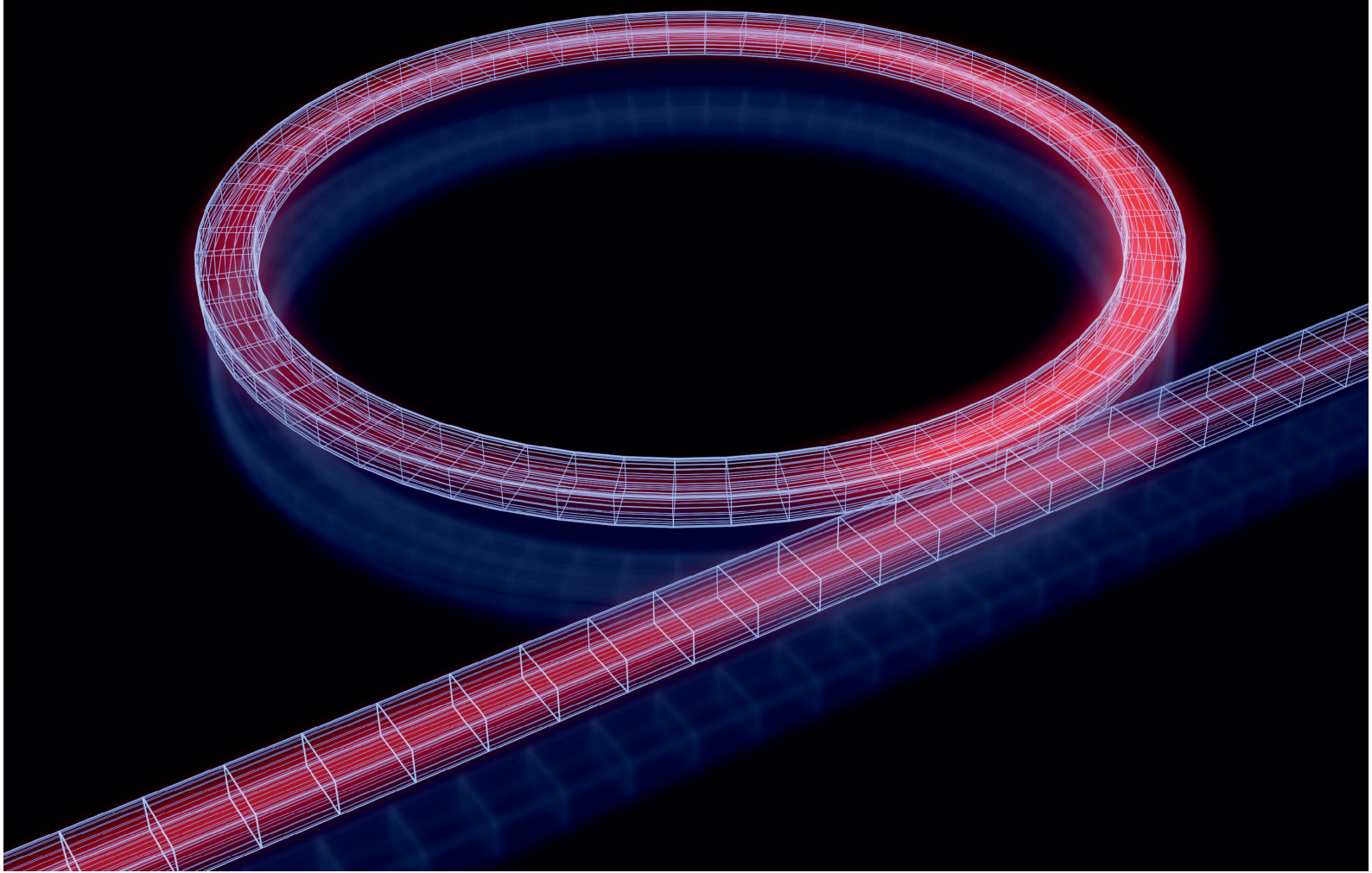

Interfacing thermal atoms with integrated photonic waveguides

Von der Fakultät Mathematik und Physik der Universität Stuttgart
zur Erlangung der Würde eines Doktors der
Naturwissenschaften (Dr. rer. nat.) genehmigte Abhandlung

vorgelegt von

Ralf Ritter

aus Hechingen

Hauptberichter:	Prof. Dr. Tilman Pfau
Mitberichter:	Prof. Dr. Harald Giessen
Prüfungsvorsitzender:	Prof. Dr. Hans Peter Büchler
Tag der mündlichen Prüfung:	12. April 2018

5. Physikalisches Institut
Universität Stuttgart

2018

Contents

List of publications

In the framework of this thesis, I prepared the following publications:

- R. Ritter, N. Gruhler, H. Dobbertin, H. Kübler, S. Scheel, W. Pernice, T. Pfau and R. Löw, Coupling thermal atomic vapor to slot waveguides, *Phys. Rev. X* **8**, 021032 (2018).
- R. Ritter, N. Gruhler, W. Pernice, H. Kübler, T. Pfau and R. Löw, Coupling thermal atomic vapor to an integrated ring resonator, *New J. Phys.* **18**, 103031 (2016).
- R. Ritter, N. Gruhler, W. Pernice, H. Kübler, T. Pfau and R. Löw, Atomic vapor spectroscopy in integrated photonic structures, *Appl. Phys. Lett.* **107**, 041101 (2015).

Zusammenfassung

Mit Gas befüllte Glaszellen sind seit Beginn der experimentellen Atomphysik im Einsatz der Forschung und finden heutzutage in modernen Experimenten noch genauso ihre Verwendung. Unser Wissen über die Elektronenstruktur der Atome und wie diese mit Licht wechselwirken resultiert zu einem großen Teil aus Untersuchungen von Absorptions- und Emissionsspektren, welche häufig anhand von Dampfzellen aufgenommen wurden. Wenn es darum geht, sehr präzise Messungen unter gut kontrollierten Bedingungen zu machen, sind kalte Atome das Mittel der Wahl. Jedoch sind hierfür komplexe experimentelle Aufbauten notwendig, welche einen kompletten optischen Tisch, oder sogar mehr beanspruchen. Im Gegensatz dazu sind Dampfzellen ohne großen Aufwand herzustellen, sind kompakt, kostengünstig, einfach zu verwenden und verbrauchen vergleichsweise wenig Energie. Dies macht sie besonders interessant für praktische Anwendungen. Im Vergleich zu Systemen basierend auf Festkörpern haben Atome den großen Vorteil, dass sie wohldefinierte und schmale Übergangsfrequenzen besitzen, wodurch reproduzierbare und akkurate Messungen ermöglicht werden. Insbesondere Alkalimetalle, wie zum Beispiel Rubidium (Rb), sind eine günstige Atomsorte für solche Messungen, da diese eine recht einfache Elektronenstruktur mit einem einzelnen Valenzelektron, vorteilhafte Übergangswellenlängen und langlebige Hyperfein-Grundzustände aufweisen. Zudem bieten diese schon bei moderaten Temperaturen (z.B. Raumtemperatur) einen brauchbaren Dampfdruck.

Tatsächlich nutzen wir in unserem Alltag bereits indirekt Technologien die auf Alkali Dampfzellen basieren: Rb-Atomuhren finden sich aufgrund ihrer kompakten Größe und ihres sparsamen Energieverbrauchs an Bord der GPS-Satelliten [1] und der Europäischen Galileo-Navigationssatelliten [2] und werden außerdem als genaue Zeit- und Frequenzreferenz in Sendeanlagen für Mobiltelefone und Rundfunk eingesetzt [3]. Dabei wird die Zeitreferenz durch Messung atomarer Übergangsfrequenzen abgeleitet, was sehr exakt bewerkstelligt werden kann. Aus diesem Grund, und weil bereits geringste Störungen die Energiestruktur der Atome beeinflussen, können Dampfzellen als sehr empfindliche Sensoren dienen. Als Beispiele seien genannt: die Messung elektrischer Felder [4], von Mikrowellen [5, 6], sogar mit räumlicher Auflösung [7, 8] und von Magnetfeldern [9, 10] mit medizinischer Anwendung im Bereich der Magnetokardiografie [11–13] sowie der Magnetoenzephalographie [14–17]. Neben der Messung von elektromagnetischen Feldern können Dampfzellen ebenfalls als Gassensoren [18] und als Gyroskope verwendet werden [19, 20]. Im Rahmen der Quanteninformationsverarbeitung könnte man sich Dampfzellen als mögliche Bausteine in einem skalierbaren

Quantennetzwerk vorstellen [21]. Hierfür wurde eine auf thermischen Atomen basierende Einzelphotonenquelle vorgeschlagen [22] und vor kurzem in unserem Labor erfolgreich demonstriert. Ein dazu kompatibler und gut funktionierender Quantenspeicher kann ebenfalls mit Dampfzellen realisiert werden [23–25]. Die enorme Bandbreite an möglichen Anwendungen umfasst zudem optische Bauteile, wie zum Beispiel einen optischen Isolator [26], oder extrem schmale Bandpassfilter [27–29], welche von Natur aus auf die atomaren Übergangsfrequenzen abgestimmt sind.

In den letzten Jahren wurde ein beträchtlicher Aufwand betrieben, um Dampfzellen sowohl in ihrer Gesamtgröße [30–32] als auch deren Einschlussvolumina [33–35] zu miniaturisieren. Insbesondere mikrostrukturierte Zellen bieten eine geringe Verlustleistung, eine geringe Größe (und dadurch ein erhöhtes Auflösungsvermögen für Sensoren) und eine Integrierung auf Waferebene, wodurch eine Massenproduktion und dadurch Kostenersparnis möglich wird. Diese Vorgehensweise hat die Herstellung extrem kompakter Atomuhren [30, 36] und Magnetometer [37–39] ermöglicht. Eventuell sind damit auf das Internationale Einheitensystem (SI) zurückführbare Referenzen für mehrere Basiseinheiten auf einem einzigen Chip realisierbar [40].

Ein sogar noch viel höheres Maß der Miniaturisierung und Integrierung kann durch die Verheiratung von Dampfzellen und photonischer Schaltkreise erreicht werden. Um dieses Thema geht es in der vorliegenden Arbeit. Ein photonischer Schaltkreis besteht aus mehreren optischen Bauteilen auf einem winzigen Chip. Dies ist vergleichbar mit integrierten elektronischen Schaltkreisen (ICs), allerdings werden Signale hier durch Licht anstatt eines elektrischen Stroms übertragen und die einzelnen Komponenten des photonischen Schaltkreises sind untereinander mit optischen Wellenleitern anstelle von Leiterbahnen verbunden. Durch das evaneszente Feld, welches durch Totalreflexion in diesen Wellenleitern entsteht, ist es möglich, Atome die sich innerhalb eines Abstandes der Größenordnung $\lambda/2\pi$ vom Wellenleiter befinden, an die im Wellenleiter geführte Mode zu koppeln. Hierbei ist λ die Wellenlänge des geführten Lichts. Neben den Untersuchungen die in dieser Doktorarbeit vorgestellt werden, wird derselbe Ansatz auch von Prof. Uriel Levy in Jerusalem verfolgt, welcher einen ersten Machbarkeitsbeweis geliefert [41] und weitere Folgestudien durchgeführt hat [42–44]. Die Realisierung eines solchen Hybridsystems birgt ein enormes Potential für praktische Anwendungen, aber auch für grundlegende Untersuchungen der Wechselwirkung zwischen Licht und Materie. Einige Vorzüge dieses Ansatzes werden im Folgenden besprochen.

Stellen Sie sich einen herkömmlichen Spektroskopie Aufbau vor, in dem Laserstrahlen durch Spiegel, Linsen und elektro- oder akustooptische Modulatoren manipuliert, und anschließend von Detektoren erfasst werden. All diese Komponenten sind üblicherweise auf einem massiven vibrationsisolierten optischen Tisch aufgebaut und nehmen dort recht viel Platz ein. Dieselben Komponenten können jedoch auch in einem photonischen Schaltkreis auf viel kleinerem Raum realisiert werden [45], samt Lichtquellen, z.B. in Form eines DFB-Lasers [46, 47] oder Oberflächenemitters (VCSEL) [48, 49] welcher durch Flip-Chip-Montage eingebaut wird. Auch Lichtdetektoren [50, 51] und sogar

Heizelemente für die Regelung des Dampfdrucks können integriert werden [30, 52]. Dadurch, dass das Licht in Wellenleitern geführt wird, sind diese Elemente nicht vibrationsanfällig und die optische Justage ist von sich aus perfekt. Das schnell wachsende Gebiet der Mikro- und Nanophotonik, sowie hoch entwickelte Fabrikationsprozesse in der Halbleiterindustrie ermöglichen es, in Massenproduktion eine Vielzahl an Bauteilen auf einem einzigen Chip unterzubringen. Optische Chips sind ohne weiteres mit dem Glasfaser-Telekommunikationsnetzwerk kompatibel, wo eine auf Atomdampf basierende Frequenzreferenz möglicherweise dazu verwendet werden könnte, um die Vermischung von unabhängigen Trägerfrequenzen beim Dichte-Wellenlängen-Multiplexing (engl. *Dense Wavelength Division Multiplexing*, DWDM) zu verhindern [53]. Einige der vorhin erwähnten auf Dampfzellen basierenden Anwendungen könnten auch mit dem vorgeschlagenen Hybridsystem mit noch kompakteren Designs umgesetzt werden, wodurch der Leistungsverbrauch und die Mobilität nochmals verbessert werden. Dies ist insbesondere für Sensor- und Referenzanwendungen interessant, welche sich dadurch in Handgeräten integrieren ließen. Da die Atome um den Wellenleiter auf einer Sub-Mikrometer-Skala sondiert werden, wäre es vielleicht sogar möglich, die räumliche Auflösung solcher Sensoren zu erhöhen. In dieser Hinsicht wurden im Bereich der Magnetometrie beispielsweise Untersuchungen mit dem evaneszenten Feld durch Totalreflexion an einem Prisma unternommen [54]. Es sei darauf hingewiesen, dass die Bewegung der Atome in einem thermischen Gas zu einer Doppler- und Durchflugsverbreiterung führt und die Energiestruktur der Atome in der Nähe eines Wellenleiters durch Wechselwirkung mit der Oberfläche verschoben wird. Diese Effekte sollten berücksichtigt werden, da sie die Präzision von potenziellen Sensoren und Atomuhren einschränken. Jedoch wird die erreichbare Präzision für einige Anwendungen sicherlich gut genug sein, wenn die Vorteile dieses Konzepts überwiegen.

Durch den Einsatz von Mikro- und Nanostrukturen ist es außerdem möglich, das an die Atome koppelnde Lichtfeld maßzuschneidern. Die geringe Modenfläche des evaneszenten Felds bewirkt eine effiziente Atom-Licht-Wechselwirkung, welche nochmals verstärkt werden kann, indem man das Licht in resonanten Kavitäten einfängt. In diesem Fall kann das Atom mit dem zirkulierenden Photon mehrfach wechselwirken. Aus diesem Konzept ist das Gebiet der Cavity-Quantenelektrodynamik (QED) entstanden [55–57]. Die Stärke der Wechselwirkung hängt außerdem von der Größe des Modenvolumens des Resonators ab: je kleiner das Modenvolumen, desto konzentrierter ist die Energie eines Photons innerhalb der Mode und umso stärker die Wechselwirkung. Nanophotonische Resonatoren verfügen über ein extrem kleines Modenvolumen und können skalierbar hergestellt werden, wodurch sie sich als Kandidaten für ein großangelegtes Quantennetzwerk auszeichnen [58–60]. Deshalb wurde eine Vielzahl von Experimenten mit Mikroresonatoren durchgeführt. Auch wenn die Kopplung von thermischen Cäsium-Atomen an Mikrokügelchen aus Quarzglas schon frühzeitig gezeigt wurde [61], konnte das Regime der sogenannten starken Kopplung nur mit ultrakalten Atomen in Verbindung mit nanophotonischen Resonatoren [62, 63], oder Wellenleitern basierend auf photonischen Kristallen, erreicht werden [64]. Dass eine starke Kopplung

mit thermischen Atomen bisher nicht erreicht wurde, liegt an der bereits angesprochenen Bewegung der Atome. Eine extrem hohe Kopplungsstärke wäre notwendig, um die Verluste durch die Bewegung zu kompensieren. In dieser Arbeit werden wir allerdings eine Abschätzung vornehmen in der wir zeigen, dass es mit einem geeigneten Resonator-Design möglich sein könnte, die notwendigen Bedingungen zu erfüllen. Sollte dem tatsächlich so sein, wäre dies ein wichtiger Schritt in Richtung eines skalierbaren Quantennetzwerks, da eine Miniaturisierung eines Aufbaus für kalte Atome sicherlich nicht weniger anspruchsvoll wäre. Ungeachtet dessen, ob das Regime der starken Kopplung erreicht werden kann oder nicht, würde jede Verbesserung der Kopplungsstärke zu einer Effizienzsteigerung führen und damit die Leistungsfähigkeit von potenziellen Geräten erhöhen.

In einem ganz anderen Zusammenhang könnte die Fähigkeit, Licht mit Wellenleitern auf kleine Volumina zu beschränken dazu genutzt werden, um die Dipol-Dipol-Wechselwirkung zwischen thermischen Atomen zu untersuchen. Dieses Thema hat vor kurzem wieder erhöhte Aufmerksamkeit erlangt [35, 65, 66] und scheint noch nicht vollkommen verstanden zu sein [67, 68]. Weitere Erkenntnisse über die zugrundeliegende Physik könnten dadurch erlangt werden, dass man die Dimensionalität und dadurch die Komplexität dieses Problems reduziert. Erste Schritte in diese Richtung wurden bereits durch den Einschluss von atomaren Gasen in Nanozellen unternommen [35, 68], welche ein quasi-zweidimensionales System darstellen. Die nächste Stufe könnte erreicht werden, indem man sich die transversale Beschränkung der Wellenleitermode auf einen Bereich der kleiner ist als die Wellenlänge zu eigen macht. Da die Lichtausbreitung entlang des Wellenleiters invariant ist, stellt dies ein quasi-eindimensionales System dar. Sogenannte Slot-Wellenleiter [69], bei denen die Mode in einen schmalen Spalt zwischen zwei rechteckige Wellenleiter gequetscht ist, wären hierfür besonders gut geeignet. Außerdem kann in Dampfzellen die Atomdichte einfach durch Temperaturänderung über einen großen Bereich eingestellt werden.

In dieser Arbeit wird die eben vorgestellte Zusammenführung von thermischen Atomen und photonischen Wellenleiterstrukturen untersucht. Dies wurde durch eine enge Zusammenarbeit mit Prof. Wolfram Pernice am KIT und der Universität Münster ermöglicht, wo die photonischen Strukturen entworfen und hergestellt wurden. Die optischen Chips, auf denen sich eine Vielzahl dieser auf Siliziumnitrid basierenden Strukturen befinden, wurden durch anodisches Bonden in Dampfzellen integriert. Die Strukturen befinden sich dabei auf der Innenseite der Zelle, sodass sie von Rb-Atomen umgeben sind. Um gezielt Bereiche zu definieren, in denen die Atome mit dem Feld der Wellenleiter wechselwirken können, ist der Rest des Chips mit einer Schicht aus Siliziumdioxid maskiert. Weiterhin sind die Strukturen mit Gitterkopplern ausgestattet, worüber Licht in die Bauteile ein- und wieder ausgekoppelt wird. Im Laufe dieser Doktorarbeit wurden unterschiedliche photonische Bauteile und deren Zusammenspiel mit Rb-Atomen untersucht. Diese werden nun im Einzelnen vorgestellt und die jeweils erzielten Ergebnisse zusammengefasst.

Um ein Gefühl dafür zu bekommen, wie die Spektroskopie von thermischen Atomen mit integrierten Strukturen funktioniert und um diese zu charakterisieren, wurden zunächst Transmissionsmessungen mit einfachen rechteckigen Wellenleitern durchgeführt. Viele der hierbei gemachten Beobachtungen treffen auch auf die später besprochenen Bauteile zu. Spektren der D_2-Linie von Rb haben hierbei gezeigt, dass die geführte Mode über das evaneszente Feld von den Atomen absorbiert werden kann. Diese weisen gegenüber Spektren aus herkömmlicher Spektroskopie eine zusätzliche Lininenverbreiterung auf. Die Ursachen hierfür liegen zum einen in der erhöhten Dopplerverbreiterung aufgrund des größeren Wellenvektors der geführten Mode, zum anderen verursacht die kurze Wechselwirkungszeit der Atome auf ihrem Weg durch das evaneszente Feld eine Durchflugsverbreiterung. Das gesamte Spektrum ist außerdem aufgrund der Casimir-Polder-Wechselwirkung der Atome mit den dielektrischen Oberflächen rotverschoben. Dies ist eine Konsequenz davon, dass die Atome so nahe am Wellenleiter abgefragt werden. Die Transmission durch einen von Atomdampf umgebenen Wellenleiter lässt sich numerisch mit der effektiven Suszeptibilität-Methode berechnen, welche wir aus der selektiven Reflexionsspektroskopie übernommen, und auf unsere Gegebenheiten angepasst haben. Hierbei wird die Propagation durch einen Wellenleiter simuliert, welcher von einem Medium mit einem komplexen Brechungsindex umgeben ist, der durch die Eigenschaften des Rb-Dampfs und die auftretenden Effekte der atomaren Bewegung bestimmt ist. Auf diese Weise konnten wir die Spektren aus dem Wellenleiter mit ausgezeichneter Übereinstimmung reproduzieren. Nachdem der optische Chip dem Rb-Dampf ausgesetzt war, haben wir frühzeitig eine Verschlechterung der Wellenleitertransmission festgestellt. Dies ist sehr wahrscheinlich auf eine Ablagerung von metallischem Rb auf den Wellenleitern zurückzuführen. Eine zusätzliche dünne Schutzschicht aus Saphir konnte bei weiteren Chips eine Verbesserung bewirken, jedoch war selbst damit noch eine verbleibende Abschwächung feststellbar.

Neben den absorptiven Eigenschaften der Atome haben wir deren Auswirkungen auf die Phase der geführten Mode untersucht. Um diese zu messen, verwendeten wir ein integriertes Mach-Zehnder-Interferometer (MZI), bestehend aus zwei Wellenleiterarmen, von denen einer mit Siliziumdioxid bedeckt und der andere für die Atome zugänglich war. Die hiermit aufgenommenen Spektren zeigen eindeutig dispersive Merkmale, welche durch den Realteil der Suszeptibilität des Atomdampfs bestimmt sind. Auch diese Daten konnten wieder mit sehr guter Übereinstimmung durch das Modell der effektiven Suszeptibilität erklärt werden. Dadurch war es uns möglich, den durch die Atome verursachten Phasenschub zu bestimmen.

Im nächsten Schritt untersuchten wir die Wechselwirkung von thermischen Rb-Atomen mit photonischen Ring-Resonatoren im Hinblick auf mögliche skalierbare Atom-Resonator-Systeme. Unsere ersten Versuche waren aufgrund der angesprochenen Transmissionsverluste erfolglos, da diese so hoch waren, dass die Ringresonanzen stark verbreitert und dadurch nicht beobachtbar waren. Erst durch die zusätzliche Saphir Schutzschicht gelang dies. Durch Veränderung der Chiptemperatur konnten wir die Frequenz ei-

ner Ringresonanz thermisch durchstimmen, so dass diese mit der Resonanzfrequenz der Rb-D_2-Linie in Übereinstimmung war. Die Wechselwirkung der Atome mit dem Ringresonator wurde somit ausgiebig charakterisiert und konnte wieder hervorragend durch das Modell der effektiven Suszeptibilität reproduziert werden. Zusätzlich wurde das Sättigungsverhalten der Atome untersucht, wenn diese mit einem resonanten Ring wechselwirken. Jedoch wurde hierbei festgestellt, dass die Sättigungsschwelle bei den gleichen Eingangsleistungen erreicht wird, wie auch bei einem nicht resonanten Ring, sprich im Zuleitungswellenleiter. Dies lässt sich zum einen durch die verbleibenden Verluste aufgrund von Rb-Atomen auf der Oberfläche erklären, zum anderen durch das relativ große Modenvolumen dieses Resonators, welcher deshalb so groß gewählt wurde, dass dieser mit vernünftigen Temperaturen auf die Atomresonanz gestimmt werden kann. In diesem Zusammenhang diskutierten wir auch die Verwendbarkeit dieser Resonatoren im Beriech der Cavity-QED und erörtern die Realisierbarkeit einer starken Kopplung von thermischen Atomen an nanophotonische Resonatoren. Hierbei stellte sich heraus, dass das extrem geringe Modenvolumen eines photonischen Kristallresonators eine Kopplungsstärke bietet, welche die Verluste durch die Bewegung der Atome übertreffen könnte.

Die Untersuchung der vorhin kurz angesprochenen Slot-Wellenleiter stelle sich als recht komplex dar, dadurch aber auch als extrem lehrreich. Hierfür wurden Wellenleiter mit unterschiedlicher Slotbreite entworfen, mit der Absicht, die Intensität der Mode in den jeweiligen Slots und damit die Kopplung an die Atome zu variieren. Aus den Transmissionsspektren der einzelnen Bauteile wurden jeweils die Linienverschiebung, Linienbreite und die optische Dicke bestimmt, welche einen anderen Verlauf aufwiesen als ursprünglich erwartet. Um das tatsächliche Verhalten zu verstehen wurde eine Monte-Carlo-Simulation entwickelt, welche die Bewegung der einzelnen Atome um die spezifische Wellenleitergeometrie berücksichtigt. Ebenfalls wurden die Potentiale durch die Wechselwirkung der Atome mit den Oberflächen und die veränderte Zerfallsrate der Atome berücksichtig. Es wurden die Abmessungen der Wellenleiterquerschnitte miteinbezogen, welche durch Elektronenmikroskopaufnahmen bestimmt wurden, nachdem der Chip von der Zelle entfernt und mit einem fokussierten Ionenstrahl Schnitte in die Wellenleiter gemacht wurden. Hierbei stellten wir fest, dass die ganz schmalen Slots gar nicht und die etwas breiteren Slots nur teilweise entwickelt waren. Ausschließlich die Bauteile mit großer Slotbreite waren vollständig entwickelt. Für die Bauteile die keinen Slot aufweisen und die komplett entwickelten Slots konnte eine gute Übereinstimmung zwischen Experiment und Monte-Carlo-Simulation erreicht werden. Allerdings zeigen die unvollständig entwickelten Slots teils erhebliche Abweichungen. Gründe hierfür werden in der Arbeit ausgiebig diskutiert, aber die Ursache kann letztendlich aufgrund vieler Unsicherheiten nicht dingfest gemacht werden. Dies liegt unter anderem daran, dass wir nicht die vollständige Information über die Geometrie der gesamten Bauteile und deren Oberflächenbeschaffenheit haben. Ebenso wenig ist die genaue Adsorptions- und Desorbtionsdynamik bekannt. Es stellt sich außerdem die Frage, welche Rolle Rb-Abscheidungen auf der Oberfläche der Wellenleiter spielen, in welcher Form diese vor-

liegen, wie diese die Mode und die Casimir-Polder-Potentiale beeinflussen und ob diese Dipole ausbilden, welche durch elektrische Felder die Atome stören. Mit zweien dieser Slot-Wellenleiter untersuchten wir zudem die gegenseitige Wechselwirkung der Atome bei hohen Dichten. Dabei wurden eine Linenverbreiterung und Linienverschiebung, die linear mit der Dichte zunehmen, gemessen. Die Verbreiterung lässt sich durch den Effekt der Selbstverbreiterung erklären. Die Größe der Verschiebung kann allerdings mit der gängigen Theorie nicht erklärt werden und bedarf weiterer Studien. Dies ist möglicherweise ein weiterer Hinweis auf eine nicht vollständige Theorie, wie weiter oben bereits erwähnt wurde.

Durch eine Zweiphotonenanregung zum $5D_{3/2}$ Zustand von Rb haben wir nahezu Dopplerfreie Spektren mit einem integrierten photonischen Schaltkreis gemessen. Die Verringerung der Dopplerbreite war hierbei durch die fast gleiche Wellenlänge der in gegengesetzter Richtung propagierenden Moden gegeben. Somit konnte eine durch Durchflugsverbreiterung dominierte Linienbreite von $\sim 2\pi \times 860\,\mathrm{MHz}$ im Vergleich zur Dopplerverbreiterten Linie mit $\sim 2\pi \times 1300\,\mathrm{MHz}$ bestimmt werden. Ein weiterer Einfluss auf die Linienbreite ist durch die Atom-Oberflächenwechselwirkung gegeben, welche die Linie asymmetrisch verzerrt. Diese Wechselwirkung ist bei der Spektroskopie des $5D_{3/2}$ Zustands größer als beim ansonsten untersuchten $5P_{3/2}$ Zustand, was sich auch in einer erhöhten Rotverschiebung widerspiegelt. Die asymmetrische Linienform dieser Zweiphotonenspektren konnte durch eine Monte-Carlo-Simulation unter Einbeziehung der Casimir-Polder-Potentiale der beteiligten Niveaus angemessen reproduziert werden. Lediglich die absolute Rotverschiebung war in der Simulation höher als in der Messung.

Für den weiteren Verlauf dieses Experiments ist es vorgesehen, die Wellenleiter künftig aus Silizium zu fertigen, welches einige Vorteile mit sich bringt. Beispielsweise gibt es eine Vielzahl an Bauteilen von extrem hoher Güte, da im Gebiet der Photonik schon seit längerer Zeit mit Silizium gearbeitet wird. Um diese zusammen mit Rb verwenden zu können, ist ein anderes Anregungsschema als bisher notwendig, da Silizium für die D_2-Wellenlänge von Rb nicht transparent ist. Deshalb wird der $5P_{3/2}$ Zustand mit einem Laserstrahl gepumpt, während über eine geführte Mode bei 1529 nm die Atome auf dem $5P_{3/2} \rightarrow 4D_{5/2}$ Übergang abgefragt werden. Diese Wellenlänge ist direkt mit der vorhandenen Telekommunikations-Infrastruktur kompatibel, was für spätere Anwendungen extrem vorteilhaft ist. Außerdem kann mit Silizium durch den größeren Brechungsindexkontrast eine höhere Intensität der geführten Mode erreicht werden, was in Verbindung mit dem ebenfalls größeren Dipolmatrixelement des $5P_{3/2} \rightarrow 4D_{5/2}$ Übergangs eine erhöhte Kopplungsstärke verspricht. Weiterhin sind die Rb Anhaftungen auf Silizium und die daraus resultierenden Transmissionsverluste möglicherweise nicht so schwerwiegend wie im Falle von Siliziumnitrid. Diese Problematik sollte im Allgemeinen besser aufgeklärt werden, insbesondere im Hinblick auf die Fertigung von Resonatoren hoher Güte. Um die Wechselwirkungszeit der Atome zu verlängern könnten möglicherweise Puffergase eingesetzt werden. Eine alternative Lösung bietet das kurz-

zeitige Auskoppeln der geführten Mode in eine Freistrahlmode. Hierbei können größere Volumina abgefragt werden, ohne dabei auf die Vorteile von integrierten optischen Bauelementen zu verzichten.

Dieses Themengebiet bietet noch eine Vielzahl von interessanten und aufschlussreichen Experimenten, die möglicherweise in der nahen Zukunft zu praktischen Anwendungen führen. Der Grundstein ist hiermit gelegt. Nun liegt es daran, darauf aufzubauen um diesen vielversprechenden Ansatz weiter voranzutreiben.

Introduction

Glass cells filled with a gas at room temperature have been a reliable workhorse for researchers in atomic physics since the inception of this field and still are in today's modern experiments. Our knowledge about the electronic structure of atoms and how they interact with light results to a large extent from the investigation of absorption and emission spectra, often obtained from atomic vapor cells. While experiments with ultracold atoms are preferable for very precise and well controlled measurements, typically complex setups occupying an entire optical bench (or more) are required to operate them. In contrast, vapor cells are straightforward to manufacture, small, inexpensive, low power, and simple to use. This makes them particularly interesting for a variety of practical applications. A major advantage of atoms compared to solid state physical systems is that they provide well defined and narrow transition frequencies, which enables repeatable and accurate measurements. Especially alkali metal vapors, such as rubidium (Rb), are favored candidates in this regard due to their simple electronic structure involving a single valence electron, convenient optical transitions, long-lived hyperfine ground states and large vapor pressure at moderate temperatures.

Indeed, we indirectly take advantage of alkali vapor cell based technology in our everyday life: Rb atomic clocks are used on board the GPS [1] and the European Galileo navigation satellites [2] owing to their small size and low power requirements, as frequency and timing reference for audio and television broadcasting and for synchronization tasks in mobile phone base stations [3]. Here, timekeeping is achieved by probing atomic transition frequencies, which can be done with high accuracy. For this reason, and because even tiny external perturbations influence the atomic energy structure, vapor cells can be used as very precise senors, e.g., for DC electric fields [4], microwave fields [5, 6] with spatial resolution [7, 8] and magnetic fields [9, 10] with medical applications in both magnetocardiography [11–13] and magnetoencephalography [14–17]. Besides the measurement of electromagnetic fields, their sensing capabilities might also be utilized as gas detectors [18] and as gyroscopes [19, 20]. In the context of quantum information processing, vapor cells are envisaged to serve as building blocks in a scalable quantum network [21]. For this purpose, a single photon source based on thermal atoms has been proposed [22] and successfully demonstrated in our lab just now. A compatible and highly efficient quantum memory can be realized with vapor cells as well [23–25]. The wide range of applications further includes optical devices such as an optical isolator [26] and narrow band pass filters [27–29] which are inherently matched to the atomic transition frequency.

In recent years, considerable effort has been put into the miniaturization of vapor cells in terms of confinement [33–35] as well as overall size [30–32]. Especially microfabricated cells offer low power dissipation, small size (thereby increasing the spatial resolution of sensors) and wafer-level integration with the potential for mass production and hence cost reduction. This procedure has enabled the fabrication of extremely compact chip-scale atomic clocks [30, 36] and magnetometers [37–39] and might potentially lead to SI-traceable references for multiple base units within a single chip [40].

An even higher level of miniaturization and integration can be achieved through the marriage of atomic vapor cells and photonic integrated circuits (PICs). This is the subject that we are addressing in the present work. A PIC contains multiple photonic devices on a small chip, similar to an electronic integrated circuit (IC) with the difference that the signal is carried by light instead of an electrical current and circuit components are interconnected via optical waveguides rather than conductive traces. The evanescent field arising from total internal reflection inside these waveguides can be used to interface the guided mode with atomic vapor surrounding the waveguide within a distance on the order of $\lambda/2\pi$, where λ is the wavelength of the guided light. Besides the investigations presented in this thesis, the same approach is followed by the group of Prof. Uriel Levy in Jerusalem who has demonstrated the first proof of principle [41] and performed follow-up studies [42–44]. The implementation of such a hybrid system offers a huge potential for both practical applications as well as fundamental studies of light-matter interactions. Some of the benefits will be discussed in the following.

Imagine a conventional spectroscopy setup with laser beams which are manipulated with mirrors, lenses, electro- or acousto-optical modulators and finally captured by some sort of detector. All these components are typically mounted on a vibration isolated optical bench and are taking up quite some space. The same components can also be realized in a PIC [45], including light sources in form of, e.g., distributed feedback lasers [46, 47] or flip-chip bonded vertical-cavity surface-emitting lasers [48, 49], detectors [50, 51] or even heaters to control the vapor pressure [30, 52], however on a much smaller scale, with immunity to vibration and inherently perfect optical alignment due to waveguide interconnections. The rapidly growing field of micro- and nanophotonics and well-established fabrication processes in the semiconductor industry allow a dense integration of multiple devices on a single chip in batch production. Optical chips are readily compatible with the fiber-based telecommunication network infrastructure, where the inclusion of atomic vapors might be utilized as an integrated frequency reference to avoid mixing of independent optical carriers in dense wavelength division multiplexing [53]. Some of the earlier mentioned vapor cell based applications can also be implemented using this hybrid approach allowing for ultra-compact designs with even further improved portability and power consumption. This is in particular interesting for sensing and referencing tasks which could be integrated into handheld

devices. As the atoms surrounding a waveguide are probed on a sub-micron scale, it might be possible to increase the spatial resolution of these sensors. For example, in the realm of magnetometry, investigations were made in this direction with the evanescent field arising from total internal reflection at a prism surface [54]. It is important to note that the atomic motion in a thermal vapor involves Doppler- and transit time broadening and the atom's energy structure is affected by atom-surface interactions at close proximity to the waveguide. These effects have to be taken into account as they will limit the precision of potential sensing or clock devices. However, the achievable precision might certainly be "good enough" for many applications where the benefits of this approach predominate.

Using micro- or nanophotonic structures it is also possible to modify and tailor the light field which couples to the atoms. The small mode area of the evanescent field enables efficient atom-light interaction which can be boosted even more by trapping the light field in resonant cavity structures. In this case, the atom can interact with the circulating photon multiple times. This concept has established the field of cavity quantum electrodynamics (QED) [55–57]. The interaction strength further depends on the cavity mode volume: the smaller the mode volume, the larger the energy concentration of a photon in the mode, thus the larger the interaction strength. Nanophotonic resonators provide extremely small mode volumes and, in addition, the possibility for scalable fabrication which makes them promising candidates for the realization of large-scale quantum networks [58–60]. Consequently, quite a number of experiments has been performed with atoms and microresonators. While coupling thermal atoms to a fused silica microsphere was demonstrated early-on [61], the so-called strong coupling regime could only be explored with ultracold atoms in combination with nanophotonic resonators [62, 63] or photonic crystal waveguides [64]. The above mentioned atomic motion has prevented strong coupling of thermal atoms so far, as an extremely large coupling strength would be required to overcome the motional dephasing. However, as we will assess in this work, it might be possible to fulfill this criterion with certain resonator designs. If so, this would be a major breakthrough towards a scalable quantum network, since miniaturization of a cold atom experiment to the same extent is certainly not a less challenging task. Irrespective of whether strong coupling can be accomplished or not, any enhancement in the coupling strength would increase the efficiency and therefore the performance of potential devices.

In a different context, the ability to confine light in a small volume with optical waveguides might be exploited for fundamental investigations of dipole-dipole interactions between thermal atoms. This topic has recently gained renewed interest [35, 65, 66] and appears to be not yet fully understood [67, 68]. Further insight into the underlying physics could be obtained by reducing the dimensionality and hence the complexity of the problem. First steps in this direction have already been undertaken by confining atomic vapor within nano-cells [35, 68] which constitutes a quasi two-dimensional system. The next stage could be achieved utilizing the sub-wavelength confinement of a

waveguide mode which restricts the atom-light interaction in the transversal direction but remains invariant along the waveguide, which represents a one-dimensional system. A particularly suitable waveguide design for this purpose would be slot waveguides [69], where the mode is squeezed into a narrow gap in between two solid core waveguides. Moreover, in thermal vapor cells a very large range of atomic densities can be covered by simply changing the cell temperature.

This thesis

The integration of thermal atoms with photonic waveguide structures was an entirely new topic within our institute at the start of this dissertation. A close collaboration with Prof. Wolfram Pernice at the KIT[1], who contributed his expertise in the fabrication of the photonic devices and provided the optical chips made this project possible. In our first approach, the optical chips were mounted into a CF flange and connected to a small vacuum chamber which was filled with cesium vapor first and with Rb later on. As it turned out, this solution was far from being ideal. Temperature control of the steel chamber and the chip itself was not sufficient, with the consequence that quite a few chips quit working after a short time, probably due to Rb deposit on the structures. Furthermore, investigating devices located at different positions on the chip required realignment of the entire optical setup, as the chamber itself was fixed.

Things got much better when we were able to anodically bond the chips to vapor cells. Now, temperature could be well controlled with a small oven and different devices could be addressed by simply moving the cell with a translation stage. This setup enabled the investigation of a variety of photonic devices coupled to thermal Rb vapor including single waveguide transmission lines, Mach–Zehnder interferometers, slot waveguides, devices for two-photon spectroscopy, and with the addition of a protection layer also ring resonators.

In this thesis, we will separately discuss the characteristics and results for the individual devices and also cover the common properties and peculiarities which arise when interfacing thermal atoms with photonic waveguides. These include enhanced Doppler broadening and transit time broadening, Casimir–Polder interactions and modification of the atomic decay rate at these short distances as well as alkali metal induced transmission losses. An effective susceptibility model is presented, which allows to predict the interaction of atoms with the guided modes of relatively simple structures. For more complex devices, another model has been developed in this work which is based on Monte Carlo simulations of atomic trajectories. The experimental advances and theoretical considerations resulting from this thesis might provide a framework for continuing work in this field, which perhaps one day leads to real world applications.

[1] At that time, now at the University of Münster.

Outline

This thesis begins with a theoretical part, which covers in chapter 1 the derivation of the optical Bloch equations for a two-level atom and the motional effects arising with thermal atoms. The photonic devices utilized in this work are introduced in chapter 2 to obtain a basic understanding of their operation. An overview of the experiment including the cell- and chip-design is presented in chapter 3. Chapter 4 covers the topics which are specific to waveguide spectroscopy of alkali metal vapor. This includes the two theoretical models, atom-surface interactions, losses due to alkali exposure and measurement results of a ridge waveguide. Subsequently the investigated photonic devices are treated in detail in chapters 5 to 8. Finally, a brief summary and an outlook on future prospects is given at the end of this work.

1 Atom-light interactions

This chapter is intended to introduce the fundamental theory required to describe the interaction between light and atoms. It is the essential basis of the experiments in this work and the derived concepts will be used to develop models to assist with the interpretation of our results and make predictions for potential upcoming experiments.

We first derive the optical Bloch equations for a two-level atom interacting with a classical light field. Even though the investigated alkali atoms exhibit a multi-level electronic structure, a two-level description is sufficient in our case, as we probe the transitions with a single near-resonant laser field. Furthermore, optical pumping plays a negligible role as the interaction time of the atoms with the evanescent field is short compared to the excited state lifetime and because of the low Rabi frequencies involved for the most part. The full spectrum can be obtained by summation of individual two-level transitions taking into account the appropriate transition strengths and energy separations. Afterwards we deal with the consequences of atomic motion, which play a significant role in our experiments.

1.1 The two-level atom

We consider a two-level atom which has a ground state $|1\rangle$ and an excited state $|2\rangle$. The two states are separated by an energy $\hbar\omega_0$ and the atomic Hamiltonian is therefore given by

$$H_{\mathrm{A}} = \hbar\omega_0 \left|2\right\rangle \left\langle 2\right| . \tag{1.1}$$

The atom is assumed to interact with a classical monochromatic light field with angular frequency ω, which is valid if a large number of photons is involved:

$$\boldsymbol{E}(\boldsymbol{r},t) = \frac{1}{2}\left[\boldsymbol{\mathcal{E}}_0 e^{\mathrm{i}(\boldsymbol{k}\cdot\boldsymbol{r}-\omega t)} + \boldsymbol{\mathcal{E}}_0^* e^{-\mathrm{i}(\boldsymbol{k}\cdot\boldsymbol{r}-\omega t)}\right] , \tag{1.2}$$

where $\boldsymbol{k}$ is the wave vector. Since for an optical transition the wavelength of the field is much larger than the extent of the atom, we omit the spatial dependence of the electric field and only consider the field at the position of the atom ($\boldsymbol{r} = 0$). This assumption is known as the dipole approximation which also allows us to write the atom-light interaction Hamiltonian in the lowest order of the multipole expansion:

$$H_{\mathrm{AL}} = -\boldsymbol{d}\cdot\boldsymbol{E} , \tag{1.3}$$

with $\boldsymbol{d}$ being the atomic dipole operator. The total Hamiltonian of the system can then be written as

$$H = H_{\mathrm{A}} + H_{\mathrm{AL}} \,. \tag{1.4}$$

In our experiments we usually deal with a large number of atoms taking part in the measurement process. The prevailing treatment for such an ensemble of atoms interacting with a classical light field is the density matrix method [70]. If p_n is the (classical) probability of the ensemble being in the state $|\psi_n\rangle = \sum_i a_i |i\rangle$, with complex coefficients a_i in the orthonormal basis states $|i\rangle$, its density matrix is given by

$$\rho = \sum_n p_n |\psi_n\rangle \langle\psi_n| = \sum_{nij} p_n a_i^{(n)} a_j^{(n)*} |i\rangle \langle j| \,, \tag{1.5}$$

with the matrix elements

$$\rho_{ij} = \sum_n p_n a_i^{(n)} a_j^{(n)*} \,. \tag{1.6}$$

Since the diagonal elements $\rho_{ii} = |a_i|^2$ are the probabilities of finding the atom in state $|i\rangle$, they are called populations, whereas the off-diagonal elements ρ_{ij} are called coherences due to their appearance in interference terms. The expectation value of any operator A can be calculated by $\langle A\rangle = \mathrm{tr}(\rho A)$.

The Hamiltonian $H(t)$ determines time evolution of the density matrix, which is described by the von Neumann equation:

$$\frac{\partial\rho(t)}{\partial t} = -\frac{\mathrm{i}}{\hbar}\left[H(t), \rho(t)\right] \,. \tag{1.7}$$

So far, only energy transfer between the atom and the driving field E has been considered, which is sufficient to describe absorption and stimulated emission. However, in a real atom also dissipative processes due to its interaction with the environment are present, for example, spontaneous emission or collisions. If a certain dissipative process affects all atoms of an ensemble equally, it is called a homogeneous process. Within the density matrix formalism, these processes can be conveniently included in terms of the Lindblad operator $L_{\mathrm{D}}(\rho)$ which is added to eq. (1.7). The resulting equation is known as the Lindblad master equation and is given by

$$\frac{\partial\rho(t)}{\partial t} = -\frac{\mathrm{i}}{\hbar}\left[H(t), \rho(t)\right] + L_{\mathrm{D}}(\rho(t)) \,. \tag{1.8}$$

The general form of the Lindblad operator is given by [71]

$$L_{\mathrm{D}}(\rho) = -\frac{1}{2}\sum_m (C_m^\dagger C_m \rho + \rho C_m^\dagger C_m) + \sum_m C_m \rho C_m^\dagger \,, \tag{1.9}$$

where the sum runs over all possible decay channels m. For the two-level atom, the excited state decays at rate Γ_0, thus we only have a single operator $C_1 = \sqrt{\Gamma_0}\,|1\rangle\langle 2|$ and we obtain

$$L_{\mathrm{D}}(\rho) = \Gamma_0 \begin{pmatrix} \rho_{22} & -\rho_{12}/2 \\ -\rho_{21}/2 & -\rho_{22} \end{pmatrix} . \tag{1.10}$$

Rotating frame transformation

The electric field which enters the interaction Hamiltonian eq. (1.3) contains terms oscillating at optical frequencies. These oscillations are much faster than the evolution timescales of the atomic system. In order to get rid of the fast oscillating terms one can make a transformation into a frame rotating at the frequency ω of the light field. This step is performed via a unitary transformation matrix

$$U = \begin{pmatrix} 1 & 0 \\ 0 & e^{\mathrm{i}\omega t} \end{pmatrix}. \tag{1.11}$$

The transformed density matrix is then given by

$$\tilde{\rho} = U^\dagger \rho U = \begin{pmatrix} \rho_{11} & \rho_{12} e^{\mathrm{i}\omega t} \\ \rho_{21} e^{-\mathrm{i}\omega t} & \rho_{22} \end{pmatrix}, \tag{1.12}$$

and by inserting eq. (1.12) into eq. (1.7), we receive for the transformation of the Hamiltonian

$$\tilde{H} = U^\dagger H U - \mathrm{i}\hbar U^\dagger \frac{\partial U}{\partial t}. \tag{1.13}$$

Inserting eq. (1.4) into eq. (1.13) and using the matrix elements of the dipole operator $\boldsymbol{d}_{ij} = \langle i | \, \boldsymbol{d} \, | j \rangle$ we obtain[1]

$$\tilde{H} = \begin{pmatrix} 0 & -\frac{\boldsymbol{d}_{12}}{2} \left(\boldsymbol{\mathcal{E}}_0 + \boldsymbol{\mathcal{E}}_0^* e^{\mathrm{i}2\omega t} \right) \\ -\frac{\boldsymbol{d}_{21}}{2} \left(\boldsymbol{\mathcal{E}}_0 e^{-\mathrm{i}2\omega t} + \boldsymbol{\mathcal{E}}_0^* \right) & \hbar(\omega_0 - \omega) \end{pmatrix}, \tag{1.14}$$

where the origin of the energy was chosen to be in the atomic ground state.

The off-diagonal terms in eq. (1.14) contain terms that oscillate at twice the driving frequency and can be neglected, if the light frequency is close to resonance and the atom-light coupling is weak, as they average out quickly compared to atomic timescales. This common step is known as the rotating wave approximation [72]. Applying this approximation yields

$$\tilde{H} = \hbar \begin{pmatrix} 0 & \Omega_0/2 \\ \Omega_0^*/2 & -\Delta \end{pmatrix}, \tag{1.15}$$

where we have introduced the detuning $\Delta = \omega - \omega_0$ and the Rabi frequency $\Omega_0 = -\frac{\boldsymbol{d}_{12} \boldsymbol{\mathcal{E}}_0}{\hbar}$ which is a measure for the strength of the atom-light coupling. The transformation of the Lindblad operator into the rotating frame is simply given by $\tilde{L}_\mathrm{D}(\tilde{\rho}) = L_\mathrm{D}(\rho)$.

Now we can write down the time evolution of the density matrix elements for the two-level atom in the rotating wave approximation by inserting equations (1.12), (1.15) and

[1] Since $\boldsymbol{d}$ has odd parity, only its off-diagonal matrix elements are non-vanishing.

(1.10) into the master equation (1.8):

$$\frac{\partial}{\partial t}\tilde{\rho}_{11} = \Gamma_0\tilde{\rho}_{22} - \mathrm{Im}\left(\Omega_0^*\tilde{\rho}_{12}\right) , \tag{1.16a}$$

$$\frac{\partial}{\partial t}\tilde{\rho}_{12} = -\left(\frac{\Gamma_0}{2} + \mathrm{i}\Delta\right)\tilde{\rho}_{12} - \mathrm{i}\frac{\Omega_0}{2}(\tilde{\rho}_{22} - \tilde{\rho}_{11}) , \tag{1.16b}$$

$$\frac{\partial}{\partial t}\tilde{\rho}_{21} = \left(\mathrm{i}\Delta - \frac{\Gamma_0}{2}\right)\tilde{\rho}_{21} + \mathrm{i}\frac{\Omega_0}{2}(\tilde{\rho}_{22} - \tilde{\rho}_{11}) = \frac{\partial}{\partial t}\tilde{\rho}_{12}^* , \tag{1.16c}$$

$$\frac{\partial}{\partial t}\tilde{\rho}_{22} = -\Gamma_0\tilde{\rho}_{22} + \mathrm{Im}\left(\Omega_0^*\tilde{\rho}_{12}\right) = -\frac{\partial}{\partial t}\tilde{\rho}_{11} . \tag{1.16d}$$

Additionally, we have the constraint $\tilde{\rho}_{11} + \tilde{\rho}_{22} = 1$, since the total population is conserved. The above equations (1.16) are the optical Bloch equations of a two-level atom.

1.2 Motional effects

So far we only considered atoms at rest. In a thermal vapor, the atoms have a mean velocity which is on the order of $300\,\mathrm{m\,s^{-1}}$ at room temperature. This motion causes several observable effects on the spectroscopic features, two of which will be discussed in the following. In an ordinary vapor cell experiment the line width is dominated by the Doppler broadening, which will be introduced first. However, when spectroscopy is performed with nanophotonic structures, transit time effects make a significant contribution and will be treated in the second part. Both processes lead to an inhomogeneous line broadening as the velocity and transit path are different for each individual atom.

1.2.1 Doppler broadening

The absorption frequency of an atom moving at velocity $\boldsymbol{v}$ in a light field with frequency ω and phase velocity c is shifted as a consequence of the Doppler effect. For $|\boldsymbol{v}| \ll c$ the frequency which is perceived by the atom is given by

$$\omega' = \omega - \boldsymbol{k}\cdot\boldsymbol{v} , \tag{1.17}$$

where $\boldsymbol{k}$ is the wave vector of the light field with $|\boldsymbol{k}| = \omega/c$. This leads to a modified detuning in the optical Bloch equations (1.16):

$$\Delta_\mathrm{D} = \Delta - \boldsymbol{k}\cdot\boldsymbol{v} . \tag{1.18}$$

To obtain the average response of an ensemble of atoms to a light field one has to sum over the contributions from all atomic velocities

$$\tilde{\rho}_\mathrm{D}(\Delta) = \mathcal{N}\int F(\boldsymbol{v})\tilde{\rho}(\delta,\boldsymbol{v})\,\mathrm{d}\boldsymbol{v} , \tag{1.19}$$

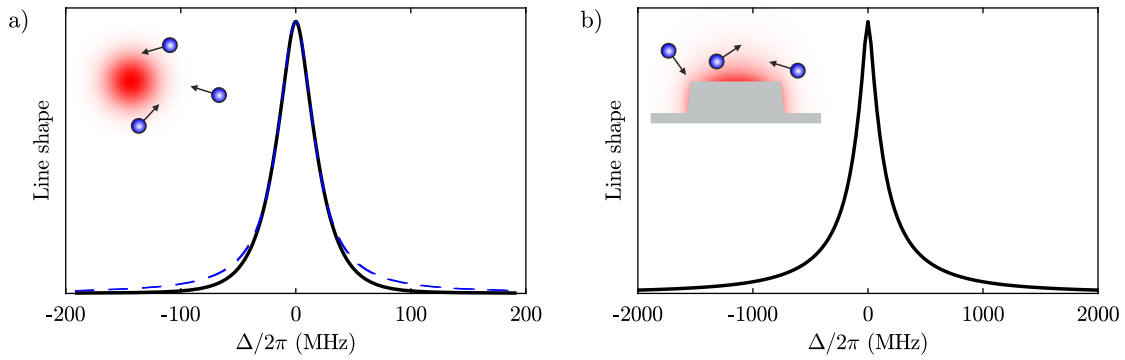

Figure 1.1: Transit time broadened line shape. a) Result for a Gaussian beam with a waist of $w_0 = 2\,\mu\text{m}$. The blue dashed line is a Lorentzian profile with the same FWHM. b) Result for a ridge waveguide. The insets illustrate the atom transits through the electric field for each case.

where $\mathcal{N}$ is the atomic number density and $F(\boldsymbol{v})$ is the probability distribution of atomic velocities which is Maxwellian for a gas in thermodynamic equilibrium (see section 4.3.2 for details). The distribution of atomic velocities translates to a distribution of transition frequencies, which results in a Doppler broadened spectrum of the ensemble.

1.2.2 Transit time broadening

In an atomic vapor experiment, the interaction time of a moving atom with a light field is in general finite. If the light field is a tightly focused laser beam or an evanescent wave, the interaction time can become shorter than the lifetime of the excited state. In this case, the line width is dominated by the transit time rather than the spontaneous decay rate.

The line width of a transit time broadened spectrum can be approximately calculated for a Gaussian beam, see e.g. reference [73]. However, for a more complex geometry of the volume in which the atom-light interaction takes place, the prediction of the line shape is less trivial. Since the Monte Carlo method which will be introduced later on in section 4.3 inherently accounts for transit time effects, we can simulate the influence of the finite interaction time for the cases of a Gaussian beam with a waist of $w_0 = 2\,\mu\text{m}$ and the evanescent field of a ridge waveguide (width $w = 900\,\text{nm}$ and height $h = 180\,\text{nm}$), which is shown in Figure 1.1 a) and b), respectively.

For these simulations the Doppler effect has been ignored to highlight the consequences of a finite transit time. In case of the Gaussian beam this results in a line shape with a full width at half maximum (FWHM) of $\delta\omega/2\pi \approx 38\,\text{MHz}$. Also plotted in Figure 1.1

a) is a Lorentzian with the same FWHM, showing that the transit time broadened line shape is not exactly Lorentzian as each transversal velocity class contributes with a different width to the total signal, which is therefore inhomogeneously broadened. In the waveguide situation transit time effects are even more significant since the evanescent field decay length is on the order of $\sim 100\,\mathrm{nm}$ which leads to a line width of $\delta\omega/2\pi \approx 260\,\mathrm{MHz}$ for the above example. The non-Lorentzian line shape is obvious in this case and will be discussed in more detail in section 4.3. Very similar line shapes have been observed in ultrahigh-resolution molecular spectroscopy in a transit time limited regime [74].

2 Fundamentals of integrated optics

The interfacing of atoms with light via photonic integrated circuits is the basis of all experiments within this thesis. This chapter is therefore intended to introduce the fundamental properties of all components of the integrated circuits and devices used in the course of this work. The working principle and characteristics of specific devices, such as ring resonators, will be explained in the corresponding chapters later on.

The subsequent sections are meant to introduce the basic concepts of integrated optics in order to obtain the required knowledge for the experiments and simulations presented in this work. A more thorough treatment of the subject can be found for example in [75].

2.1 Waveguides

Dielectric waveguides are the essential component of an integrated optical circuit. They are used to interconnect photonic devices on a chip, similar to the optical fibers employed for signal transmission over long distances. Moreover, they already form devices by themselves, such as directional couplers or, in our case, serve as an interface between confined light and atoms.

The most common waveguide geometry in an integrated circuit is the rectangular ridge waveguide shown in Figure 2.1. It consists of a high index dielectric material, the core, which is truncated in the transverse directions and surrounded by lower index material, the cladding. For all experiments in this work, the core material is silicon nitride (Si_3N_4) with $n_2 = 2$ [76], and the substrate material is silicon dioxide (SiO_2) with $n_3 = 1.45$ at $\lambda = 780\,\mathrm{nm}$ [77]. The refractive index contrast allows for light propagation along the longitudinal direction, while propagation is prohibited in the transversal directions. This guiding mechanism can be understood by considering the path of a plane wave (or an optical ray) inside the core: since the refractive index of the core material is larger than the index of the surrounding, total internal reflection can occur at the core-cladding interfaces. As the wave repeatedly bounces back and forth between the core boundaries it has to interfere constructively with itself in order to propagate along the waveguide. This resonance condition leads to a discrete set of guided modes which are characteristic of a specific waveguide structure. A mode is a spacial field distribution in the transverse plane of a waveguide which remains constant

along the propagation direction if the structure is translation-invariant. The electric and magnetic fields of a mode can therefore be written as

$$\boldsymbol{E}_m(\boldsymbol{r},t) = \boldsymbol{\mathcal{E}}_m(x,y)\exp\left[\mathrm{i}(\beta_m z - \omega t)\right] , \tag{2.1a}$$
$$\boldsymbol{H}_m(\boldsymbol{r},t) = \boldsymbol{\mathcal{H}}_m(x,y)\exp\left[\mathrm{i}(\beta_m z - \omega t)\right] , \tag{2.1b}$$

where m is an integer mode index, $\boldsymbol{\mathcal{E}}_m$ and $\boldsymbol{\mathcal{H}}_m$ are the mode profiles and β_m is the complex propagation constant, corresponding to the eigenvalue of the m-th mode. The real part of β_m determines the phase variation along z, whereas its imaginary part accounts for any attenuation along the propagation direction due to absorption, scattering or radiation losses. Linked to the propagation constant is the effective index n_{eff}, which is analogous to the refractive index in homogeneous media and determines the phase velocity of light in the waveguide. It is defined as

$$n_{\mathrm{eff},m} = \beta_m/k = c/v\,, \tag{2.2}$$

where $k = 2\pi/\lambda$ is the wavenumber in vacuum and v is the phase velocity in the waveguide. Related to the effective index is the group refractive index defined as $n_{\mathrm{g}} = c/v_{\mathrm{g}}$, where v_{g} is the group velocity. In case of small dispersion the group refractive index can be approximated as

$$n_{\mathrm{g}} = n_{\mathrm{eff}} - \lambda\frac{\partial n_{\mathrm{eff}}}{\partial\lambda}\,. \tag{2.3}$$

The ray optics approach used above for describing the guiding mechanism has many limitations, especially when considering dimensions on a sub-wavelength scale. Therefore, a rigorous analysis of the fields requires the solution of Maxwell's wave equations. Solving these equations analytically is (except for a few cases) either very difficult or impossible and usually numerical methods are employed for this problem. We use the Wave Optics Module within COMSOL Multiphysics for this task which is based on a finite element analysis.

The electric field distribution of the fundamental mode of a rectangular waveguide ($h = 180\,\mathrm{nm}$, $w = 1100\,\mathrm{nm}$) is shown in Figure 2.1 b). A fraction of the mode reaches into the cladding region in terms of an evanescent field. It decays exponentially with distance to the core. The top and side panels of Figure 2.1 b) show horizontal and vertical cuts of the electric field through the core center. Fitting an exponential function to the evanescent tails (red sections) yields a $1/e$-decay length of $\gamma_x = 81\,\mathrm{nm}$ for the side wall field and $\gamma_y = 92\,\mathrm{nm}$ for the top field. It is this part of the mode which interacts with the atomic vapor in our experiments. Only the fraction of optical power in the cladding region contributes to the atom-light interaction which is obtained by integrating the intensity of the mode over the cladding region, denoted by C, and the

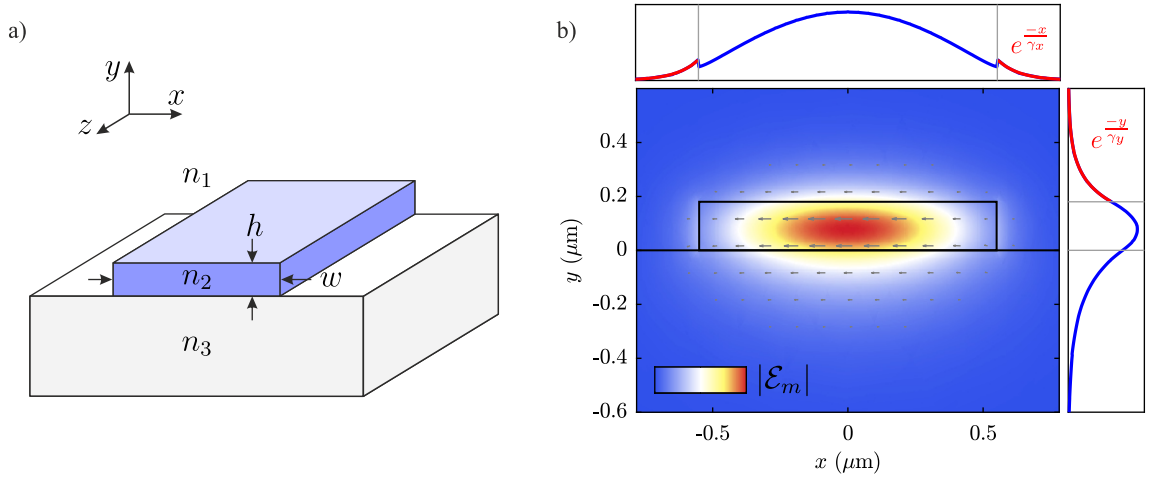

Figure 2.1: Waveguide structure and mode profile. a) Geometry of a ridge waveguide as used in this work. The waveguide core of refractive index n_2 is placed on a substrate of index n_3 and surrounded by a cladding of index n_1. b) Simulated electric field profile $|\boldsymbol{\mathcal{E}}_m(x,y)|$ of the fundamental TE_0 mode for a Si_3N_4 waveguide ($h = 180\,\text{nm}$, $w = 1100\,\text{nm}$) on an SiO_2 substrate. The gray arrows indicate the direction and strength of the electric field, representing the polarization direction. The top and side panels show horizontal and vertical cuts of the electric field through the center of the core (blue lines). Red lines are exponential fits to the evanescent tails.

total cross section, respectively:

$$\eta = \frac{P_C}{P_m} = \frac{\iint\limits_{C} I_m(x,y)\mathrm{d}x\mathrm{d}y}{\iint\limits_{-\infty}^{+\infty} I_m(x,y)\mathrm{d}x\mathrm{d}y}\,, \tag{2.4}$$

where the intensity of the mode is given by

$$I_m = (\boldsymbol{\mathcal{E}}_m \times \boldsymbol{\mathcal{H}}_m^* + \boldsymbol{\mathcal{E}}_m^* \times \boldsymbol{\mathcal{H}}_m) \cdot \hat{\boldsymbol{z}}\,, \tag{2.5}$$

with $\hat{\boldsymbol{z}}$ being the unit vector along the waveguide axis. The cladding power fraction for the waveguide shown in Figure 2.1 equals to $\eta \approx 8.6 \times 10^{-2}$. This value can be increased for example by shrinking the core size or using special geometry designs like slot waveguides (see chapter 7).

Depending on the structure of the waveguide it can support multiple modes. Figure 2.2 a) shows the effective indices of existing modes in a waveguide of height $h = 180\,\text{nm}$[1] as a function of core width. For a mode to be guided in the core, its

[1]This is the default core height of the devices used in this work.

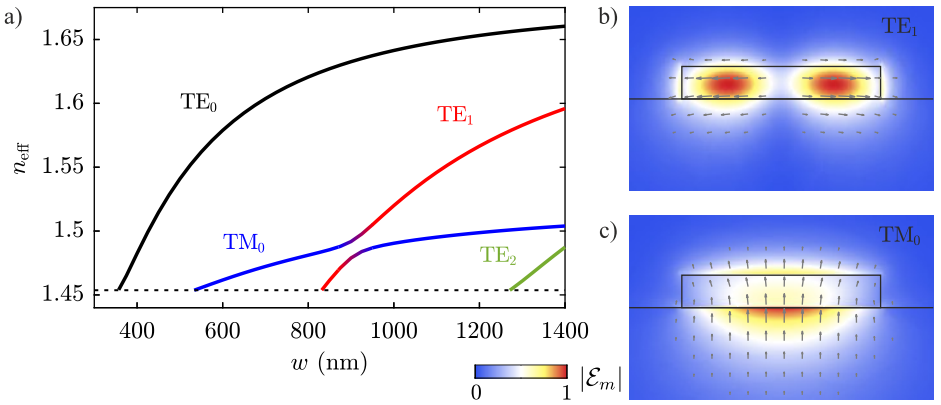

Figure 2.2: Different modes of a Si_3N_4waveguide ($h = 180\,\text{nm}$) on SiO_2 substrate at $\lambda = 780\,\text{nm}$. a) Effective mode indices of the guided modes as a function of core width w. The black dashed line indicates the refractive index of SiO_2 at $\lambda = 780\,\text{nm}$ and therefore the cutoff condition. The waveguide is single mode up to $w = 533\,\text{nm}$. b) and c) show the electric field profiles of a $w = 1100\,\text{nm}$ waveguide for the TE_1 and TM_0 modes, respectively. Gray arrows show the polarization direction of the electric field.

effective index has to be larger than the index of the surrounding media. In our case the refractive index of the substrate determines this cutoff condition. For core widths $w < 533\,\text{nm}$ only a singe mode exists.

The classification of the modes depends on the polarization direction of the fields: if the electric field mostly points in the x direction, it is named TE-like[2] mode, and analogously TM-like mode for magnetic fields. Additionally, the subscript index indicates the number of nodes in the mode profile. See Figure 2.1 b) and Figure 2.2 b)-c) for the mode profiles and polarizations of the fundamental TE_0, and higher order TE_1 and TM_0 modes, respectively. These higher order modes appear with increasing core size, as shown in Figure 2.2 a). At a width of around 900 nm the polarization character of the mode is heavily mixed between a TM_0 and TE_1 mode, which manifests in an anti-crossing in the effective index.

2.2 Grating couplers

Coupling light into and out of a waveguide can be achieved in different ways. The simplest approach is to directly focus a laser beam from free space onto the end face

[2]Because the modes of a ridge waveguide are confined in two transversal dimensions, the z components of both electric and magnetic fields do not vanish completely. Therefore these modes are no true TE or TM modes but rather hybrid modes. This is indicated by the '-like' suffix, which we omit hereafter for the sake of brevity.

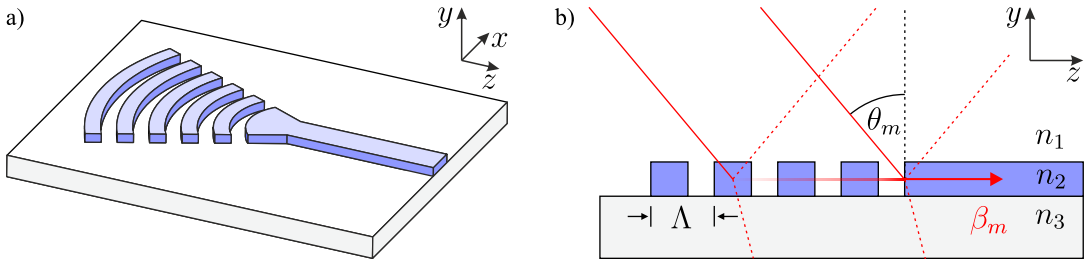

Figure 2.3: Focusing grating coupler. a) Schematic of a focusing grating coupler. The curved grating lines focus the light towards the waveguide with a short taper to convert the size of the laser mode to the size of the waveguide mode. b) Cut through the grating coupler. Light is incident at an angle θ_m with respect to the surface normal and partially diffracted into the waveguide mode β_m. The other part is reflected or transmitted to the substrate.

of a waveguide. However, this method can only be used when the waveguide facet is exposed at the edge of the chip. In order to address devices within the optical chip, an out-of-plane access is required. For this purpose we use grating couplers in our experiments, like the one illustrated in Figure 2.3. The task of the grating is to produce phase matching between a free space laser mode and a certain waveguide mode β_m, which is required for efficient coupling. Without a grating, focusing light from the cladding region with index n_1 onto the waveguide surface at an angle θ_m would lead to the phase matching condition

$$kn_1 \sin\theta_m = \beta_m = kn_{\text{eff}}\,. \tag{2.6}$$

However, for the mode to be guided, $n_{\text{eff}} > n_1$ has to be fulfilled. We now look at the basic principle of a grating coupler to see how it assists to obtain phase matching.

In Figure 2.3 b) the schematic structure of a grating waveguide coupler is shown. The waveguide exhibits a periodic corrugation in propagation direction with a period Λ. This leads to a periodic perturbation of the waveguide modes and introduces spatial harmonics with propagation constants $\beta_q = \beta_0 + q\frac{2\pi}{\Lambda}$ $(q = 0, \pm1, \pm2, ...)$ and the fundamental $\beta_0 \approx \beta_m$ [78]. Hence the phase matching condition for light incident at an angle θ_m is given by

$$kn_1 \sin\theta_m = \beta_m + q\frac{2\pi}{\Lambda}\,, \tag{2.7}$$

which can now be satisfied for negative values of q. It should be noted that in our experiments light is focused through the substrate onto the grating coupler, which is covered with an SiO_2 layer, hence $n_1 \approx n_3$.

Due to optical reciprocity, the grating can also act as an output coupler. Since the amplitude of the guided mode decays exponentially in the coupler region with distance to the waveguide end, the output beam also has an exponentially decaying transverse

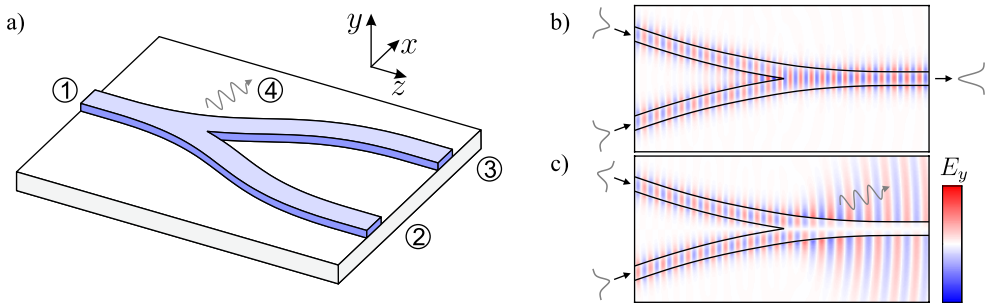

Figure 2.4: Integrated Y junction. a) Schematic of a Y junction composed of a stem waveguide which is connected to port 1 and branching into two waveguides which are connected to ports 2 and 3, respectively. Port 4 represents the radiation mode. b) - c) 2D simulations of the y component of the electric field for a Y junction acting as a combiner. In b) two waves of the same phase are combined to a wave of twice the power at the output. In c) two waves of opposite phase are converted to the radiation mode and no output is obtained.

profile. From this it follows that an input beam should have the same exponential beam profile to obtain maximum coupling efficiency[3]. Also, it is preferable to align the incident beam close to the edge of the grating, as shown in Figure 2.3 b). Although the preceding explanation provides insight into the basic functionality of a grating coupler, coupled wave analysis and Floquet theory are required for a rigorous treatment [75, 78].

To transform the size of a laser beam with a typical waist of 10 µm to the waveguide width of around 1 µm a focusing coupler design is used. This is realized by elliptically curved grating lines (see Figure 2.3 a)) which have a common focal point at the link between grating and waveguide [79]. Additionally, a short taper is used to keep the light confined and guided towards the waveguide [80].

The coupling efficiency for the devices used in this work is usually on the order of a few percent. However, aperiodic grating couplers with efficiencies as high as 87 % have been realized at telecommunication wavelengths by additionally using a backside mirror [81].

2.3 Y junctions

In the design of photonic circuits and their corresponding devices it is often necessary to split optical power into two or more paths, or vice versa. There are several approaches

[3]The maximum overlap that can be achieved between an input beam with Gaussian profile and an exponential beam profile is 80 %.

for this task, e.g., directional couplers [82] or multi-mode interference couplers [83]. Another implementation is the Y junction [84] shown in Figure 2.4 a), which is the type used throughout this work. The operation of a Y junction is usually described in terms of coupled mode analysis. However, we only want to give a simple explanation of its functionality in this section.

The Y junction is composed of a stem waveguide which splits into two arms via circular bends. A tapered section arises during the branching, which allows for a smooth transformation of the modes. If the two arms are identical, the junction behaves like a 50/50 beam splitter as a result of the geometrical symmetry: power inserted at port 1 is equally divided to port 2 and 3.

The other purpose of the Y junction is to combine optical power from two input ports. The operation mechanism for this case is illustrated in Figure 2.4 b) and c) on the basis of electric field simulations. When the two waves incident at port 2 and 3 are in phase, the output power at port 1 is the sum of the powers in both input arms (Figure 2.4 b)). When they are of opposite phase, the first higher order mode at the branching section is excited. If this mode is below the cutoff frequency of the stem waveguide, the power will be converted to the radiation mode and therefore no output power will be obtained at port 1 (Figure 2.4 c)). Assuming the stem and arm waveguides are single mode, the Y junction can therefore be considered as a 4-port device with the radiation mode being connected to port 4. In this case the junction behaves analogous to a conventional beam splitter.

3 Experimental overview

This chapter gives an overview of the main components involved in the presented experiments. First, the general composition of an optical chip is introduced. In our very first experiments involving waveguide structures and thermal atoms the chip was mounted to a vacuum chamber filled with either cesium or rubidium atoms. However, temperature control and alignment of the input and detection optics was rather difficult with this approach. Therefore, subsequent experiments have been performed with the chip integrated into a vapor cell, the construction of which will be described here. In the last section we present the relevant parts of the optical setup and tools that were used to couple light in and out of the photonic structures.

3.1 The waveguide cell

The central part of our experiments is the waveguide cell enabling the marriage of thermal atoms and photonic devices on an optical chip. The cell consists of a main glass body, a reservoir tube and the chip itself which will be described in detail in this section. The whole assembly forms a small sized device which can be conveniently heated and easily positioned in order to select specific devices on the chip as opposed to an earlier version of the experiment, realized with a vacuum chamber.

3.1.1 Chip design and fabrication

The optical chips have been designed and fabricated at the Institute of Nanotechnology at the Karlsruhe Institute of Technology (KIT) by Nico Gruhler in the nanophotonics group of Prof. Wolfram Pernice. One chip usually contains several devices of different functionality and varying design parameters.

The substrate is formed by a 1.1 mm thick $20 \times 20\,\mathrm{mm}^2$ borosilicate plate[1], which is compatible with the anodic bonding process described below. Figure 3.1 a) illustrates the layer composition of a photonic chip. The guiding structures are made of silicon nitride (Si_3N_4) which exhibits a large transmission window between $300\,\mathrm{nm} < \lambda < 6\,\mu\mathrm{m}$

[1] For the Mach–Zehnder interferometer experiments described in chapter 5, a 4 mm thick 1.5 in diameter fused silica vacuum window (Thorlabs VPW42) was used as a substrate.

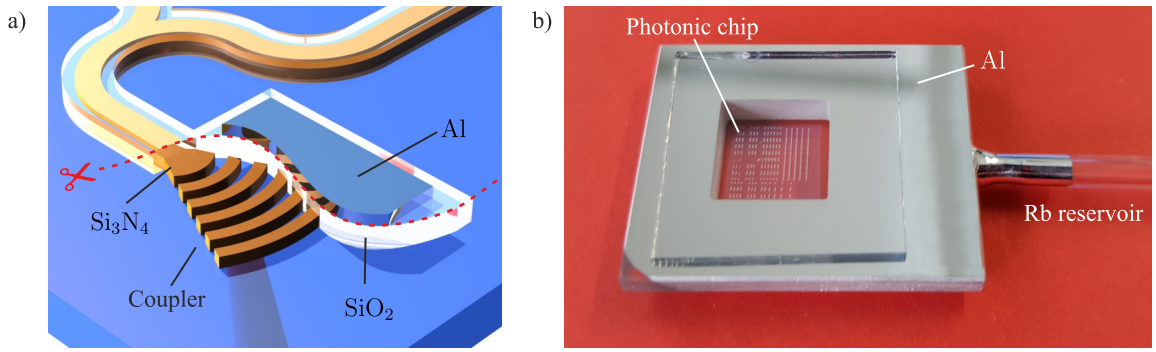

Figure 3.1: Chip design and waveguide cell. a) Layer composition of a photonic chip. The coverage of the grating coupler is depicted sliced to reveal its structure. b) Cell with an anodically bonded photonic chip and attached rubidium reservoir.

[85] and very low material absorption at a wavelength of 780 nm [86]. The devices are patterned within a 180 nm thick Si_3N_4 layer via electron-beam lithography and subsequent CHF_3/O_2-plasma based dry etching, see reference [87] for details. Focusing grating couplers are used for in- and out-coupling of light. All devices are completely covered with a thick (600 nm to 800 nm) silicon dioxide (SiO_2) layer, except for the regions where the atoms are supposed to interact with the light field. This is realized by using hydrogen silesquioxane (HSQ) as a resist in an additional electron-beam lithography step. Furthermore, a 100 nm thick opaque layer of aluminum (Al) is deposited on top of the SiO_2 layer above each grating coupler to avoid leakage of uncoupled light through the coupler and the detection of fluorescence light from atoms inside the cell volume. As described in section 4.5, exposing the structures to rubidium vapor leads to a degradation of the waveguide transmission. Therefore, starting from chip generation NGJ30-II [2], an additional 7 nm to 9 nm thick protection layer consisting of sapphire (Al_2O_3) is deposited on the entire chip, except for a 5 mm wide frame which remains completely uncoated for the anodic bonding. This coating is applied via atomic layer deposition (ALD) providing a closed film which is conformal to the waveguide structures.

An overview of the layer composition of the individual chips used for the measurements presented in this work is given in Appendix D.

3.1.2 Cell construction

The photonic chip is integrated into a rubidium vapor cell as shown in Figure 3.1 b). The main body of the cell consists of a 3.5 mm thick borosilicate glass plate with a $10 \times 10\,\mathrm{mm}^2$ ultrasonically drilled bore forming the inner cell volume. A further bore

[2] See Appendix D.3.

connects the cell volume to a glass tube which is attached laterally via glass blowing and serves as a reservoir for Rb after the filling process. The chip and a similar uncoated borosilicate substrate are connected to the glass frame via triple stack anodic bonding [88] to close the cell volume. After the reservoir tube has been attached, both cell faces were lapped and polished[3] to obtain a surface flatness of $\lambda/4$ which is required for the bonding process to work properly. The polished surfaces are coated with a 100 nm thick aluminum layer acting as an anode material.

For the anodic bonding procedure the Al layer is connected to the positive terminal of a high voltage power supply, whereas the two borosilicate substrates are in contact with plate electrodes (cathode) which are connected to the power supply ground. The whole stack is homogeneously heated to 300 °C. At this temperature the sodium ions contained in the borosilicate become mobile and can diffuse to the cathode when applying a high voltage[4]. The oxygen ions remain in the glass and are bonded to the SiO_2 structure creating a strong electric field between the substrates and the Al layer. This field pulls the substrates into intimate contact to the frame whereupon the Al atoms can diffuse into the substrate and bind to the oxygen ions. The substrates are now joined with the cell body via molecular bonds which leads to a vacuum tight and outgasing free sealing of the cell. After the bonding current has dropped and remains almost constant the cell is cooled down to room temperature.

In order to fill the cell with Rb, its reservoir tube is connected to a glass manifold containing a Rb ampule. The manifold is attached to a vacuum pump and pumped to a pressure of $\sim 1 \times 10^{-7}$ mbar. After pumping for several hours/days, the Rb ampule is broken and a small droplet of Rb is transfered into the reservoir tube. Subsequently, the cell is sealed and separated from the manifold with a gas flame. Details on the fabrication and filling procedure can be found in [90].

3.2 Experimental setup

The relevant parts of the experimental setup are shown in Figure 3.2. The probe light at 780 nm is provided by a Toptica DLX diode laser and is guided to the experiment by an optical fiber. For the two photon measurements, this laser can be locked onto a Doppler-free absorption signal from a Rb vapor cell. The probe beam is first magnified with a telescope to allow for a small beam waist when coupling into the waveguide structures. A beam splitter cube with 90 % reflection is used to send a weak probe beam to the chip, and to direct the light collected from the output grating coupler to the detection setup with small loss. The polarization angle of the probe light is adjusted to the polarization of the desired waveguide mode with a half-wave plate before it is

[3] Lapping and polishing was performed at Photon LaserOptik GmbH [89].
[4] Typically a voltage of 1100 V to 1300 V was used for this type of cell.

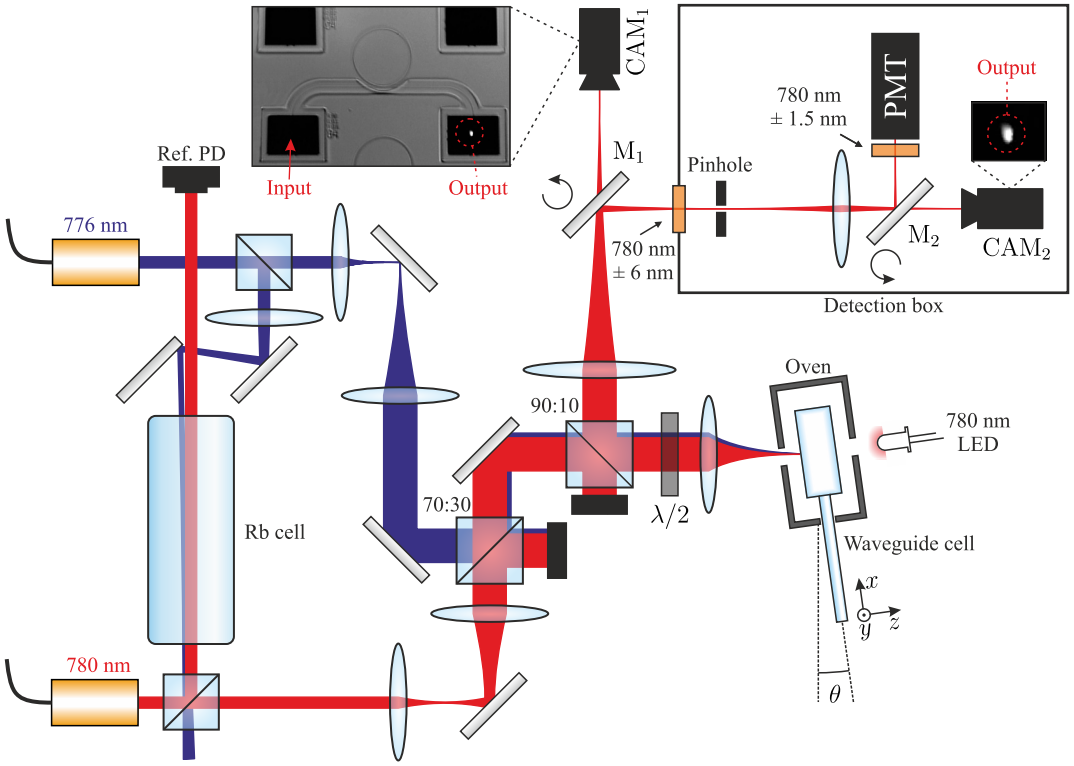

Figure 3.2: Schematic of the experimental setup showing the essential components and beam paths for both one and two photon measurements.

focused with an $f = 50\,\text{mm}$ aspheric lens onto the optical chip. A $1/e^2$ beam waist of $w_0 \approx 6\,\mu\text{m}$ is achieved.

The waveguide cell is housed in an oven with separate temperature control of the reservoir and the chip, where the chip is kept $\sim 30\,^\circ\text{C}$ hotter than the reservoir to minimize Rb condensation on the chip. To fulfill the Bragg condition for the grating coupler, the cell is aligned at an angle $\theta \approx 10^\circ$ with respect to the input beam. The cell is mounted on a three-axis translation stage to enable positioning of the chip with respect to the optical setup. To couple into the photonic structures, the light is focused through the substrate of the chip onto the desired grating coupler. Selection of a specific device and initial coupling into a waveguide structure is monitored using a CMOS camera (CAM_1) when the magnetically mounted mirror M_1 is removed. A 780 nm LED behind the oven illuminates the chip for this purpose. The LED wavelength was chosen to be identical to the probe light to avoid chromatic aberrations during imaging.

The output grating is imaged onto a 100 µm pinhole to isolate the out coupled light from any background light. The alignment of the pinhole is monitored with CAM_2 when mirror M_2 is removed. Due to the strong confinement of the waveguide mode,

high intensities are achieved already at low input powers. Hence, when performing measurements in the weak probe regime a low light level of the out coupled signal has to be detected. For this purpose a photo multiplier tube (PMT) with high sensitivity is used. The entire detection setup is placed inside a lightproof box with only a small opening comprised of a 780 nm bandpass filter to protect the sensitive PMT from any stray light.

For the two photon experiments, the coupling light is provided by a Toptica DL pro diode laser at 776 nm. After expanding the diameter of the coupling beam, it is overlapped with the probe beam using a 70:30 beam splitter and subsequently directed to the optical chip. To suppress detection of the relatively strong coupling light, a narrow band pass filter at 780 nm (Semrock MaxLine LL01-780-12.5) is mounted in front of the PMT. A conventional 10 cm Rb vapor cell is used to obtain reference signals for both one and two photon measurements.

4 Optical waveguide spectroscopy

The spectroscopy of atoms using integrated photonic waveguide structures involves some peculiarities which usually do not need to be considered when performing conventional laser spectroscopy. The strong confinement of the light field does not only provide large coupling strengths but also implicates short interaction times, leading to significant transit time broadening. Furthermore, the atoms are probed close to the waveguide surface within a sub-wavelength range leading to considerable interactions between the atoms and the material environment. These include collisions with the photonic structures causing quenching of the atomic excitation, shift of the energy levels due to Casimir–Polder potentials, as well as a modification of the atomic decay rates.

This chapter comprises the common properties of alkali vapor spectroscopy with integrated photonic structures. First, the effective susceptibility is introduced as a method to calculate the transmission properties of a waveguide surrounded by thermal atoms. Next, atoms-surface interactions are discussed which are also part of the subsequently presented Monte Carlo simulations. This simulation toolbox enables modeling of the complex atom-light interaction for arbitrary waveguide geometries. After these theory sections, spectroscopy measurements with a simple ridge waveguide are presented. Finally, we address the transmission losses of photonic structures immersed in an alkali atmosphere.

4.1 The effective susceptibility

In this section we will introduce the effective susceptibility concept which provides a simple way to model the essential transmission properties of a waveguide surrounded by a gas of thermal atoms. It allows us to treat the atomic vapor around the waveguide as a homogeneous macroscopic medium with a complex refractive index, while taking the non-local and transient response of the atoms in the evanescent field into account. In order to derive a simple expression which can be conveniently plugged into numerical calculations, we will make two approximations: a low vapor density and low probe Rabi frequencies. This method stems from the work on selective reflection spectroscopy and the following approach is mainly based on references [91–93]. The upcoming section

is intended to provide a closed derivation adapted to our system and to clarify the necessary steps sometimes omitted in the mentioned literature.

The underlying idea is to calculate the reflection coefficient of a light field incident under an arbitrary angle on an interface between a dielectric and the atomic medium. To do so, we first derive the electric field radiated by a general dipole polarization above the interface which is caused by the incident light field. In the next step we will consider the specific polarization of a medium comprised of two-level atoms, accounting for their thermal motion. Here we explicitly assume the field to be evanescent on the atomic side of the interface, as it is the case for our waveguide spectroscopy experiments. The resulting reflection coefficient will be related to an effective susceptibility of the atomic medium. The corresponding refractive index is then used to finally calculate the light propagation in a waveguide surrounded by such a medium. This approach has also been successfully applied in a different work on atomic cladding waveguides [41].

4.1.1 Reflection for an arbitrary dipole polarization density

For the derivation of the effective susceptibility we consider the geometry in Figure 4.1 a), which consists of a dielectric with refractive index n in the lower half space $z < 0$ and an atomic vapor in the upper half space $z > 0$. The interface between the two media is taken to be in the xy plane and we choose the polarization direction of the probe field to be normal to the plane of incidence[1]. The probe field is described as a plane wave which is incident at an angle θ_1, given by

$$\boldsymbol{E}_1(\boldsymbol{r}, t) = \hat{\boldsymbol{y}} E_1 \exp\left[\mathrm{i}\left(\boldsymbol{r} \cdot \boldsymbol{k}_1 - \omega t\right)\right] + \text{c.c.}\,, \tag{4.1}$$

with the wave vector $\boldsymbol{k}_1 = nk(a\hat{\boldsymbol{x}} + b\hat{\boldsymbol{z}})$, where $k = \omega/c$, $a = \sin\theta_1$ and $b = \cos\theta_1$. Part of the field is reflected back into the dielectric, whereas the transmitted field creates a dipole polarization in the atomic medium which in turn radiates a field in the direction of the reflected wave an therefore alters the reflection coefficient of the interface. The boundary conditions at the interface demand that the transmitted field and therefore the induced dipole polarization vary in the x direction with $\exp(\mathrm{i}\alpha kx)$, where $\alpha = n\sin\theta_1$. Hence the dipole polarization can be written as

$$\boldsymbol{P}(\boldsymbol{r}, t) = \hat{\boldsymbol{y}} P(z) \exp\left[\mathrm{i}\left(\alpha k x - \omega t\right)\right] + \text{c.c.}\,. \tag{4.2}$$

In the following we omit the complex conjugate (c.c.) for the sake of brevity.

A layer of atomic polarization at a certain position z' emits a plane wave in opposite directions. In absence of the dielectric, the wave vector of this wave in the region $z < 0$ is given by

$$\boldsymbol{k}_2 = k(\alpha\hat{\boldsymbol{x}} - \xi\hat{\boldsymbol{z}})\,, \tag{4.3}$$

[1]This assumption was made for the sake of brevity and does not affect the effective susceptibility. For a polarization in the plane of incidence, the derivation is similar.

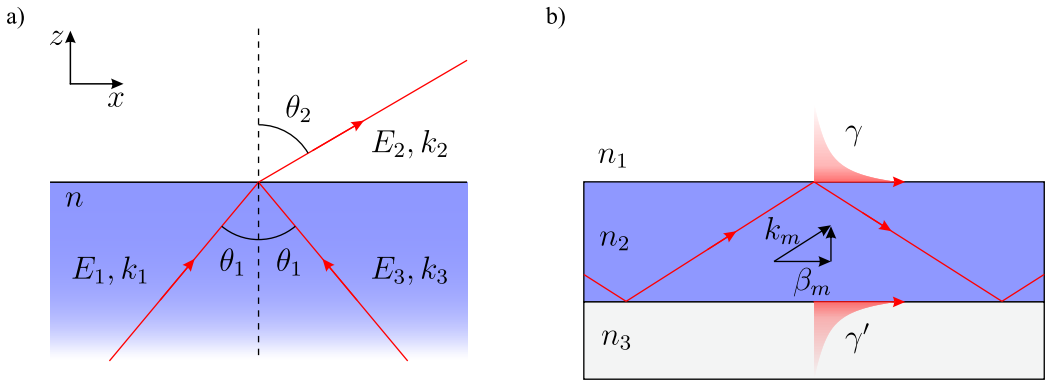

Figure 4.1: Geometry for the derivation of χ_{eff}. a) A plane wave with wave vector in the xz plane is incident on the interface between a dielectric with refractive index n and vacuum, where it is partially reflected and partially refracted. b) Three-layer planar waveguide with $n_2 > n_3 > n_1$. The wave inside the core is totally reflected at both interfaces, resulting in a guided mode with propagation constant β_m, which evanescently decays outside the core in both z directions with penetration depths γ and γ', respectively.

where ξ needs to fulfill the condition $\alpha^2 + \xi^2 = 1$. In the case of total reflection $\alpha > 1$ and we write $\xi = \mathrm{i}\eta$.

In order to find the field due to this dipole polarization we consider the wave equation in the Lorenz gauge condition

$$\left(\nabla^2 + k^2\right) \boldsymbol{A} = \mathrm{i}\omega\mu_0 \boldsymbol{P}\,, \tag{4.4}$$

where $\boldsymbol{A}$ is the vector potential. The derivation of eq. (4.4) and relations between the fields and the electromagnetic potentials can be found in Appendix A.

In order to solve the wave equation (4.4) we need to find a Green's function $G(z, z')$ that solves

$$\left(\nabla^2 + k^2\right) G(z, z') = \delta(z - z') \exp(\mathrm{i}\alpha k x)\,. \tag{4.5}$$

The derivation of the corresponding Green's function can be found in Appendix A.1 and we directly continue with the result:

$$G(z, z') = \frac{1}{2\mathrm{i}\xi k} \exp(\mathrm{i}\xi k|z - z'| + \mathrm{i}\alpha k x)\,. \tag{4.6}$$

The solution of the wave equation is then given by the convolution of $G(z, z')$ with the source term:

$$\boldsymbol{A}(\boldsymbol{r}) = \frac{\omega\mu_0}{2\xi k} \exp(\mathrm{i}\boldsymbol{k}_2 \cdot \boldsymbol{r})\hat{\boldsymbol{y}} \int_0^\infty \mathrm{d}z' P(z') \exp(\mathrm{i}\xi k z')\,. \tag{4.7}$$

To calculate the associated electric field we use eq. (A.9) from the Appendix and get

$$\boldsymbol{E}_{\mathrm{p}}(\boldsymbol{r}) = \frac{\mathrm{i}k}{2\xi\epsilon_0} \exp(\mathrm{i}\boldsymbol{k}_2 \cdot \boldsymbol{r})\hat{\boldsymbol{y}} \int_0^\infty \mathrm{d}z' P(z') \exp(\mathrm{i}\xi k z') \,. \tag{4.8}$$

This field is the radiation of the atomic dipole polarization. At the interface it is partially reflected back into the vapor and a part of it is refracted into the dielectric and thereby effectively alters the reflection coefficient. The total amplitude of the reflected wave E_3 is therefore a combination of the field which would be reflected if the half space $z > 0$ would be vacuum and the dipole radiation which is refracted into the dielectric. Using Fresnel's equations this can be expressed in a reflection coefficient:

$$r_\perp = \frac{E_3}{E_1} = \frac{nb-\xi}{nb+\xi} + \frac{2\xi}{nb+\xi}\frac{E_{\mathrm{p}}}{E_1} = \frac{nb-\xi}{nb+\xi} + \frac{4nb\xi}{(nb+\xi)^2}\frac{E_{\mathrm{p}}}{E_2} \,, \tag{4.9}$$

where the Fresnel equation for the refracted field into the vapor $E_2 = 2nb/(nb+\xi)E_1$ has been used.

We can now introduce the complex effective susceptibility χ_{eff}, which is the susceptibility a medium in the half space $z > 0$ would have in order to reproduce the same reflectivity as in eq. (4.9). In response to an incident probe field, this susceptibility gives rise to a field in the medium with the wave vector $\boldsymbol{k}_{\mathrm{a}} = k(\alpha\hat{\boldsymbol{x}} + \zeta\hat{\boldsymbol{z}})$, since the x component needs to be the same on both sides of the interface. The z component in the medium is therefore determined by

$$k\left(\alpha^2 + \zeta^2\right) = k\left(1 + \chi_{\mathrm{eff}}\right) \,. \tag{4.10}$$

Consequently, the amplitude of the probe field reflected at an interface between a dielectric and such a medium is specified by a reflection coefficient

$$r_\perp^* = \frac{nb-\zeta}{nb+\zeta} = \frac{nb-\sqrt{1+\chi_{\mathrm{eff}}-\alpha^2}}{nb+\sqrt{1+\chi_{\mathrm{eff}}-\alpha^2}} = \frac{nb-\sqrt{\chi_{\mathrm{eff}}+\xi^2}}{nb+\sqrt{\chi_{\mathrm{eff}}+\xi^2}} \,, \tag{4.11}$$

where we have used that $\alpha^2 + \xi^2 = 1$. If we assume a low enough vapor density, such that $|\chi_{\mathrm{eff}}| \ll 1$, we can develop eq. (4.11) to first order in χ_{eff} and get

$$r_\perp^* = \frac{nb-\xi}{nb+\xi} - \frac{nb\chi_{\mathrm{eff}}}{\xi(nb+\xi)^2} \,. \tag{4.12}$$

By comparing eq. (4.9) with eq. (4.12) we see that the effective susceptibility is given by

$$\chi_{\mathrm{eff}} = -\frac{2\mathrm{i}\xi k}{\epsilon_0 E_2} \int_0^\infty \mathrm{d}z P(z) \exp(\mathrm{i}\xi k z) \,. \tag{4.13}$$

4.1.2 Dipole polarization of the atomic vapor

In order to evaluate eq. (4.13) we need to know the polarization density $P(z)$ of the atoms moving in the transmitted field. For this purpose we make the approximation, that the field which is driving the atoms is the same as if the upper half space would be vacuum. This means, that we neglect the field radiated by the atomic polarization in the driving field, which is also known as the Born approximation [94] and is valid for low vapor densities. In this case the driving field is determined by Fresnel's equation and is given by

$$\boldsymbol{E}_2(\boldsymbol{r}) = \hat{\boldsymbol{y}} \frac{2nb}{nb+\xi} E_1 \exp[\mathrm{i}k(\alpha x + \xi z)] \,. \tag{4.14}$$

For the derivation of the dipole polarization we assume the atomic vapor to consist of two level atoms, as introduced in 1.1. The driving field induces a dipole polarization which is determined by the expectation value of the atomic dipole moment

$$\begin{aligned} \langle d \rangle &= \mathrm{tr}(\rho \cdot \boldsymbol{d}) \\ &= d_{12}\rho_{21} + d_{21}\rho_{12} \\ &= d_{12}\tilde{\rho}_{21} \exp(\mathrm{i}\omega t) + d_{21}\tilde{\rho}_{12} \exp(-\mathrm{i}\omega t) \,. \end{aligned} \tag{4.15}$$

The positive frequency part of the dipole moment is therefore proportional to the coherence $\tilde{\rho}_{12}$ which is determined by the optical Bloch equations (1.16). The presence of the interface and the fact that the atoms move imposes boundary conditions in the Bloch equations: if an atom collides with the interface, we assume that it leaves the interface in the ground state and its coherence is lost ($\tilde{\rho}_{12} = 0$). In the case of refraction ($\alpha < 1$) the Bloch equations can be solved in a closed form by the Laplace transform of the density matrix [91]. When $\alpha > 1$, the driving field is evanescent and decays exponentially into the vapor. Hence, the Rabi frequency is a function of z:

$$\Omega(z) = \Omega_0 \exp(-\eta k z) \,, \tag{4.16}$$

with $\Omega_0 = \Omega(z=0) = d_{12}E_2/\hbar$. If we assume the probe field to be weak enough such that the response of the atoms is linear, we can write for the evolution of the coherence to first order in the Rabi frequency

$$\frac{\mathrm{d}}{\mathrm{d}t}\tilde{\rho}_{12}(z(t),t) = \left(\frac{\partial}{\partial t} + v_z \frac{\partial}{\partial z}\right)\tilde{\rho}_{12} = -\left[\frac{\Gamma_0}{2} + \mathrm{i}(\Delta - \alpha k v_x)\right]\tilde{\rho}_{12} + \frac{\mathrm{i}\Omega(z)}{2} \,, \tag{4.17}$$

where we have used that the Doppler shift only contributes in the x direction since there is no phase variation of the driving field in y and z direction. In the steady state eq. (4.17) reduces to a differential equation in z only and reads

$$v_z \frac{\partial}{\partial z}\tilde{\rho}_{12}(z) = -C\tilde{\rho}_{12}(z) + \frac{\mathrm{i}\Omega_0}{2} \exp(-\eta k z) \,, \tag{4.18}$$

where $C = \Gamma_0/2 + \mathrm{i}(\Delta - \alpha k v_x)$. The general solution of eq. (4.18) is given by (see e.g. [95])

$$\begin{aligned}\tilde{\rho}_{12}(z, v_z) &= e^{-C(z-z_0)/v_z}\left[\tilde{\rho}_{12}(z_0) + \int_{z_0}^{z} \mathrm{d}z'\, e^{C(z'-z_0)/v_z}\frac{\mathrm{i}\Omega_0}{2v_z}e^{-\eta k z'}\right] \\ &= \frac{\mathrm{i}\Omega_0}{2}\frac{1}{C-\eta k v_z}\left[e^{-\eta k z} - e^{(C-\eta k v_z)\frac{z_0}{v_z} - Cz/v_z}\right],\end{aligned} \tag{4.19}$$

where z_0 is the position at which the coherence vanishes, which depends on v_z: if $v_z > 0$, the atom leaves the interface at $z_0 = 0$ and $\tilde{\rho}_{12}(z_0) = 0$ due to the prior collision, which leads to the solution

$$\tilde{\rho}_{12}(z, v_z > 0) = \frac{\mathrm{i}\Omega_0}{2}\frac{e^{-\eta k z} - e^{-[\Gamma_0/2 + \mathrm{i}(\Delta - \alpha k v_x)]\frac{z}{v_z}}}{\Gamma_0/2 - \eta k v_z + \mathrm{i}(\Delta - \alpha k v_x)}. \tag{4.20}$$

If $v_z < 0$, the atom arrives from infinity $z_0 = \infty$ where it does not experience any excitation, thus $\tilde{\rho}_{12}(z_0) = 0$ and the solution is given by

$$\tilde{\rho}_{12}(z, v_z < 0) = \frac{\mathrm{i}\Omega_0}{2}\frac{e^{-\eta k z}}{\Gamma_0/2 - \eta k v_z + \mathrm{i}(\Delta - \alpha k v_x)}. \tag{4.21}$$

The dipole polarization of the atomic vapor is then determined by an average over the velocity distribution:

$$\begin{aligned}\boldsymbol{P}(\boldsymbol{r}) = \mathcal{N} d_{12} \exp(\mathrm{i}\alpha k x - \eta k z)\hat{\boldsymbol{y}} \int \mathrm{d}\boldsymbol{v} F_{\mathrm{M}}(\boldsymbol{v}) \,[&\Theta(v_z)\tilde{\rho}_{12}(z, v_z > 0) \\ &+ \Theta(-v_z)\tilde{\rho}_{12}(z, v_z < 0)],\end{aligned} \tag{4.22}$$

where $\mathcal{N}$ is the atom number density, Θ is the Heaviside step function and $F_{\mathrm{M}} = f(v_x)f(v_y)f(v_z)$ is the Maxwell velocity distribution[2] (see section 4.3.2).

Now we can evaluate the effective susceptibility (4.13) using eq. (4.22) and $\xi = \mathrm{i}\eta$ and obtain

$$\begin{aligned}\chi_{\mathrm{eff}} = \frac{2\eta k \mathcal{N} d_{12}^2}{\epsilon_0 \hbar \Omega_0} \int_0^{\infty} \mathrm{d}z \exp(-\eta k z) \int \mathrm{d}\boldsymbol{v} F_{\mathrm{M}}(\boldsymbol{v}) \,[&\Theta(v_z)\tilde{\rho}_{12}(z, v_z > 0) \\ &+ \Theta(-v_z)\tilde{\rho}_{12}(z, v_z < 0)],\end{aligned} \tag{4.23}$$

After performing the integration over z in eq. (4.23), one finds that atoms moving away from the interface give the same contribution as atoms moving towards the interface,

[2] Here we consider a steady state situation and integrate over the z direction. Therefore, we have to use the Maxwell distribution instead of the flux distribution for v_z (section 4.3.2).

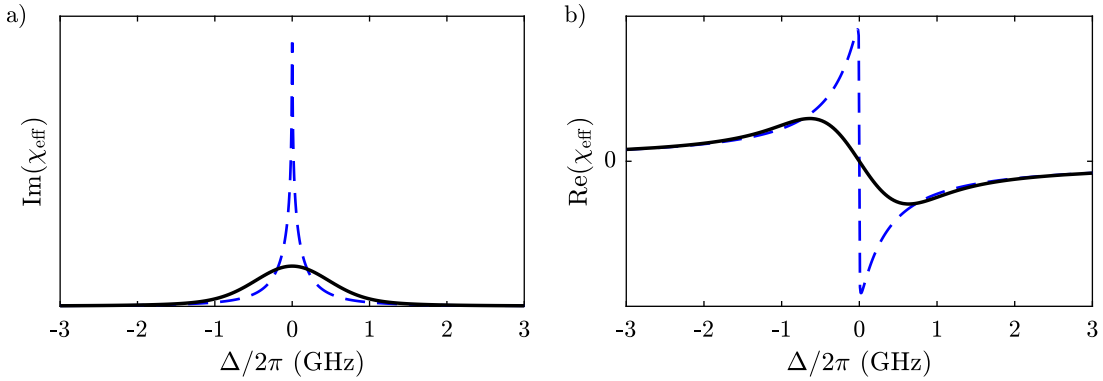

Figure 4.2: Effective susceptibility of a two level atom. a) Imaginary part of χ_{eff}. The blue dashed line shows the effect of transit time broadening without Doppler broadening ($v_x = 0$), whereas the black line shows the full susceptibility, including atoms with $v_x \neq 0$. b) Real part of χ_{eff}.

which is a consequence of the weak probe approximation. The final result for the complex effective susceptibility then reads:

$$\chi_{\text{eff}} = \frac{\mathcal{N} d_{12}^2}{\epsilon_0 \hbar} \int_{-\infty}^{\infty} \mathrm{d}v_x \, f(v_x) \int_{0}^{\infty} \mathrm{d}v_z \, f(v_z) \frac{1}{-(\Delta - \alpha k v_x) - \mathrm{i}(\Gamma_0/2 + \eta k v_z)} \,. \tag{4.24}$$

Examining eq. (4.24) one finds that there are two broadening contributions to the line width of χ_{eff} due to motional effects. First, the Doppler broadening is caused by the Doppler shift in propagation direction, which is enhanced by a factor $\alpha > 1$ compared to free space propagation. In the planar waveguide picture (see Figure 4.1) the Doppler broadening is therefore determined by the propagation constant $\beta_m = n_{\text{eff},m} k = \alpha k$.

Furthermore, there is an additional Lorentzian broadening for each velocity class in z direction caused by the limited transit time of the atoms traveling through the exponentially decaying driving field. The factor $\eta k = \gamma^{-1}$ determines the inverse $1/e$ penetration depth of the evanescent wave.

Figure 4.2 shows the effective susceptibility of a two level atom as a function of detuning Δ. The imaginary part, shown in a), is responsible for the absorption of the evanescent field by the atoms, as we will see later on. The blue dashed line was calculated with $v_x = 0$, hence no Doppler broadening, to point out the effect of transit time broadening. The contribution of different velocity classes in z direction leads to a tapered (non-Lorentzian) line shape. The black line shows the full susceptibility, including all velocity classes in x and y direction. The real part, shown in b), describes the dispersive properties of the atomic medium.

4.1.3 Light propagation in an atomic cladding waveguide

The effective susceptibility eq. (4.24) describes a macroscopic medium which includes the transient effects of the atom-light interaction in the case of total internal reflection. Inside this medium, Maxwell's equations must be extended by the material equation $\boldsymbol{D} = \epsilon_r \epsilon_0 \boldsymbol{E} = (1+\chi)\epsilon_0 \boldsymbol{E}$, where ϵ_r is the relative permitivity of the material. This also affects the wave equation and results in a modified propagation velocity $v = c/\sqrt{1+\chi}$ for plane wave solutions. Therefore the (complex) refractive index of the atomic medium can be defined as

$$n_\mathrm{a} = c/v = \sqrt{1+\chi_\mathrm{eff}}\,. \tag{4.25}$$

This quantity can be used to describe the transmission of a waveguide immersed in atomic vapor. Although χ_eff was derived for an interface which extends to infinity in the x, y directions (analogous to a planar waveguide), the result can also be used for rectangular waveguides to a good approximation.

In order to calculate χ_eff for a certain waveguide geometry, we start with a mode analysis (COMSOL) of the waveguide in a vacuum cladding to obtain the mode profile (and therefore the penetration depth γ, see Figure 2.1) as well as the propagation constant β. These numbers are plugged into eq. (4.24), where $\alpha k = \beta$ and $\eta k = \gamma^{-1}$, in order to calculate the effective susceptibility and therefore, using eq. (4.25) the complex refractive index of the atomic medium. Next, the mode analysis is repeated, but this time with a cladding material which has the refractive index n_a. The result is a modified propagation constant β_a, which determines the propagation of light in the atomic cladding waveguide (eq. (2.1a)):

$$\begin{aligned} \boldsymbol{E}(\boldsymbol{r},t) &= \boldsymbol{\mathcal{E}}_m(x,y)\exp\left[\mathrm{i}(\beta_\mathrm{a} z - \omega t)\right] \\ &= \boldsymbol{\mathcal{E}}_m(x,y)\exp\left[-\mathrm{Im}(\beta_\mathrm{a})z + \mathrm{i}(\mathrm{Re}(\beta_\mathrm{a})z - \omega t)\right]\,. \end{aligned} \tag{4.26}$$

The imaginary part of β_a represents damping along the z direction due to absorption by the surrounding atoms, whereas the real part determines the phase change.

Figure 4.3 shows the propagation constant for a Si_3N_4 ridge waveguide with $h = 180\,\mathrm{nm}$ and $w = 1100\,\mathrm{nm}$ surrounded by a rubidium vapor with a density of $\mathcal{N} = 1.7 \times 10^{13}\,\mathrm{cm}^{-3}$. Here, the total effective susceptibility is composed of the individual hyperfine transitions of the Rb D_2 line with the appropriate weightings. The propagation constant was obtained by a frequency sweep with the detuning Δ around the center frequency of the D_2 line.

Figure 4.3 a) shows the imaginary part of β_Rb, which results in an absorption spectrum within the transmitted light. The line shape of the spectrum exhibits some distinct deviation from the conventional Rb D_2 spectrum in a vapor cell (indicated by the blue line) due to the enhanced Doppler broadening and transit time broadening. Panel b) shows the real part of β_Rb winding around the linear slope of the propagation constant

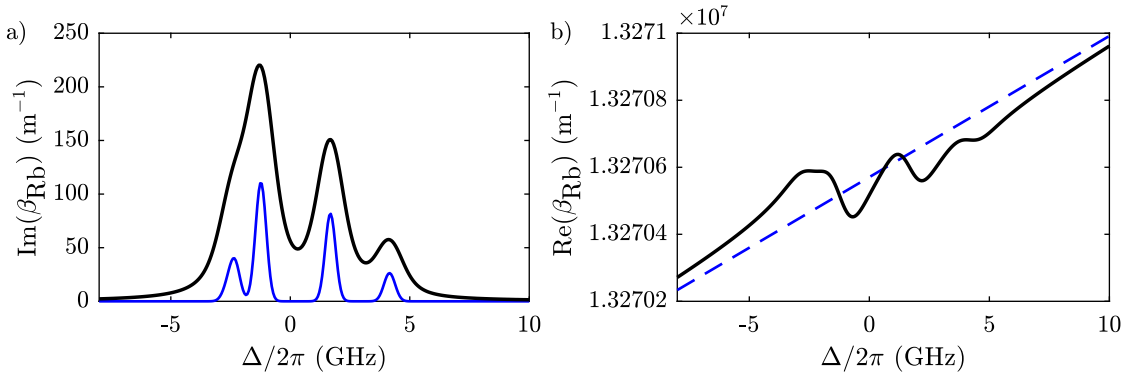

Figure 4.3: Frequency dependent propagation constant β_{Rb} for a waveguide ($h = 180\,\mathrm{nm}$, $w = 1100\,\mathrm{nm}$) surrounded by Rb vapor ($\mathcal{N} = 1.7 \times 10^{13}\,\mathrm{cm}^{-3}$). a) The black line shows the imaginary part of β_{Rb}, responsible for absorption. The blue line indicates the absorption profile for the free space case (arb. amplitude). b) Real part of β_{Rb} (black line). The blue dashed line shows $\mathrm{Re}(\beta)$ in absence of Rb.

in absence of Rb (blue dashed line). The presence of $\mathrm{Re}(\beta_{\mathrm{Rb}})$ becomes relevant in phase sensitive devices, such as the Mach-Zehnder interferometer or ring resonators.

4.2 Atom-surface interactions

The spectroscopy of atoms via the evanescent part of a waveguide mode necessarily involves substantial atom-surface interactions as the probing field amplitude decays within $\sim \lambda/2\pi$ distance from the waveguide surface, where λ is the atomic transition wavelength. These interactions give rise to a shift of the atomic energy levels. Furthermore, the presence of a nearby objects alters the photonic environment of the atom, thus leading to a modified spontaneous emission rate. The interaction between an atom and a macroscopic body is called Casimir–Polder (CP) interaction[3] [96].

To understand the origin of the CP interaction we consider the situation depicted in Figure 4.4. A neutral atom is located at a distance z in front of a dielectric or conducting surface. We assume the atom to be in its ground state and the electromagnetic field to be in its zero-point energy state. Hence, the atomic polarization and the electromagnetic field vanish on average. However, the Heisenberg uncertainty principle states that both the atomic polarization and the electromagnetic field constantly fluctuate. The atom's fluctuating dipole moment induces an image dipole behind the surface. This image dipole has an attractive interaction with the atomic dipole, thus causing a red

[3]We are following the naming convention of [96]. Often, the non-retarded interaction regime is called van der Waals regime and CP is used for the retarded case, while both terms are used to describe atom-atom interactions as well as atom-body interactions.

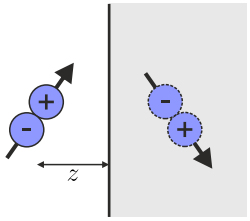

Figure 4.4: Illustration of the atom-surface interaction. An induced atomic dipole at distance z in front of a surface generates an image dipole inside the medium which in turn acts on the atomic dipole via an electromagnetic field.

shift of the atomic transition frequencies[4]. The CP potential is commonly described by the power law

$$U_{\mathrm{CP}}(z) = -\frac{C_\alpha}{z^\alpha}\,, \tag{4.27}$$

where C_α is the coupling coefficient depending on the atomic polarizability and the dielectric permittivity of the surface which determines the strength of the CP interaction and α is an exponent which gradually varies between approximately 3 and 4 depending on the distance z. In the non-retarded regime ($z < \lambda/2\pi$) the interaction between a fluctuating dipole and its image dipole can be calculated using classical electrostatics and was found by Lennard-Jones to take the form of eq. (4.27) with $\alpha = 3$ [98]. In the retarded regime ($z > \lambda/2\pi$) the finite speed of photons leads to a reduction of the interaction strength as was found by Casimir and Polder, such that $\alpha = 4$ in eq. (4.27) [99].

The calculation of CP potentials is commonly performed in the framework of macroscopic quantum electrodynamics (QED) which we will not elaborate on in this thesis. A detailed overview of this concept and practical instructions can be found, for example, in references [96, 100]. In short, the key is to find the classical Green's tensor of the electromagnetic field in the presence of dielectric bodies whose material properties are determined by dielectric permittivities $\epsilon(\omega)$. The CP potential of an atomic state $|j\rangle$ with corresponding polarizability $\alpha_j(\omega)$ is then calculated via perturbation theory as the energy shift due to the coupling between the atom and the body-assisted field.

4.2.1 Casimir–Polder potential near a waveguide

Atoms in the proximity of a waveguide are exposed to different sorts of dielectric materials. For example, an atom above the top side of a waveguide "sees" a material stack

[4]Note, that due to the dispersive properties of a real surface it may occur that an atom resonantly couples to electromagnetic modes of the surface, which can lead to a repulsive interaction and therefore cause a blue shift [97].

composed of Al_2O_3, Si_3N_4 and SiO_2. A first approach to calculate the CP potential is to consider a planar multilayer system of infinite extension for which analytical expressions for the Green's tensor are known [96, 101]. However, the dimensions of the structures typically vary on a sub-wavelength scale, thus the infinite plane approach is not suitable over the entire geometry. In such a case one has to apply numerical techniques like the discrete dipole approximation (DDA) [102]. The basic idea is to approximate an arbitrary geometry by a set of discrete cells, each of them acting as a point dipole. These dipoles interact with the incident field from a fluctuating atomic dipole and also with each other. The scattering quantities required to calculate the atom-surface interaction then can be obtained from the individual polarizations.

In order to obtain the CP shift Δ_{CP} of the Rb $5^2\mathrm{P}_{3/2} \rightarrow 5^2\mathrm{S}_{1/2}$ transition line, the CP potentials of the individual $5^2\mathrm{P}_{3/2}$ and $5^2\mathrm{S}_{1/2}$ levels are calculated and subtracted from each other. While the CP potential of the ground state involves emission and reabsorption of virtual photons from a continuous (non-resonant) frequency range, an atom in an excited state can emit real photons of discrete (resonant)frequency when going through a transition to a lower lying state. Therefore, the potential of an excited state is the sum of a non-resonant part and a resonant part, whereas the ground state potential is of the non-resonant form [100]. The consequence of the CP shift in our experiment is an overall redshift of the line shape as well as an asymmetric red tail due to atoms at different distances to the surface obtaining different line shifts. Exemplary DDA result[5] for Δ_{CP} are shown in Figure 4.5 a) for a 75 nm Si_3N_4 slot waveguide (see chapter 7 for details on the waveguide structure). In the vicinity of the surface the transition frequency is red shifted and $|\Delta_{\mathrm{CP}}|$ rapidly falls off with increasing distance. The emission of real photons from the excited state gives rise to an oscillating contribution in the resonant potential, leading to a zero crossing of the line shift at larger distance (dark blue area and white dashed line). This can be understood as an interference effect between the emitted photon and the photon re-emitted by the image dipole.

Figures. 4.5 b) and c) serve to analyze the differences between the infinite plane approach and the DDA method for the calculation of Δ_{CP} around a waveguide. Figure 4.5 b) shows a detail of the waveguide cross section as indicated by the red dashed box in Figure 4.5 a). Here, the solid black lines are equipotential lines of Δ_{CP} calculated with the DDA method (Δ_{DAA}), whereas the dashed lines are calculated using the infinite plane approach (Δ_{p}) with the corresponding material stacks below the respective surfaces. This plot shows clearly the importance of taking into account the real geometry in the domains around any edges. On the other hand, there are regions with negligible deviation between the two methods above plane surfaces with larger extent, except for atoms being in immediate proximity to the surface. This discrepancy can be attributed to discretization errors due to the finite cell size of 2.5 nm in

[5] The DDA calculations presented in this work have been performed by Helge Dobbertin in the group of Prof. Stefan Scheel at the Uni Rostock.

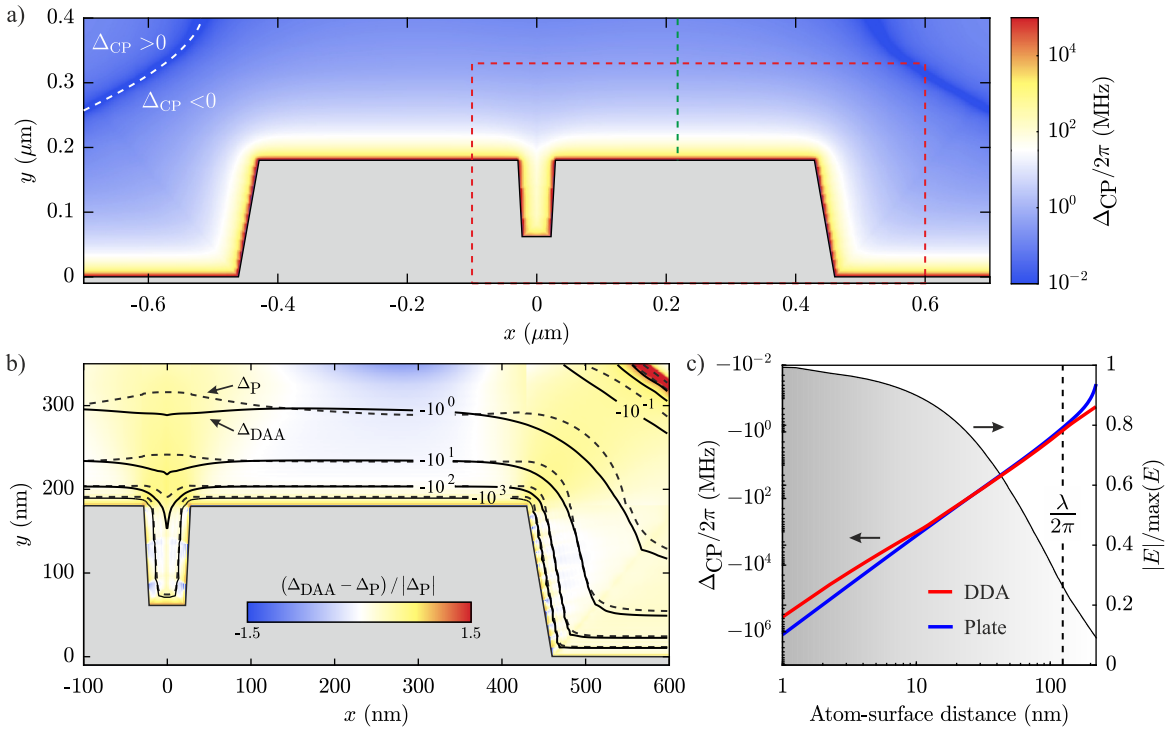

Figure 4.5: Casimir–Polder shift in the vicinity of a 75 nm slot waveguide. a) Spatial dependence of Δ_{CP} calculated with the DDA approach. The red dashed box and green dashed line indicate the regions of panel b) and c), respectively. b) Comparison between DDA (Δ_{DAA}) and infinite plane results (Δ_p). Equipotential lines are shown for Δ_{DAA} (solid) and Δ_p (dashed) where the given values are in MHz. Encoded in color is the relative difference between the two results. c) Line shift above the top side of the waveguide (left ordinate) calculated with the DDA and infinite plane approach. The material order in this case is 7 nm Al_2O_3 (protection coating), 175 nm Si_3N_4 (core material) and infinitely thick SiO_2 (substrate). The gray area shows the normalized electric field of the fundamental waveguide mode (right ordinate). DDA calculations performed by H. Dobbertin.

the DDA simulation. However, at such small atom-surface distances the macroscopic assumptions behind the presented theory become questionable anyway. To examine the two methods more closely, Figure 4.5 c) shows the CP shift above the top side of the waveguide along the green dashed line in Figure 4.5 a). For distances between 10 nm and 100 nm both results agree well. Atoms in this region also contribute the largest part to the spectroscopy signal since for greater distances the evanescent probe field is already significantly damped as indicated by the gray area, whereas for shorter distances the CP interaction shifts the atoms way out of resonance.

Casimir–Polder force

The CP potentials do not only influence the atomic level structure but also lead to an electromagnetic force acting on a neutral atom, which is given by

$$\boldsymbol{F}(\boldsymbol{r}) = -\nabla U^j_{\mathrm{CP}}(\boldsymbol{r})\,. \tag{4.28}$$

Note, that an atom in its ground state experiences a different force than an atom in its excited state determined by the particular potential U^g_{CP} and U^e_{CP}, respectively. Close to the waveguide the CP force is attractive in both cases and accelerates the atom towards the surface.

Under the conditions of our experiments the atoms already exhibit a relatively large initial velocity ($\langle v\rangle \approx 350\,\mu\mathrm{m}\,\mu\mathrm{s}^{-1}$ for Rb at $T = 150\,^{\circ}\mathrm{C}$) such that the atomic trajectories are affected by the CP force only within a few nanometers distance to the surface. The influence of the CP force on the local atomic density can be estimated using [103]

$$\mathcal{N}(z) = \frac{\mathcal{N}(\infty)}{k_{\mathrm{B}}T}\int_0^\infty e^{-E/k_{\mathrm{B}}T}\sqrt{\frac{E}{E - U^j_{\mathrm{CP}}(z)}}\,\mathrm{d}E\,, \tag{4.29}$$

where E is the energy of the atom. For $T = 150\,^{\circ}\mathrm{C}$ and considering the potential shown in Figure 4.5 c), the local density at a distance of 4 nm to the surface is estimated to be $\mathcal{N}(4\,\mathrm{nm}) > 0.99 \times \mathcal{N}(\infty)$. We have obtained a similar result from Monte Carlo simulations of atom trajectories (see section 4.3). Consequently, the CP force can be neglected in the temperature regime of the experiments presented in this work.

4.2.2 Spontaneous emission rate near a waveguide

The spontaneous emission of a photon from a quantum emitter like an excited atom is not a property of the emitter (atom) itself, but depends on its environment, as was first pointed out by Purcell [104]. More specifically, the emission rate is proportional to the strength of the vacuum electric field fluctuations at the position of the atom [105]. The presence of a dielectric body modifies the magnitude and distribution of

these vacuum field fluctuations, which results in an altered spontaneous emission rate relative to the free space value Γ_0. This effect becomes significant if the atom is located within a distance $d \leq \lambda/2\pi$ to the dielectric surface due to the presence of evanescent waves.

The magnitude of the vacuum fluctuations at the atom's position is given by the imaginary part of the aforementioned Green's tensor [106], which is also a measure for the local density of states (LDOS) [107]. An exemplary result obtained with the DDA approach for the modified decay rate Γ of the Rb $5P_{3/2}$ state in the vicinity of a 75 nm Si_3N_4 slot waveguide is shown in Figure 4.6 a). Here, the calculated total emission rate $\Gamma = (2/3)\Gamma_{\parallel} + (1/3)\Gamma_{\perp}$ is averaged over all dipole orientations. Close to the surface, Γ shows a marked increase due to the presence of guided modes and substrate radiation modes. A special feature of slot waveguides is the strong electric field confinement in the low index region inside the slot which gives rise to an increased LDOS and hence a particularly high spontaneous emission rate. Far from the material boundaries Γ approaches the free space value Γ_0, as expected.

Emission into guided modes

An excited atom close to a dielectric structure can decay into either radiation or guided modes [108], where the radiation modes can be divided into substrate radiation modes which are evanescent in the vacuum region and fully radiative modes which leave the region as outgoing plane waves. To obtain the emission rate into a certain waveguide mode, the Green's tensor can be expanded into a corresponding basis [109]. In a waveguide with low losses the emission rate of a randomly oriented dipole into mode m takes the form [110]

$$\Gamma_m(x,y) = \frac{\pi c^3 \epsilon_0 |\boldsymbol{\mathcal{E}}_m(x,y)|^2}{2\omega^2 P_m} \Gamma_0 \,, \tag{4.30}$$

where $\boldsymbol{\mathcal{E}}_m$ is the electric field distribution of the mode and $P_m = \frac{1}{2}\int (\boldsymbol{\mathcal{E}}_m \times \boldsymbol{\mathcal{H}}_m)\,\mathrm{d}\boldsymbol{A}$ is the corresponding mode power, which can both be conveniently obtained from a numerical mode solver, such as COMSOL. The sum of emission rates into guided modes $\Gamma_{\mathrm{M}} = \sum_m \Gamma_m$ of the 75 nm Si_3N_4 slot waveguide is shown in Figure 4.6 b). Inside the slot up to 40 % of the atomic emission is channeled into guided modes, whereof the dominant part is emitted into the fundamental mode with the rate $\kappa = \Gamma_{\mathrm{TE0}}$, as shown in Figure 4.6 c).

The emission of a single photon into a well defined mode is an important goal in quantum-optics experiments. The efficiency with which an emitter couples to a specific mode is commonly described by the parameter $\beta = \kappa/\Gamma$. In the presented example of a slot waveguide β can reach decent values, even without optical feedback from a cavity. However, if the emitter is an atom within a thermal gas, the main dissipation mechanism is set by the atomic motion (non-radiative decay).

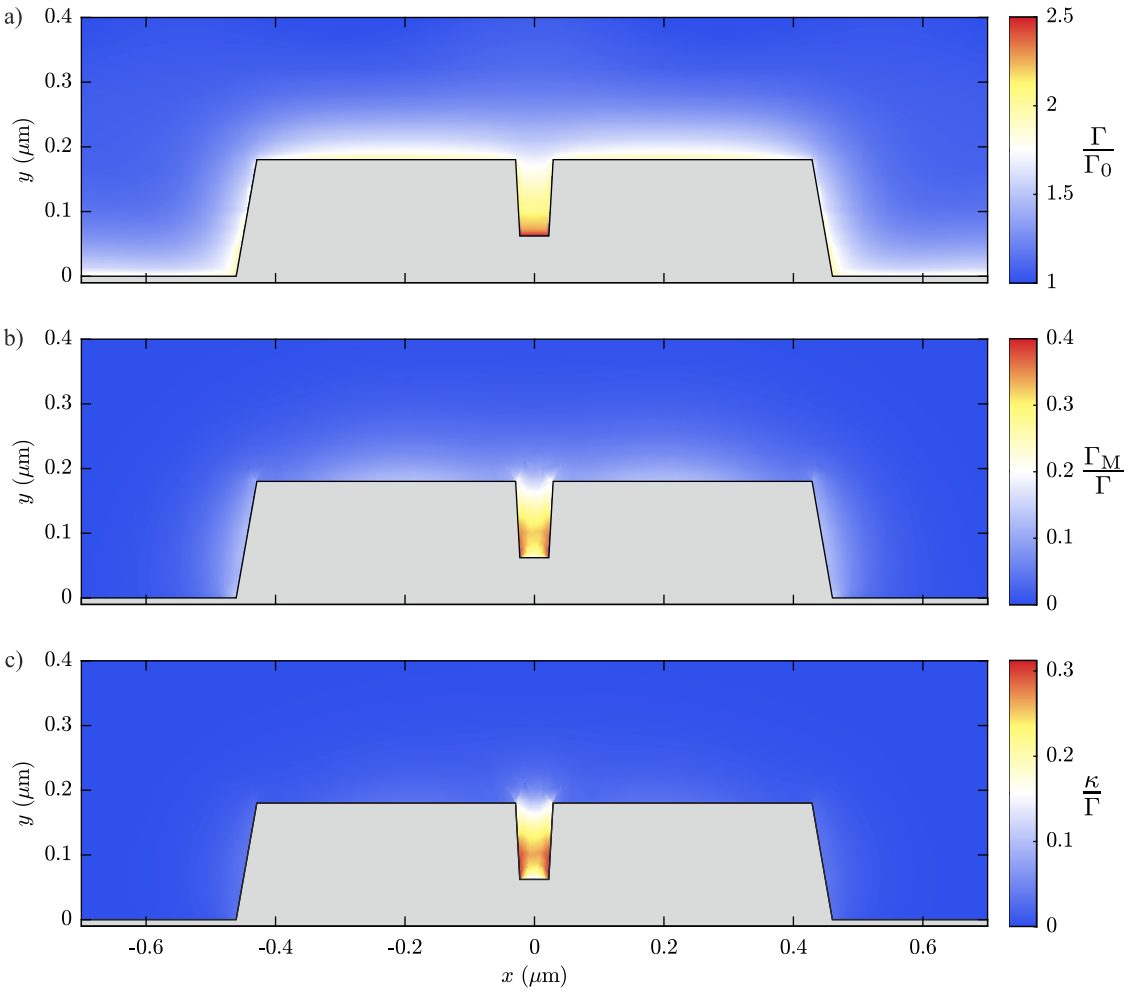

Figure 4.6: Spatial dependence of the emission rate of the Rb $5P_{3/2}$ state close to a 75 nm Si_3N_4 slot waveguide. a) Total spontaneous emission rate Γ normalized by the free space value Γ_0. b) Fraction of emitted energy coupled into guided modes of the waveguide. c) Fraction of emitted energy into the fundamental TE0 mode. Note that losses due to atomic motion are not considered here. DDA calculations performed by H. Dobbertin.

4.3 Monte Carlo simulation

The effective susceptibility method specified in an earlier section has its limitations and cannot account for non-trivial spatial dependencies, for example, the actual mode profile or waveguide geometry. If these factors become important, it is preferable to use the Monte Carlo type simulation described in the following in order to model the interaction between an atomic vapor and a waveguide mode.

In this approach we trace individual atoms moving around the waveguide and calculate the evolution of their density matrix. The arguments entering the optical Bloch equations are updated according to the momentary positions and velocities of the atoms. Thus, the Rabi frequency and the environment assisted decay rate are determined by the position of the atom. Furthermore, the detuning is given by the distance between the atom and any surface of the geometry due to Casimir–Polder interactions, as well as the atom's velocity because of the Doppler shift. Transient effects are inherently included in this simulation, since, on the one hand, the actual trajectory of an atom through the evanescent field is considered, and on the other hand, atom-surface collisions are handled with the corresponding effects on the density matrix.

4.3.1 General procedure

The simulation volume is bounded by a rectangular box around the waveguide cross-section with dimensions $w_x \times w_y \times w_z$, where in most cases $w_x = 2\,\mu\text{m}$ and $w_y = w_z = 1\,\mu\text{m}$. The following description refers to two-level atoms but the general procedure can also be adapted to multi-level atoms. For each atom, the time-dependent optical Bloch equations (1.16) are solved numerically with a fourth-order Runge–Kutta method [111] for a set of detunings Δ. In the initialization step, N atoms are randomly placed within the simulation box and are given random velocities sampled from a Maxwell-Boltzmann distribution, see section 4.3.2. Then time advances gradually and in each time step the position and the density matrix of every atom is re-calculated. The individual Rabi frequencies $\Omega(\boldsymbol{r})$, total decay rates $\Gamma(\boldsymbol{r})$, decay rates into the fundamental mode $\kappa(\boldsymbol{r})$ and effective detunings $\Delta_{\text{eff}}(\boldsymbol{r}, v_z) = \Delta - \Delta_{\text{CP}}(\boldsymbol{r}) - \beta v_z$ which enter the optical Bloch equations are updated with respect to the momentary position and velocity. Here, Δ_{CP} is a shift of the resonance frequency due to the Casimir–Polder (CP) potential $U_m(\boldsymbol{r})$, see section 4.2, and βv_z is the Doppler shift, where β is the propagation constant of the waveguide mode. A particular waveguide geometry is implemented with the original dimensions and the corresponding modes are used to calculate the Rabi frequencies and decay rates into these modes. Whenever an atom collides with the waveguide surface or hits the transversal boundary of the simulation box, we assume that it gets deexcited and its coherences are set to zero. In the subsequent time step the atom leaves the surface in its ground state with a new direction and speed according to Knudsen's cosine law [112] (see section 4.3.2). In reality, the atom might stick to the surface for a

certain time, however, adsorption and desorption rates are identical after a dynamical equilibrium has been reached for a given temperature, so it is reasonable to assume that the atom leaves the surface instantly after a collision. Most of the experiments in this work have been conducted in a density regime where the mean free path is longer than the size of the cell[6] and we can therefore neglect collisions between atoms. For the longitudinal direction we use periodic boundary conditions, such that an atom which passes though one side of the box enters on the opposite side with the same velocity and density matrix. This is justified as long as the length of the waveguide is much larger than its transversal extent and the system can be assumed to be invariant along the longitudinal direction.

We run the simulations for a certain time $T = n_t \times \Delta t$ (usually a few hundred nanoseconds up to microseconds) with n_t time steps and discard the first few nanoseconds which are required to reach a steady state. It is favorable to run multiple independent realizations for the same parameters in parallel, each with a fraction of the total atom number, and afterwards average over these realizations to shorten the overall computation time.

4.3.2 Velocity distributions

In thermodynamic equilibrium the instantaneous velocity distribution of non-interacting atoms inside a given volume is determined by the Maxwell distribution [113]. The probability of finding an atom with velocity between v_i and $v_i + \mathrm{d}v_i$, $(i = x, y, z)$ is

$$F_{\mathrm{M}}(\boldsymbol{v})\mathrm{d}\boldsymbol{v} = f(v_x)f(v_y)f(v_z)\,\mathrm{d}v_x\,\mathrm{d}v_y\,\mathrm{d}v_z\,, \tag{4.31}$$

where the probability distribution for each independent direction is given by

$$f(v_i) = \frac{1}{\sigma\sqrt{2\pi}}\exp\left(-\frac{v_i^2}{2\sigma^2}\right)\,, \tag{4.32}$$

where $\sigma = \sqrt{k_{\mathrm{B}}T/m}$ is the variance of the distribution, which depends on the mass of the atom m and the product of Boltzmann's constant k_{B} and the temperature T. Transforming eq. (4.31) into spherical coordinates, we obtain the distribution function for atoms with speeds $(v = |\boldsymbol{v}|)$ between v and $v + \mathrm{d}v$:

$$f_{\mathrm{s}}(v) = 4\pi\left(\frac{1}{2\pi\sigma}\right)^{3/2} v^2\exp\left(-\frac{v^2}{2\sigma^2}\right)\,. \tag{4.33}$$

For an atom leaving a surface after a collision the situation is different. The probability of an atom leaving (or crossing) a surface during a unit interval of time is linearly proportional to the velocity component v_{n} in the direction normal to the surface:

$$g(v_{\mathrm{n}}) = Cv_{\mathrm{n}}f(v)\,, \tag{4.34}$$

[6]The only exception are the measurements described in section 7.3.

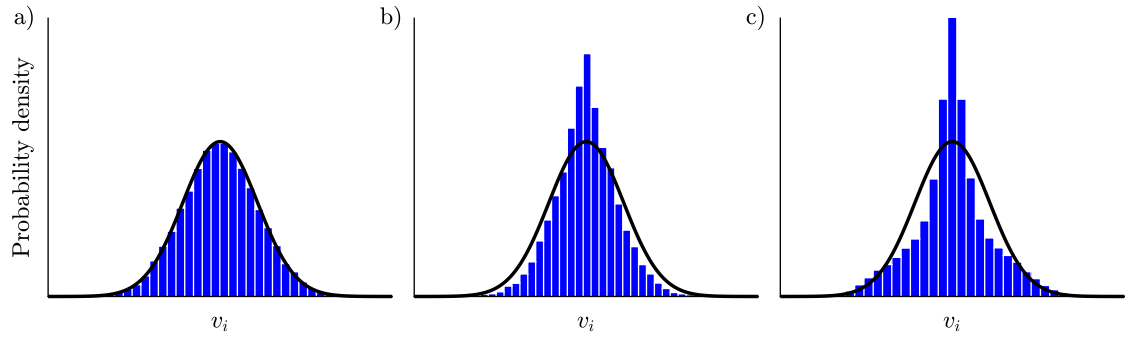

Figure 4.7: Distribution of velocity components v_i, $(i = x, y, z)$ inside the simulation volume for different cases of desorption. The black line shows the calculated probability density according to eq. (4.32). a) Atoms obeying Knudsen's cosine law during desorption. b) Desorption with solely Maxwellian velocity components. c) Directed desorption $\propto \cos^{10}\theta$.

where C is a proportionality constant which has to be determined such that the probability distribution is normalized:

$$\int_0^\infty \mathrm{d}v_\mathrm{n}\, C v_\mathrm{n} f(v_\mathrm{n}) = 1 \;\rightarrow\; C = \frac{\sqrt{2\pi}}{\sigma}\,. \tag{4.35}$$

Consequently, the resulting expression for the normal velocity distribution is given by

$$g(v_\mathrm{n}) = \frac{1}{\sigma^2} v_\mathrm{n} \exp\left(-\frac{v_\mathrm{n}^2}{2\sigma^2}\right)\,. \tag{4.36}$$

This type of function is also known as the probability density function of the Rayleigh distribution [114]. The relation to Knudsen's cosine law [112] becomes clear, as v_n is proportional to the cosine of the angle between the surface normal and the velocity vector: $v_\mathrm{n} = \boldsymbol{v} \cdot \hat{\boldsymbol{n}} = v \cos \sphericalangle(\boldsymbol{v}, \hat{\boldsymbol{n}})$.

The distribution of the tangential velocity components is of the volume type eq. (4.32), so that the distribution function for an atom leaving (or striking) a surface has the form

$$F_\mathrm{C}(\boldsymbol{v}) = f(v_\mathrm{t1}) f(v_\mathrm{t2}) g(v_\mathrm{n})\,, \tag{4.37}$$

where $v_\mathrm{t1}, v_\mathrm{t2}$ are the tangential velocity components. Equation (4.37) is also known as the "flux" distribution [115].

Figure 4.7 illustrates the importance of choosing the proper velocity for an atom after a surface collision. Here we show the distribution of the velocity components of 10 000 atoms inside the simulation volume after 100 ns simulation time for different desorption cases: one according to the flux distribution eq. (4.37) with $g(v_\mathrm{n})$ given by eq. (4.36) ($\cos\theta$), another one with all three velocity components sampled from

the Maxwell distribution, and one with a more directed distribution ($\cos^{10}\theta$). It can be seen, that only atoms which follow the cosine law during desorption reproduce a Maxwellian velocity distribution inside the volume. Several experiments verified the cosine law for atoms desorbing from a surface using evanescent wave spectroscopy in a non-equilibrium situation [116, 117] and by scanning a probe laser beam along the cross section of a vapor cell [118]. Moreover, the validity of the cosine law for atom-surface reflections was mathematically proven in [119]. These findings do, however, not exclude desorption distributions other than the cosine type. Only the sum of all desorption contributions needs to be cosine in an equilibrium [115]. In fact, there has been evidence for non-cosine distribution in many desorption experiments, see e.g. [120–122]. Hence, one would have to take into account the actual microscopic mechanisms behind the desorption from individual surfaces for a more realistic modeling of the experiment. For lack of knowledge about the microscopic surface structure and due to limited computational resources, we set up the simulation such that we obtain an equilibrium distribution within the simulation volume.

4.3.3 Retrieving spectroscopic quantities

The data obtained in an atomic cladding waveguide experiment is typically a transmission spectrum. In order to compare the simulations with the experimental data, one needs to find the fraction of the input power missing in the transmitted light for a certain detuning. Hence we have to determine how much light is scattered by the atoms into free space or into the waveguide mode in both forward and backward direction. Also, we need to register the accumulated excited-state fraction of the atoms at the instance they collide with a surface or the transversal simulation boundary[7]. We write for the total scattered power inside the simulation volume

$$P_{\mathrm{sc}}(\Delta) = \hbar\omega_0 \sum_{\Delta t} \sum_{i=1}^{N} \left[\left(\Gamma(\boldsymbol{r}_i, t) - \frac{\kappa(\boldsymbol{r}_i, t)}{2} \right) \times \frac{\rho_{22}(\boldsymbol{r}_i, t, \Delta_{\mathrm{eff}})}{n_t} + \frac{\rho_{22}^{\mathrm{col}}(\boldsymbol{r}_i, t, \Delta_{\mathrm{eff}})}{T} \right], \tag{4.38}$$

where ρ_{22} denotes the population probability[8] of an atom inside the simulation volume and ρ_{22}^{col} is the population probability of an atom which undergoes a surface collision at time step t. The inner sum runs over all atoms inside the simulation volume and the outer sum takes care of time averaging. The first term within the square brackets accounts for the scattered power due to the decay of the excited state which is determined by Γ. A fraction of the atoms decays into the forward propagating fundamental

[7] We do not have to account for collisions with the longitudinal boundaries, as we apply periodic boundary conditions in this direction.

[8] Here, we omit the tilde which indicates the rotating wave approximation as introduced in section 1.1.

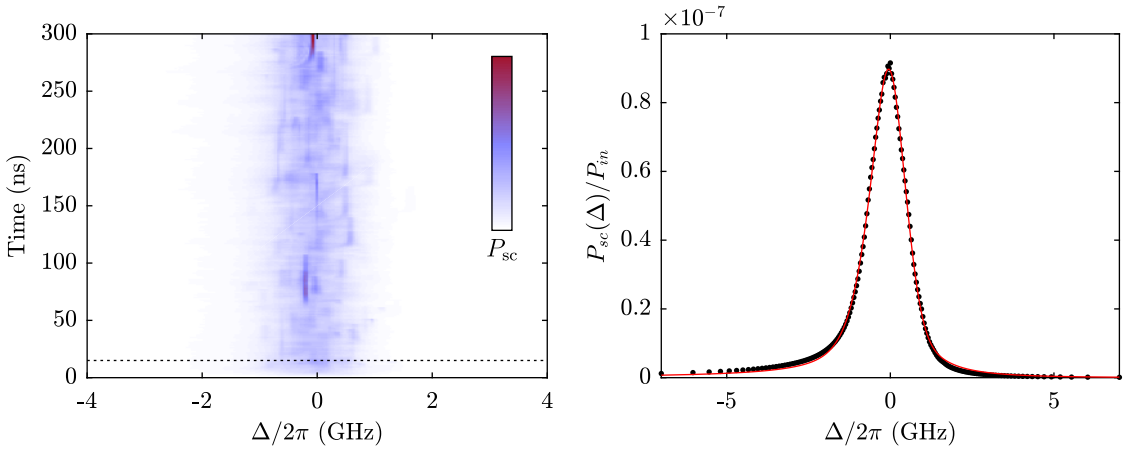

Figure 4.8: Results of a Monte Carlo simulation for a ridge waveguide. a) Evolution of the signal as a function of detuning. The dashed line indicates the point in time, after which integration of the signal begins. b) Scattered power normalized to the input power (black dots) with the corresponding pseudo Voigt fit (red line).

mode with a rate $\kappa/2$ and has to be subtracted from the total scattered power as this portion is added to the observed transmission signal. Excitation losses due to surface collisions are included via the second term.

Figure 4.8 shows the time evolution of the simulation signal as well as the final steady state result for a ridge waveguide ($w = 900\,\text{nm}$, $h = 180\,\text{nm}$) with $N = 2000$ atoms, 171 detuning steps and an integration time of $T = 300\,\text{ns}$. A suitable way to extract spectroscopic quantities, such as line width, line shift and amplitude of the signal, is to fit an asymmetric pseudo Voigt function[9] to $P_{\text{sc}}(\Delta)$, indicated by the red line in Figure 4.8 b).

4.3.4 Comparison to the effective susceptibility method

It is instructive to compare the results obtained with the Monte Carlo simulations (MCS) to the effective susceptibility method (ESM) described in section 4.1. For this purpose we consider a ridge waveguide ($w = 1100\,\text{nm}$, $h = 180\,\text{nm}$) with thermal atoms at 150 °C. Since atom-surface interactions are not included in the ESM, we have ignored them in the MCS as well for this discussion.

First, we look at transit time effects, as they should be accurately accounted for in the MCS. The results for both methods with the Doppler effect disabled are shown in Figure 4.9 a). The tapered line shape with a broad pedestal is obtained by either

[9]See Appendix B for details.

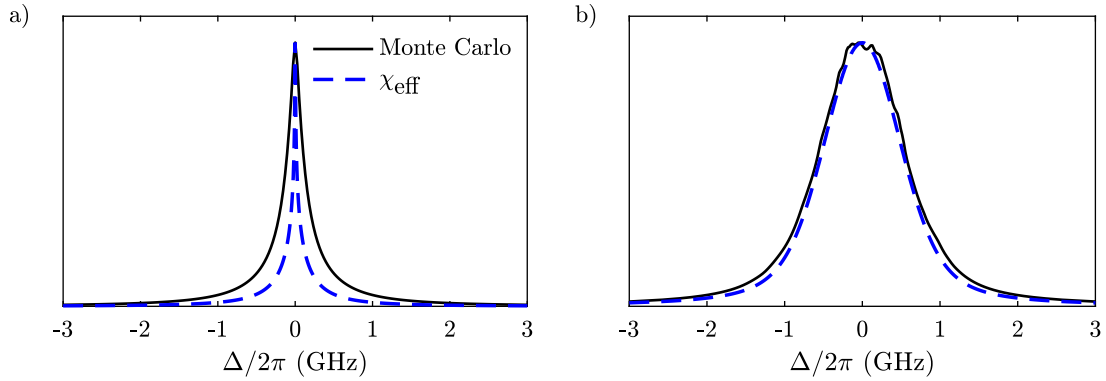

Figure 4.9: Comparison between the Monte Carlo and the effective susceptibility methods. The signals are P_{sc} for the MCS and $\text{Im}(\chi_{\text{eff}})$ for the ESM, which are both normalized to their maximum value for better comparison. a) Transit time broadened features (Doppler effect disabled). b) Complete signals, including the Doppler effect.

method and is very similar, except for the absolute width of the feature, which is quite narrow in the ESM case ($2\pi \times 50\,\text{MHz}$ FWHM vs. $2\pi \times 260\,\text{MHz}$ FWHM). This can be understood from the fact the ESM only accounts for one transit direction, namely along the normal of the interface between dielectric and atomic vapor, whereas the MCS includes realizations of many trajectories, some of which can intersect the evanescent field on very short paths.

Figure 4.9 b) shows the full results, including all velocity components. The influence of the Doppler effect is implemented in both methods via an additional detuning $-\beta v$, with the difference that in the MCS the velocity is randomly sampled from the Maxwell distribution, whereas in the ESM the susceptibility is integrated over all velocity classes with a weighting according to the Maxwell distribution. An agreement in the Doppler width is therefore expected, and as it contributes the major part of the line width, the relative difference is not as significant as in Figure 4.9 a). Applying a Voigt fit to both signals reveals a total line width of $2\pi \times 1190\,\text{MHz}$ for the ESM and $2\pi \times 1260\,\text{MHz}$ for the MCS.

4.4 Waveguide transmission measurement

For a characterization of the spectroscopy with integrated structures, we investigated the most elementary device, shown in Figure 4.10 a). It consists of a ridge waveguide ($w = 900\,\text{nm}$, $h = 180\,\text{nm}$) with grating couplers at either end. The Si_3N_4 structures were written into positive photoresist, which is why most of the chip area is covered by Si_3N_4 and the structures are actually defined by removing material around their edges.

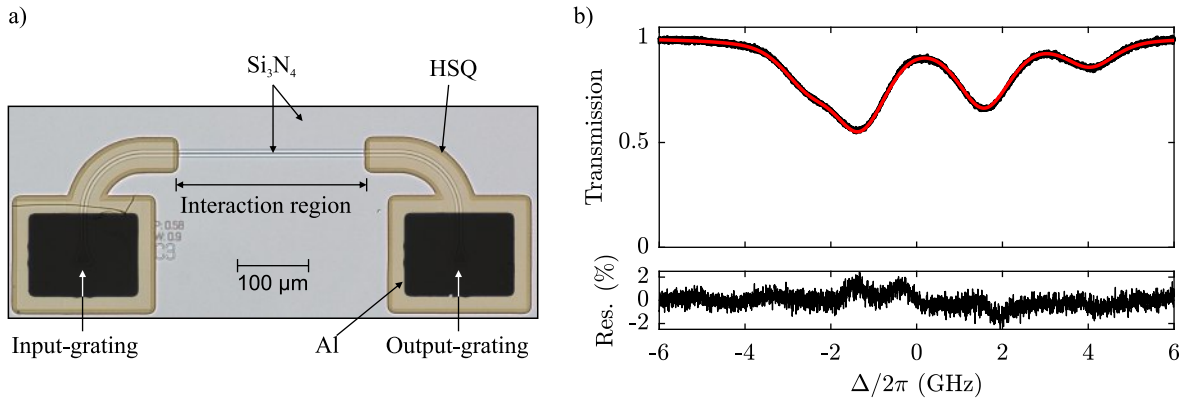

Figure 4.10: Transmission through an atomic cladding waveguide. a) Microscopy image of the waveguide structure. b) Transmission spectrum of the waveguide at a density of $\mathcal{N} \approx 8.5 \times 10^{13}\,\mathrm{cm}^{-3}$. The trace is normalized to the off-resonant transmission level. The red line is a fit of the model to the data (black line). The residuals (Res.) underneath show the difference between data and fit.

The whole device is covered by a HSQ layer, except for a 260 µm long section within which the waveguide is exposed to the atomic vapor (interaction region).

A transmission spectrum of the device is shown in Figure 4.10 b) for a frequency scan over the Rb D_2 line at a density of $\mathcal{N} \approx 8.5 \times 10^{13}\,\mathrm{cm}^{-3}$. The laser which is sent to the chip has a power of 20 nW, which is reduced by few orders of magnitude inside the waveguide core due to coupling losses. The corresponding intensity is therefore well below the saturation intensity which has been determined to be reached at an input power of $\sim 3\,\mu\mathrm{W}$ in a power dependent measurement series.

Also shown in Figure 4.10 b) is a fit of a transmission function for the Rb D_2 line, based on the asymmetric Voigt function (see Appendix B). The residuals below indicate that this model fits the data very well. From the fit we determine the line width to be $\Gamma_{\mathrm{tot}}/2\pi = 1302 \pm 2\,\mathrm{MHz}$. Assuming a Doppler width of $\Gamma_{\mathrm{D}}/2\pi = kn_{\mathrm{eff}}\sigma\sqrt{8\ln(2)} = 1025.9\,\mathrm{MHz}$, we can estimate the transit time broadening to be[10] $\Gamma_{\mathrm{TT}}/2\pi \approx 474\,\mathrm{MHz}$.

The optical depth (OD) for the Rb^{85} $5S_{1/2}$, F= 3 $\rightarrow$ $5P_{3/2}$ transition is ~ 0.6 for the given density and waveguide length. For comparison, a laser beam propagating through a cell with a thickness that matches the length of the waveguide and contains Rb vapor at the same density would experience an OD of 13.5, assuming the line widths are the same as above. Taking into account that the fraction of optical power in the cladding is $\eta \approx 8.8\,\%$, we get an effective OD of 1.2, which is in the same order as the value

[10] The Lorentzian FWHM Γ_{L} can be approximately calculated from the Voigt FWHM Γ_{V} and the Gaussian FWHM Γ_{G} by [123]: $\Gamma_{\mathrm{L}} = 7.7258\Gamma_{\mathrm{V}} - 2.8903\sqrt{5.415\Gamma_{\mathrm{V}}^2 + 1.7310^14\Gamma_{\mathrm{G}}^2}$. However, the transit time broadened line shape is not exactly Lorentzian, as we have seen above and the result should only be taken as an estimate.

determined from the waveguide transmission spectrum. The discrepancy is most likely due to the deviation of the actual density from the density estimated from the reservoir temperature[11].

Comparison to the effective susceptibility model

The data from the measurement above is well suited to test the effective susceptibility model from section 4.1, due to the comparatively simple waveguide geometry in this experiment.

After calculating the propagation constant β_{Rb} for the corresponding experimental parameters, the transmission spectrum of the waveguide can be obtained by the following equation:

$$T = \exp\left[-2\mathrm{Im}(\beta_{\mathrm{Rb}})l\right] , \tag{4.39}$$

where l is the length of the interaction region. Figure 4.11 shows the result of eq. (4.39) together with the experimental data. The agreement is remarkably good, given that the position of the center frequency is the only free fit parameter, as frequency shifts due to atom surface interactions are not included in this model. From this fit we determine that the waveguide spectrum is shifted by $-2\pi \times 64\,\mathrm{MHz}$ against the spectrum of a reference cell. The slight overestimation of the optical depth is in accordance with the comparison above and suggests a lower density in the cell as expected from the adjusted reservoir temperature.

Based on the satisfactory prediction of the OD and line width of the calculated spectrum, this model seems to be adequate for describing the interaction between an atomic vapor and the evanescent field of a simple ridge waveguide.

Monte Carlo simulation results

Now we also want to use the data from this experiment to examine the quality of the Monte Carlo simulation introduced in section 4.3. For the calculation of the atom-surface potentials, the C_3 coefficients derived for an atom in front of an infinite surface have been used in this case. Figure 4.11 b) shows the result of a simulation run with $N = 2000$ atoms, 171 detuning steps and an integration time of $T = 300\,\mathrm{ns}$.

From a fit to the resulting line shape, we infer a line width of $\Gamma_{\mathrm{tot}}/2\pi = 1346 \pm 12\,\mathrm{MHz}$ and a line shift of $\Delta_0/2\pi = 75 \pm 4\,\mathrm{MHz}$. Both values are reasonably close to experimentally measured values, with 3 % deviation in the line width and 15.6 % deviation in the line shift. The increased discrepancy in the line shift is expected, since the atom-surface potentials are included under the approximation described earlier.

[11] In this case, the density would correspond to a temperature of 138 °C instead of the 150 °C set point for the values to agree.

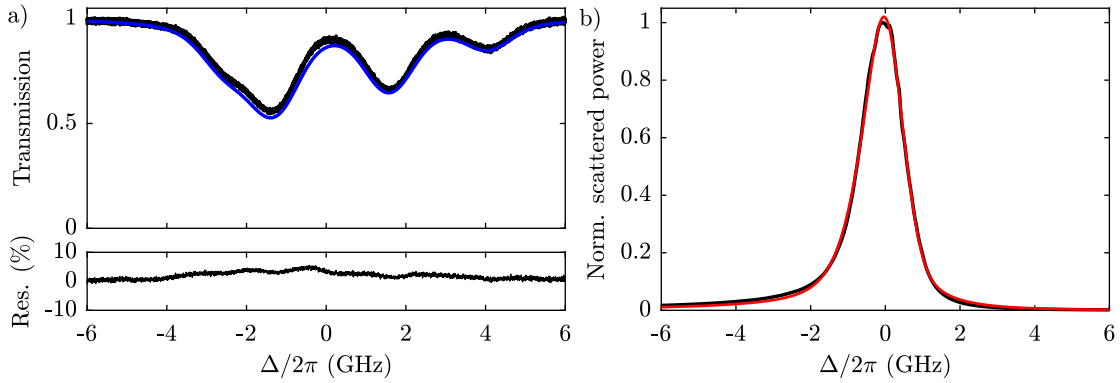

Figure 4.11: Results of the two models for the waveguide transmission. a) Transmission spectrum obtained with the effective susceptibility method (blue line) together with the experimental data (black line) with no free parameters, except the frequency center. The residuals (Res.) underneath show the difference between data and model. b) Normalized scattered power obtained from the Monte Carlo simulation (black line) and fit (red line).

The exaggerated atom-surface interaction also affects the line width indirectly, as the resulting distribution of line shifts leads to a broadening of the spectrum. If we repeat the simulation run with the atoms-surface interaction deactivated, we obtain a line width of $\Gamma_{\mathrm{tot}}/2\pi = 1310 \pm 7\,\mathrm{MHz}$, which is remarkably close to the experimental value.

4.5 Losses due to alkali metal exposure

It has become apparent that exposing the photonic structures to a saturated alkali metal vapor leads to increased transmission losses of the devices. For a regular waveguide, this simply leads to a reduced output power. However, for the ring resonators the additional losses cause a broadening of the resonances and eventually renders them unobservable. We have witnessed this effect to happen over the course of a few minutes during the initial heat up of the reservoir, immediately after the cell was filled with rubidium. In order to keep the alkali exposure to a minimum at times when no measurement was run, we kept the cell at high temperature[12] while having the reservoir heater switched off. Even with these "recovery cycles" the overall transmission dropped irreversibly over time, hence the useable lifetime of the chips was limited.

To quantify the additional losses we introduce the attenuation coefficient α_{Rb}, such

[12] Typically, the cell temperature was set to 150 °C to 180 °C for this process, which caused the reservoir to be at $\sim$ 50 °C due to thermal coupling.

Chip	Device	Rb exposure time (days)	α_{Rb} (µm^{-1})
NGE06	Short waveguide D3	48	3.6×10^{-3}
NGJ16	EIT AA4	18	3.4×10^{-3}
NGJ16	EIT BB4	13	1.9×10^{-3}
NGJ21	Short waveguide A1	11	3.5×10^{-3}
NGJ21	Short waveguide A2	11	8.7×10^{-4}
NGJ21	Short waveguide A2	27	1.81×10^{-2}

Table 4.1: Attenuation coefficients extracted for several devices by comparing their transmission properties before and after exposing the chip to rubidium for several days.

that the total transmission of a waveguide with an interaction length l is given by

$$T = T_0 \times e^{-\alpha_{\mathrm{Rb}} l}\,, \tag{4.40}$$

where T_0 is the original transmission determined by the coupling losses and intrinsic losses of the device. Some devices have been characterized before filling the cell with Rb, which gives us a knowledge of T_0. Therefore, we can extract α_{Rb} using eq. (4.40), the results being listed in table 4.1. The Rb exposure time is the total time after filling the cell including several measurement- and recovery-cycles.

The actual mechanism of the alkali atom induced losses is unknown up to now, however, one reasonable explanation is the formation of a thin metallic layer or clusters on the waveguide surface. It is known, and has also been observed in our experiments, that the walls of vapor cells (usually made of SiO_2) undergo a curing process after filling with alkali metal for the first time until a saturated vapor pressure is achieved [124, 125]. According to [126, 127], the first layer of adsorbed alkalis on oxide surfaces is relatively strong bonded and the binding is assumed to have ionic character, whereas in excess of one monolayer (ML), the alkalis form metallic clusters which desorb at relatively low temperatures. To desorb the initially adsorbed atoms requires much higher temperatures ($\gtrsim 600\,\mathrm{K}$ for Na on SiO_2 [126]). Although our waveguide core material is silicon nitride instead of an oxide, the adsorption mechanism described before should be similar. This is due to the fact that Si_3N_4 is thermodynamically unstable in air and oxidizes, such that a thin film of SiO_2 forms on the waveguide surface [128–130].

The optical properties of a metal can be explained by a plasma model[13], where collisions of the free electrons with the ion cores result in a damping of the electromagnetically driven electron oscillation [131]. This damping gives rise to a complex dielectric

[13]For alkali metals, this model is valid for frequencies up to the ultraviolet [131].

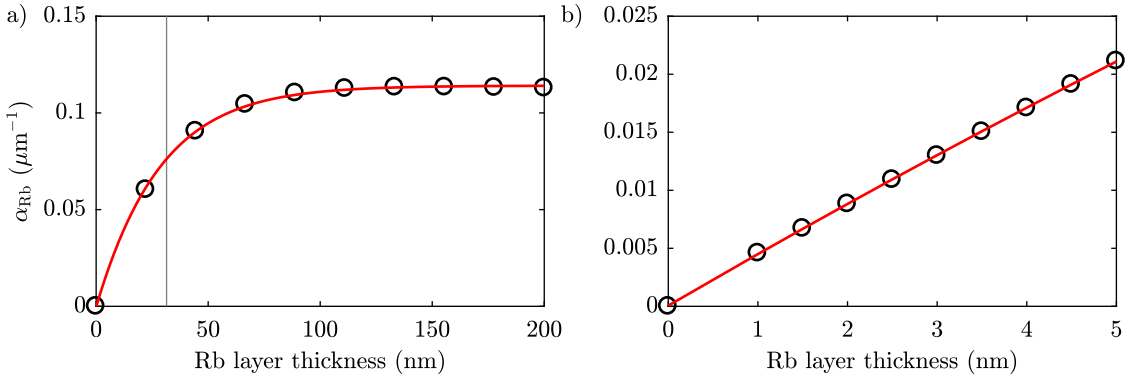

Figure 4.12: Simulated attenuation coefficient of a Rb covered waveguide. a) 2D model with a large range of layer thicknesses. The red curve is a fit of $-\log\left[\alpha_{\max} + \exp(-bd_{\mathrm{Rb}})\right]$, where $\alpha_{\max}$ and b are material dependent parameters. The gray vertical line indicates the skin depth of Rb at $\lambda = 780\,\mathrm{nm}$. b) Results of the 3D model with fit.

function of the metal, the imaginary part of which is causing absorption of the electromagnetic field. In order to estimate the losses caused by a thin Rb layer we performed simulations within COMSOL, where we applied a metallic layer to the waveguide surface. This layer has been implemented via a transition boundary condition with the dielectric function of Rb taken from [125]. Because the implementation of a 3D model with a very thin conductive layer is computationally demanding, we started with a 2D model to obtain the relevant effects caused by adsorbed Rb. Figure 4.12 a) shows the attenuation coefficient α_{Rb} extracted from the simulated transmission of a Si_3N_4 waveguide as a function of Rb layer thickness. After a rapid increase the losses saturate at $\alpha_{\mathrm{Rb}} \approx 0.11\,\mu\mathrm{m}^{-1}$, since the thickness of the metal layer which is "seen" by the waveguide mode is limited by the skin depth[14], which is $\sim 31\,\mathrm{nm}$ at $\lambda = 780\,\mathrm{nm}$ (calculated using the values from [125]).

For a better comparison of the experimentally observed losses to this model, we also performed full 3D simulations based on a ridge waveguide ($w = 800\,\mathrm{nm}$, $h = 175\,\mathrm{nm}$), where the thickness of the Rb layer was limited due to the previously mentioned computational effort. The results are shown in Figure 4.12 b) and are in the same range as the values listed in table 4.1. From this, we can very roughly estimate the average thickness of the metallic layer to be $\sim 1\,\mathrm{nm}$, corresponding to ~ 2.3 monolayers[15] of rubidium. In [124] it has been found, that a cured vapor cell made of Pyrex glass has about 6-7 ML of Rb on its walls, which is in the same order.

Of course, this estimation should be taken with caution, since we have assumed a

[14] The skin depth is the distance into the metal at which the intensity amplitude of an electromagnetic field is reduced by $1/e$.

[15] Assuming 1 ML $= 2 \times r_{\mathrm{Rb}}$, where $r_{\mathrm{Rb}} = 220\,\mathrm{pm}$ is the covalent radius of Rb [132].

Compound	ΔGf^0 (kJ mol^{-1})	Compound	ΔGf^0 (kJ mol^{-1})
Cs_2O	-308.2	K_2O	-240.6
Al_2O_3	-1582.3	Si_3N_4	-647
SiO_2	-856.4	MgO	- 568.9
TiO_2	-883.3		

Table 4.2: Gibbs free energy of formation ΔGf^0 for a few alkali metal oxides and relevant compounds for the fabrication of photonic structures and protection coatings. Values taken from [135].

continuous layer of Rb (instead of clusters [133, 134]) with the same properties as the bulk material. The roles of surface defects, edges and corners have not been taken into account. Also, we only considered an average value of the few available attenuation coefficients listed in table 4.1. The large variation of these values may be attributed to different surface conditions of the samples (surface texture and purity, degree of oxidization, defects, etc.). Nevertheless, the considerations made above support our hypothesis of metallic rubidium on the waveguide surface being the reason for the witnessed transmission losses. A further evidence is the sudden increase of transmission that we observed after venting the vacuum chamber of the early experiments[16]. During the venting the adsorbed alkali reacts with the oxygen and water vapor contained in the ambient environment and therefore is no longer metallic.

4.5.1 Protection coating

Since the deterioration of the waveguide performance seems to depend on its surface properties, it might be beneficial to coat the waveguides with an extra layer of a different material which does not substantially affect the mode characteristics. It has been reported that aluminum oxide (Al_2O_3) is a suitable candidate for a protection coating in an alkali environment and can increase the resistance of vapor cells by two orders of magnitude [136, 137]. There are two possible mechanisms assumed to play a role in the interaction between SiO_2 and alkali metals: the diffusion into the bulk material [138] and the reduction of SiO_2 by the alkali [136]. Both possibilities remain valid for an Al_2O_3 coating, but the latter should be less likely since the absolute value of the Gibbs free energy for the formation of Al_2O_3 is much higher than that of SiO_2, whereas both values are higher than for Cs_2O [17] (see table 4.2).

[16] In one case we quantified the transmission after venting to be ~ 120 times the transmission under vacuum and Rb atmosphere.

[17] We take Cs_2O as a reference instead of Rb_2O since the Gibbs energy of formation for the first one is available.

We have tried Al_2O_3 protection coatings on the last two chip generations with a thickness of 9 nm. According to [136], a 6 nm thick layer of Al_2O_3 should be sufficient for a good protection. The layer was grown by atomic layer deposition (ALD), a technique allowing for a conformal and pinhole-free coating of the nanostructures. A further advantage of the ALD coating is the reduction of scattering losses due to smoothening of the waveguide surface [139]. With this coating it was possible to observe the resonances of the ring resonators in combination with rubidium vapor, which was not the case for the bare Si_3N_4 devices. However, the line width of the resonances was still increased by a factor of around five compared to the resonances of an unexposed chip. The ring resonances remained observable after four months, although the round trip transmission factor seemed to be slightly decreased with respect to the freshly filled cell ($\tau \approx 0.7$ as to $\tau \approx 0.73$).

Our findings suggest that the deposition of a 9 nm thick Al_2O_3 protection layer indeed reduces the degradation of the photonic structures in an alkali vapor environment. However, this method is still not sufficient to avoid alkali induced losses completely and further studies are required to clarify the underlying mechanisms and to develop a better protection strategy.

5 Integrated Mach-Zehnder interferometer

The Mach-Zehnder interferometer (MZI) is a simple tool to translate relative phase changes between two light paths into intensity changes. Light entering the MZI passes a beam splitter and is divided into two parts which are then recombined by another beam splitter. The relative phase acquired along the two paths determines the intensity at a particular output port. This property makes the MZI suitable for optical sensing of refractive index changes or tiny length changes on the order of less than a wavelength.

In this chapter we investigate the waveguide version of the MZI and use it to measure phase changes due to the presence of rubidium atoms. The entire interferometer has a footprint of less than a square millimeter and is an example for the compactness of integrated photonic devices. This chapter is largely based on reference [140].

5.1 Theory of operation

The schematic of an integrated MZI is shown in Figure 5.1 a). The in-coupled light is split by means of a 50/50 Y junction into two arms consisting of curved waveguides with a path difference of $\Delta l = l_2 - l_1$. The lower arm (1) is completely covered with HSQ, whereas the upper arm (2) is only partially covered, therefore offering a region of length l_A for the guided mode to interact with the surrounding atoms via the evanescent field. The modes from both arms are recombined with a second Y junction where they interfere. The output power depends on the relative phase between the modes of arm 1 and arm 2 at the combiner and is given by

$$T_\mathrm{MZI} = \left|U_1 \exp[\mathrm{i}(\beta_1 l_1 + \phi_0)] + U_2 \exp[\mathrm{i}(\beta_1(l_2 - l_\mathrm{A}) + \beta_\mathrm{Rb} l_\mathrm{A})]\right|^2 , \tag{5.1}$$

where U_1, l_1 and U_2, l_2 are the light amplitudes and lengths of arm 1 and arm 2, respectively. The propagation constant for a waveguide covered with HSQ is denoted as β_1, whereas β_Rb is the complex propagation constant for a Rb cladding, as described in section 4.1.3. The additional phase term ϕ_0 accounts for a temperature dependent change of the arm lengths.

The calculated transmission of an MZI in the absence of Rb is shown in Figure 5.1 b) for two different cases. In the absence of propagation losses and for a perfect 50/50

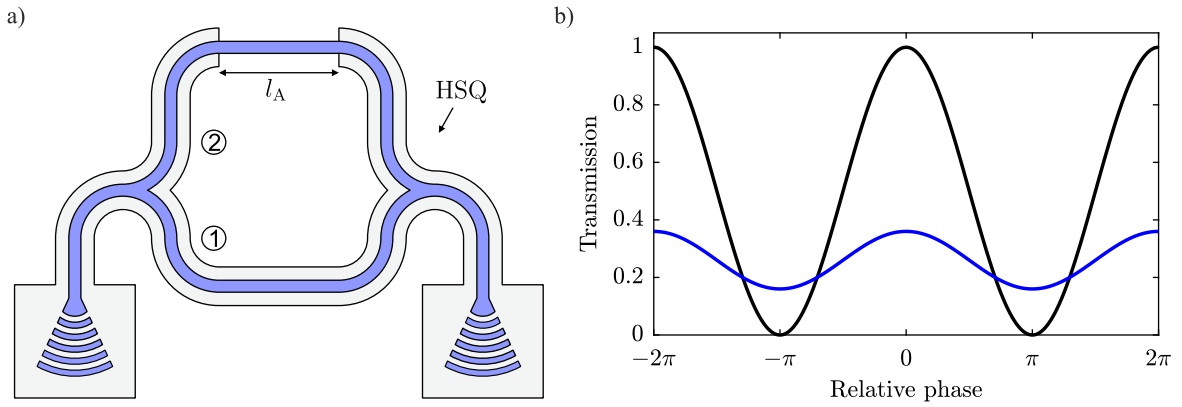

Figure 5.1: The integrated waveguide MZI. a) Schematic structure of an MZI composed of two Y junctions. The waveguide core and the grating couplers (blue) are covered with HSQ (gray) except for the interaction region l_A in arm 2. b) Calculated transmission depending on the relative phase of the light fields at the combining Y junction for different amplitude ratios: $U_1 = U_2$ (black line), $U_2 = 1/5\,U_1$.

splitting ratio the fringes exhibit maximum contrast[1], as shown by the black line. Any deviation of the two amplitudes at the combining Y junction leads to a loss of contrast (blue line).

Aside from propagation losses, some of the light in the uncovered arm gets absorbed by the surrounding atoms, which is why the MZI transmission signal contains information about both real and imaginary part of the effective vapor susceptibility.

5.2 Atomic phase shift measurements

The Mach-Zehnder interferometer for the phase sensitive measurements is based on Si_3N_4 waveguides with a width of $w = 1100\,\text{nm}$ and a height of $h = 180\,\text{nm}$. The length of the covered arm 1 is $l_1 = 500\,\mu\text{m}$ whereas arm 2 has a total length of $l_2 = 2.5\,\text{mm}$ with an uncovered length of $l_A = 2\,\text{mm}$. Figure 5.2 shows Rb D_2 transmission spectra of the MZI for different atom densities and an input power of 280 nW. The spectra have been fitted with (5.1) based on the effective susceptibility model, where the Rb density, the amplitudes of the individual arms, and the phase offset are free fit parameters. The panels of Figure 5.2 a) show the MZI transmission over a larger detuning range with and without contribution from the atoms. The transmission of the bare MZI has been calculated using (5.1) with the parameters obtained from the fit.

[1]The fringe contrast (or visibility) is defined as the ratio of fringe amplitude to average transmission: $C = \frac{\max(T)-\min(T)}{\max(T)+\min(T)}$.

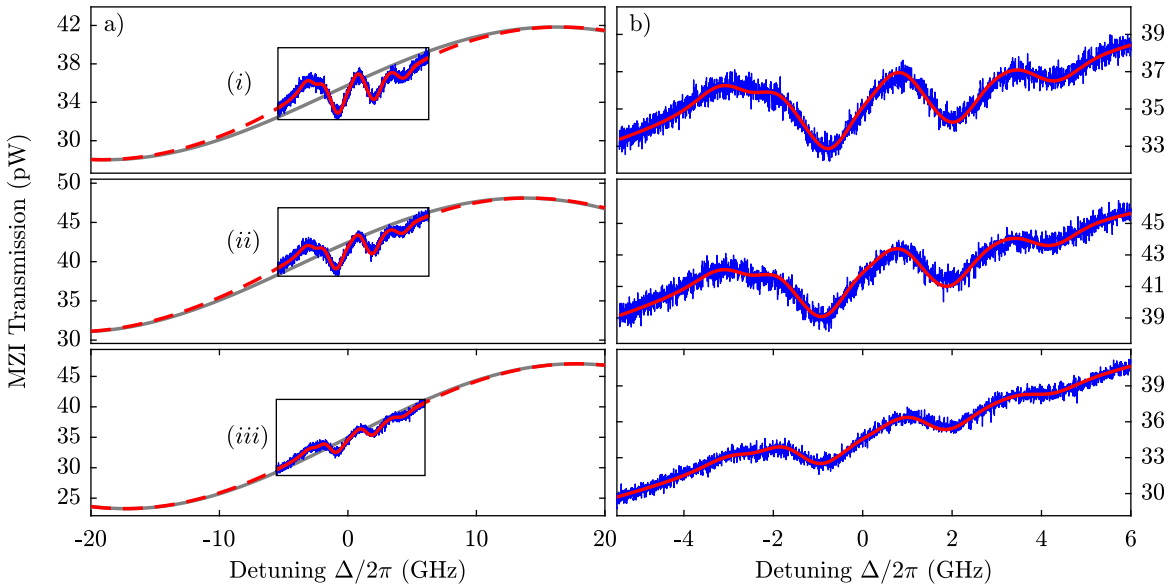

Figure 5.2: Transmission through a waveguide MZI with $l_A = 2\,\text{mm}$. a) The gray solid lines show the calculated transmission of the MZI without any coupling to the atoms with a free spectral range of FSR $\approx 71\,\text{GHz}$. The insets contain the experimental traces (blue) for various atomic densities $\mathcal{N} = 2.4 \times 10^{13}\,\text{cm}^{-3}$ (i), $\mathcal{N} = 1.4 \times 10^{13}\,\text{cm}^{-3}$ (ii), $\mathcal{N} = 6 \times 10^{12}\,\text{cm}^{-3}$ (iii). The solid red line is the theory fit while the red dashed line is the calculated transmission including the atomic contributions outside the scan range of the laser. Far off resonance this curve smoothly approaches the empty MZI fringe. b) Zoom in on the insets from a) with the experimental data (blue) and the theory fit (red).

Furthermore, one can deduce that the amplitude in arm 2 is approximately ten times smaller the amplitude in arm 1 and decreasing over the course of the experiment, thus causing a smaller visibility than expected from a 50/50 beam splitter. This behavior can be attributed to the larger length of arm 2 and therefore higher (intrinsic) propagation losses on the one hand. On the other hand, as discussed in section 4.5, the exposed waveguide additionally suffers from losses due to rubidium atoms adsorbed on its surface.

The most intriguing feature of a Mach Zehnder interferometer is of course its ability to measure phase shifts. We now can extract this phase shift $\Delta\varphi$ due to the presence of the atoms from our data transforming equation 5.1 and subtracting the phase shift of the bare MZI:

$$\Delta\varphi = \cos^{-1}\left(\frac{T_{\text{MZI}} - |U_1|^2 - |U_2|^2 \exp\left(-2\,\text{Im}(\beta_{\text{Rb}})l_A\right)}{2U_1U_2 \exp\left(-\,\text{Im}(\beta_{\text{Rb}})l_A\right)}\right) - \left[\beta_1 l_1 - \left(\beta_1(l_2 - l_A) + \beta_0 l_A\right)\right], \tag{5.2}$$

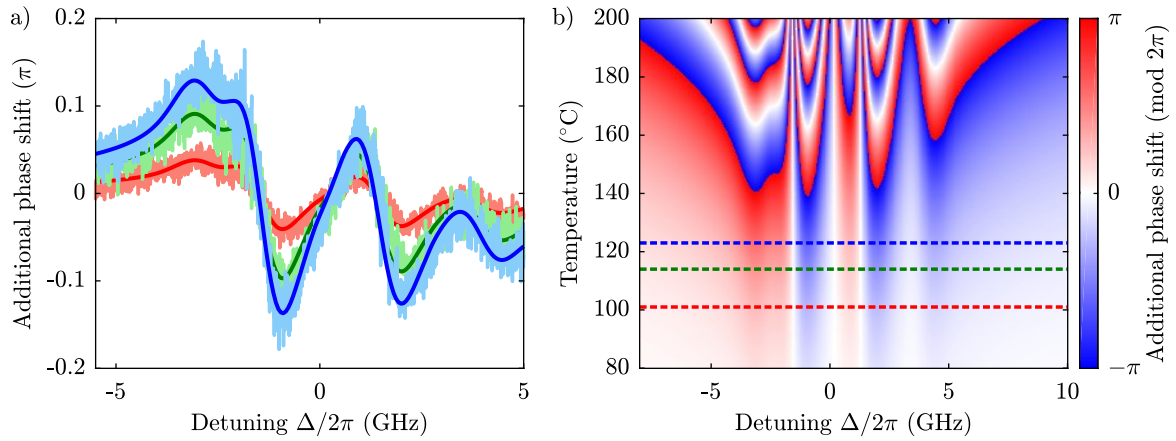

Figure 5.3: Additional phase shift in the MZI. a) The bright traces show the phase shift extracted from the data for atomic densities $\mathcal{N} = 2.4 \times 10^{13}\,\mathrm{cm}^{-3}$ (blue), $\mathcal{N} = 1.4 \times 10^{13}\,\mathrm{cm}^{-3}$ (green), $\mathcal{N} = 6 \times 10^{12}\,\mathrm{cm}^{-3}$ (red). The dark curves are the corresponding calculated phase shifts for the parameters obtained from the fits in Figure 5.2. b) Calculated additional phase shift by the atoms modulo 2π as a function of detuning and reservoir temperature. Dashed lines indicate the positions of the data from a).

where β_0 is the propagation constant in the waveguide without cladding (vacuum). Figure 5.3 a) shows the phase shifts corresponding to the data in Figure 5.2. For the data with the highest atomic density of $\mathcal{N} = 2.4 \times 10^{13}\,\mathrm{cm}^{-3}$, the light experiences an additional phase shift of up to $0.15 \times \pi$. In Figure 5.3 b) the calculated atomic phase shift for this particular device is shown in dependence of the reservoir temperature. One can extrapolate from this model, that an additional phase of π is reached at a temperature of 160 °C, corresponding to an atomic density of $\mathcal{N} = 1.7 \times 10^{14}\,\mathrm{cm}^{-3}$. Naturally a higher density is accompanied by strong absorption, however the imaginary part of the susceptibility drops off quadratically with detuning whereas the real part drops off linearly. Hence, an off-resonant phase shift can be obtained without much attenuation. Nevertheless, we did not further increase the reservoir temperature and hence the atomic density in this experiment, since we intended to keep the reservoir temperature well bellow the chip temperature in order to keep the amount of Rb condensation at a minimum. Since this experiment was performed in the old vacuum chamber setup, we were not able to safely increase the chip temperature even further.

Eventually, the magnitude of the refractive index of an atomic vapor is fundamentally limited due to resonant dipole-dipole interactions [141, 142]. The increase in the effective susceptibility with higher density is compensated by the self broadening of the resonance which leads for rubidium to a maximum refractive index of $n_{\mathrm{Rb}} \approx 1.4$ [143].

6 Coupling thermal atoms to ring resonators

The interaction between atoms and photons can be boosted by making the photon pass the atom multiple times, which can be achieved using an optical resonator. In integrated optics, a simple and widespread resonator design is the ring resonator consisting of a circular waveguide closed to a loop and a bus waveguide to couple light into and out of the ring. This type of resonator in combination with thermal rubidium atoms will be investigated in this chapter. For these first experiments we chose a rather large ring radius to tune the ring resonance with moderate temperature changes to the atomic transition frequency. However, the resulting large mode volume and especially the alkali induced round trip losses prevented us from observing any enhancement in the coupling strength. This chapter is largely based on reference [144]. The interaction of thermal atoms with ring resonators has been proposed theoretically in reference [42]. Similar experiments have been conducted by the group of Uriel Levy [43].

First, we introduce the theory of a bare ring resonator as well as a ring resonator surrounded by atomic vapor. This is followed by a characterization of the devices before and after bringing them in contact with rubidium, which drastically alters their performance due to rubidium atoms sticking to the waveguide surface. Then we experimentally investigate the resonant interaction between rubidium and the ring mode. Finally, an excursion into the field of cavity quantum electrodynamics will be made to evaluate our system in this context and to estimate the potential of different resonator designs.

6.1 Theory

The ring resonator with radius R is evanescently coupled to a bus waveguide terminated with grating couplers as illustrated in Figure 6.1 a). To analyze the exchange of power between the waveguide and the ring one can treat the coupling region like a beam splitter as indicated by the dashed box [145, 146]. The relations between the complex mode amplitudes are then given by

$$\begin{aligned} \mathcal{E}_2 &= r\,\mathcal{E}_1 + \mathrm{i}t\,\mathcal{E}_3 \\ \mathcal{E}_4 &= r\,\mathcal{E}_3 + \mathrm{i}t\,\mathcal{E}_1\,, \end{aligned} \tag{6.1}$$

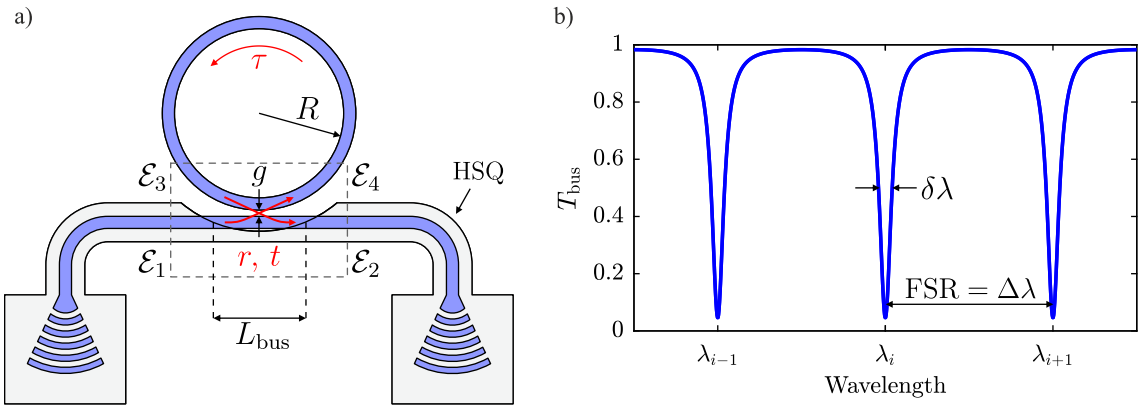

Figure 6.1: Waveguide ring resonator. a) Schematic of a ring resonator with radius R coupled to a bus waveguide separated by the distance g. The gray area depicts the HSQ cover layer. Coupling is described with a beam splitter formalism as indicated by the dashed box. b) Bus waveguide transmission spectrum with free spectral range (FSR) $\Delta\lambda$ and resonance line width $\delta\lambda$.

where r and t are the coupling parameters satisfying the condition $r^2 + t^2 = 1$. The coupling is determined by the size of the gap g between ring and waveguide and is assumed to be lossless in this analysis. Inside the ring the light circulation is described by

$$\mathcal{E}_3 = \tau e^{\mathrm{i}\phi} \mathcal{E}_4 \,, \tag{6.2}$$

where τ is the round-trip transmission factor and $\phi = 2\pi R\beta$ is the phase acquired after one round-trip, with β being the propagation constant of the ring mode. Combining equations (6.1) and (6.2) the intensity transmission of the bus waveguide can be obtained:

$$T_{\text{bus}} = \left| \frac{\mathcal{E}_2}{\mathcal{E}_1} \right|^2 = \frac{\tau^2 - 2r\tau\cos\phi + r^2}{1 - 2r\tau\cos\phi + r^2\tau^2} \,. \tag{6.3}$$

Figure 6.1 b) shows T_{bus} as a function of input wavelength with $r = 0.9$ and $\tau = 0.85$. Near resonance, when $\phi = 2\pi q$ ($q = 0, \pm 1, \pm 2, ...$), the transmission drops due to destructive interference. This effect is illustrated in Figure 6.2 for $tau = 1$ which shows the results of a ring resonator simulation within COMSOL. It can be seen that the field in the bus waveguide and the field returning from the ring are out-of-phase and therefore interfere destructively. In the special case when $r = \tau$, i.e. when the internal resonator loss matches the transmission loss in the coupler, the bus waveguide output becomes zero. This situation is called critical coupling.

The ring resonator is characterized by certain figures of merit which are reflected in the transmission spectrum. The distance between two resonances is called the free spectral

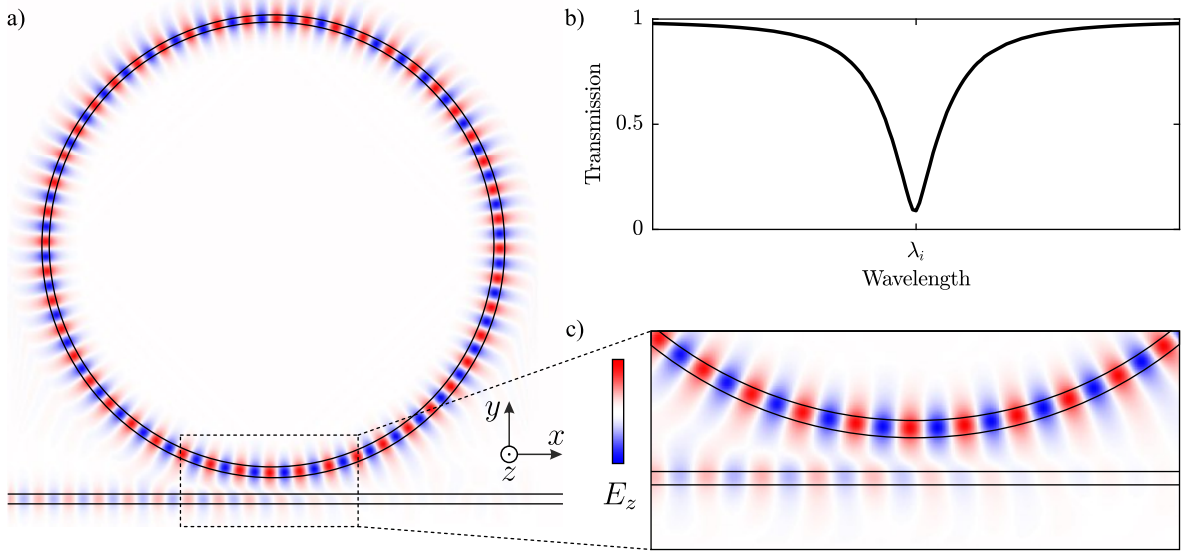

Figure 6.2: Electric field simulation of a ring resonator with $\tau = 1$. a) E_z component for the resonant wavelength. Part of the incoming field in the bus waveguide is coupled over to the ring and likewise from the ring back to the bus waveguide. The field returning from the ring (left side) is out-of-phase with the incoming field of the bus waveguide, see close up in c) for better visibility, which is why the transmission drops due to destructive interference. Conversely, constructive interference leads to a amplitude build up inside the ring which is much higher than the amplitude in the bus waveguide. b) Transmission for a wavelength sweep around the resonance.

range (FSR) and is given by [147]

$$\mathrm{FSR}_\lambda = \Delta\lambda = \frac{1}{R}\left(\frac{\partial\beta}{\partial\lambda}\right)^{-1} = \frac{\lambda^2}{2\pi R\, n_\mathrm{g}} \approx \frac{\lambda^2}{2\pi R\, n_\mathrm{eff}}\,, \tag{6.4a}$$

$$\mathrm{FSR}_\omega = \frac{\omega}{\lambda} \times \mathrm{FSR}_\lambda\,, \tag{6.4b}$$

where n_g is the group refractive index which accounts for the wavelength dependence of the effective index, see section 2.1. The time required to accomplish one round-trip is then given by $t_\mathrm{R} = 2\pi/\mathrm{FSR}_\omega$.

Another important quantity is obtained by the ratio of the FSR and the resonance width $\delta\lambda$ (FWHM) and is called Finesse $\mathcal{F} = \mathrm{FSR}_\lambda/\delta\lambda = \mathrm{FSR}_\omega/\delta\omega$. It can be interpreted as the number of round trips a photon undergoes in the ring until its probability amplitude has dropped to $1/e$. A related parameter to the finesse is the quality factor Q and is defined as

$$Q = \frac{\lambda}{\delta\lambda} = \frac{\omega}{\delta\omega} \approx \frac{2\pi R n_\mathrm{eff}}{\lambda}\mathcal{F}\,. \tag{6.5}$$

It is a measure for the decay time of the stored energy times the frequency. Finally, we define the extinction ratio ER which quantifies the depth of a resonance feature and is given by

$$\mathrm{ER} = 10 \log_{10} \left(\frac{T_{\max}}{T_{\min}} \right) , \tag{6.6}$$

where $T_{\max}$ and $T_{\min}$ are the maximum and minimum transmission, respectively.

6.1.1 Ring resonator coupled to atomic vapor

We now want to derive the transmission behavior of the bus waveguide if the ring resonator is surrounded by rubidium vapor. To restrict the atom-light interaction mainly to the ring, the remaining parts are covered with HSQ except for the short coupling region between the bus waveguide and the ring denoted by L_{bus} (see Figure 6.1). The phase acquired during a round trip in the ring is now influenced by the refractive index of the atoms and can be expressed in terms of the altered propagation constant (see section 4.1):

$$\phi = L \, \mathrm{Re}(\beta_{\mathrm{Rb}}) , \tag{6.7}$$

where $L = 2\pi R$ is the circumference of the ring. Furthermore, the round trip transmission factor is changed due to resonant absorption losses by the atoms:

$$\tau^* = \tau e^{-\,\mathrm{Im}(\beta_{\mathrm{Rb}})L} . \tag{6.8}$$

Using eq. (6.3), the bus waveguide transmission in presence of the atoms is then given by

$$\begin{aligned} T_{\mathrm{bus}} = {} & e^{-2\,\mathrm{Im}(\beta_{\mathrm{Rb}})L_{\mathrm{bus}}} \\ & \times \frac{\tau^2 e^{-2\,\mathrm{Im}(\beta_{\mathrm{Rb}})L} - 2r\tau e^{-\,\mathrm{Im}(\beta_{\mathrm{Rb}})L} \cos\left[\mathrm{Re}(\beta_{\mathrm{Rb}})L + \varphi_0\right] + r^2}{1 - 2r\tau e^{-\,\mathrm{Im}(\beta_{\mathrm{Rb}})L} \cos\left[\mathrm{Re}(\beta_{\mathrm{Rb}})L + \varphi_0\right] + r^2\tau^2 e^{-2\,\mathrm{Im}(\beta_{\mathrm{Rb}})L}} , \end{aligned} \tag{6.9}$$

where ϕ_0 is a phase offset. The prefactor in eq. (6.9) accounts for the absorption along the uncovered region of the bus waveguide.

6.2 Ring resonator characterization

Here we present a characterization of the ring resonator type used for the experiments in this work and evaluate the performance of these devices. First, in section 6.2.1 the behavior is analyzed without the presence of rubidium. In section 6.2.2 we then discuss the effects of rubidium on the general (non-resonant) transmission properties.

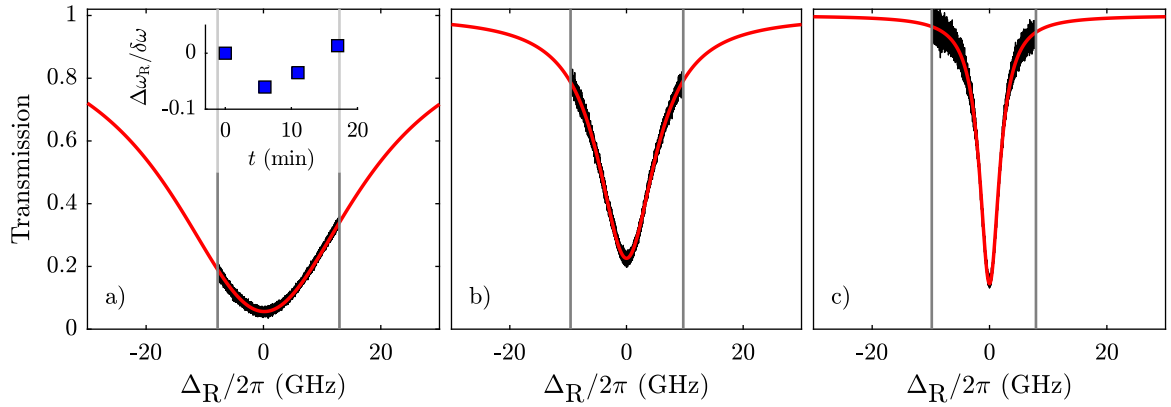

Figure 6.3: Bus waveguide transmission for ring resonators with different gap size g on the NGJ21 chip (see Appendix D.2). The curves have been recorded in absence of rubidium. Vertical gray lines indicate the scan range of the laser. The red lines show a Lorentzian fit with extrapolation to larger detunings. a) $g = 75\,\text{nm}$. b) $g = 100\,\text{nm}$. c) $g = 200\,\text{nm}$. The inset in a) shows the change of the center frequency position of the ring resonance over time: $\Delta\omega = \omega_R(t) - \omega_R(t = 0)$.

6.2.1 Without rubidium

The discussion in this section refers to the ring resonators on the NGJ21 chip[1] before filling the cell with rubidium. The rings have a radius of $R = 80\,\mu\text{m}$, corresponding to a free spectral range of $\text{FSR}_\omega/2\pi \approx 308\,\text{GHz}$ around $\lambda = 780\,\text{nm}$.

Figure 6.3 shows the bus waveguide transmission for different devices with increasing gap size ($g = 75\,\text{nm} - 200\,\text{nm}$) versus laser detuning from the ring resonance $\Delta_R = \omega_p - \omega_R$, where ω_p is the frequency of the probe laser. As the coupling decreases with growing gap size, the photon lifetime in the ring increases and therefore the resonance line width reduces. An overview of the relevant parameters is presented in table 6.1. The line width $\delta\omega$ was obtained from a Lorentzian fit to the transmission curves and has been used to calculate $\mathcal{F}$ and Q.

The device with a gap size of $g = 75\,\text{nm}$ exhibits an extinction ratio of $\text{ER} \approx 12\,\text{dB}$ and is therefore close to critical coupling (Figure 6.3 a)). With increasing g, a decrease in ER is expected as confirmed in b). However, the larger ER in c) suggests that the propagation losses vary between different devices, perhaps due to fabrication tolerances.

The ring resonance frequency ω_R can be tuned by varying the temperature of the chip due to the refractive index change of the involved materials and, to a lesser extent,

[1]The NGJ21 chip did not have an Al_2O_3 protective coating, see Appendix D.2.

g (nm)	$\delta\omega/2\pi$ (GHz)	$\mathcal{F}$	Q
75	39.1	7.9	9.8×10^3
100	11.8	26.1	3.3×10^4
200	4.1	75.3	9.4×10^4

Table 6.1: Measured ring resonator parameters for devices with different gap size g on the NGJ21 chip in absence of rubidium.

thermal expansion of the ring[2]. The relatively large radius of our rings allows us to tune between individual resonances with moderate temperature changes. For an Si_3N_4 ring with $R = 80\,\mu m$ the thermal tuning rate of the resonance frequency was found to be $\partial\omega_R/\partial T \approx 2\pi \times 5\,\mathrm{GHz\,K^{-1}}$. Consequently, a reasonable temperature control is required in order to keep the resonance at a fixed position. The inset of Figure 6.3 a) shows the variation of ω_R over time for a fixed oven temperature set point and indicates a temperature stability of $\Delta T < \pm 0.15\,\mathrm{K}$, which is within the expected performance of the used temperature controller.

6.2.2 With rubidium

If the ring resonators are exposed to rubidium their performance changes drastically. Due to additional propagation losses caused by alkali atoms interacting with the waveguide surface (see section 4.5) the round trip transmission coefficient τ for the devices on the NGJ21 chip dropped so low that the resonances entirely disappeared. Consequently, the subsequent chip generations have been protected by a 9 nm thick Al_2O_3 coating grown by atomic layer deposition.

Figure 6.4 shows the consecutive resonances of an Al_2O_3 coated ring ($R = 80\,\mu m$, $g = 200\,nm$) appearing at certain temperatures during the initial heating of the chip[3] after filling the cell with Rb. The reservoir was not actively heated during this measurement series, however thermal coupling caused the reservoir temperature to be in the range of 50 °C to 74 °C which leads to a substantial Rb vapor pressure once thermodynamic equilibrium is achieved. While the line width of the first two resonances remained narrow with $\delta\omega = 8.6\,\mathrm{GHz}$, the resonance at 217 °C was broadened to $\delta\omega = 16.6\,\mathrm{GHz}$ due to the build up of Rb vapor pressure in the cell, which depends not only on the reservoir temperature but also takes a certain "curing time" (see section 4.5). Although the propagation losses and therefore the line width increased with the addition of

[2] For Si_3N_4 the thermo-optic coefficient at 300 K and $\lambda = 850\,nm$ is $dn/dT \approx 2.5 \times 10^{-5}\,\mathrm{K^{-1}}$ [148], whereas the thermal expansion coefficient is $\alpha_{th} \approx 7.6 \times 10^{-7}\,\mathrm{K^{-1}}$ [149].

[3] NGJ30-II, see Appendix D.3.

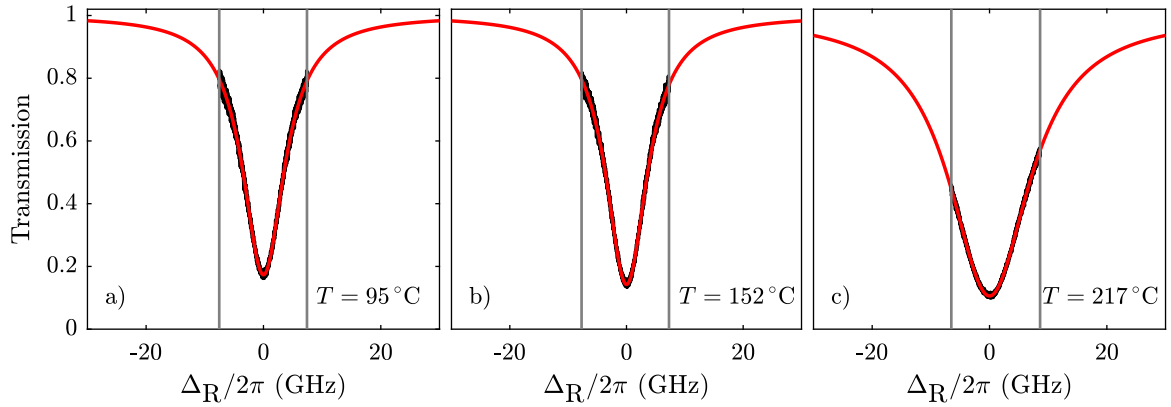

Figure 6.4: Ring resonances of one and the same device appearing at different temperatures during the initial heat up of a rubidium filled cell with Al_2O_3 coating. The broadening of the resonance in c) is attributed to alkali induced losses since the rubidium pressure inside the cell started to build up in the meantime.

rubidium, it is crucial that the resonance remains visible owing to the Al_2O_3 coating.

Most of the ring resonator experiments involving rubidium were performed with a device which had a gap of $g = 100\,\mathrm{nm}$ in order to approach critical coupling of the resonator. In this case a line width of $\delta\omega = 50\,\mathrm{GHz}$ has been measured a few days after filling the cell. Although the line width is increased by factor of five compared to a similar device with the same parameters but without rubidium, the line width remained nearly constant for two months, even at elevated rubidium density. Thus, applying a thin ALD grown Al_2O_3 layer on the nanophotonic chip seems to be an effective method to reduce alkali induced losses.

6.3 Coupling thermal Rb vapor to a ring resonator

The experiments in this section employ a ring resonator on the Al_2O_3 coated NGJ30-II chip with radius $R = 80\,\mu\mathrm{m}$ and a distance $g = 100\,\mathrm{nm}$ to the bus waveguide. This device is close to critical coupling such that near zero transmission on resonance is achieved.

The inset of Figure 6.5 shows a typical transmission spectrum of the bus waveguide at a moderate atom density ($\mathcal{N} \approx 2 \times 10^{13}\,\mathrm{cm}^{-3}$), where the ring resonance is centered to the atomic resonance ω_0 and the probe frequency ω_p is scanned over the rubidium D_2 line with the detuning $\Delta_\mathrm{p} = \omega_\mathrm{p} - \omega_0$. The transmission of the device without contribution of the atoms is calculated from fit parameters of the numerical model

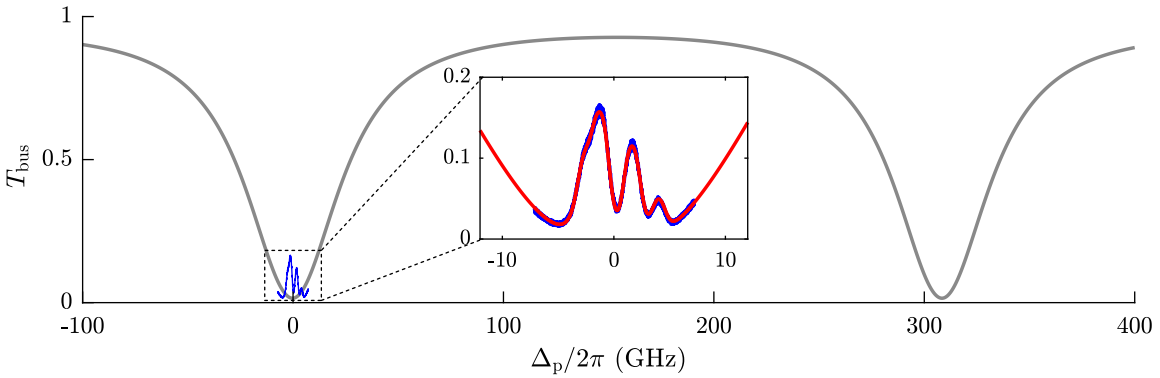

Figure 6.5: Coupling an integrated ring resonator to atomic vapor. The gray curve shows the calculated bus waveguide transmission without contribution of the atoms. The transmission is modified in presence of the atoms (blue curve), which is shown more detailed with a fit of the model (red curve) in the inset.

described in section 6.1.1 and displayed in the background of Figure 6.5 over more than one free spectral range (FSR$/2\pi \approx 308\,$GHz) to visualize the bandwidth proportions.

Both absorptive and dispersive properties of the atoms play a role, when they interact with the resonator mode. The absorption of the light field lifts the critical coupling condition, leading to an increase in transmission within the ring resonance feature for $\omega_{\mathrm{R}} \approx \omega_0$, whereas the real part alters the round trip phase shift, leading to a shift of the ring resonance to lower (higher) frequencies on the red (blue) side of the atomic resonance. We observe a red shift of $\sim -2\pi \times 60\,$MHz of the atomic resonance with respect to a reference vapor cell which we attribute to Casimir–Polder interactions with the waveguide surface. The size of this shift is comparable to the shifts we measured with other types of devices during the course of this work and is reproduced by Monte Carlo simulations (see, e.g., section 4.4 or 7.2).

Note that the total signal is always a combination of the ring signal and the absorption signal from the 100 µm long uncovered part of the bus waveguide. The interaction of the atoms with the ring does not only manifest itself in the transmission signal, but is also directly visible in the fluorescence of the atoms as shown in Figure 6.6(a) and (b) for an off-resonant and a resonant situation, respectively. In b) the attenuation of the guided mode in the ring is clearly observable, which is not only caused by the absorption of resonant atoms but also by non-resonant losses due to adsorbed atoms on the waveguide surface.

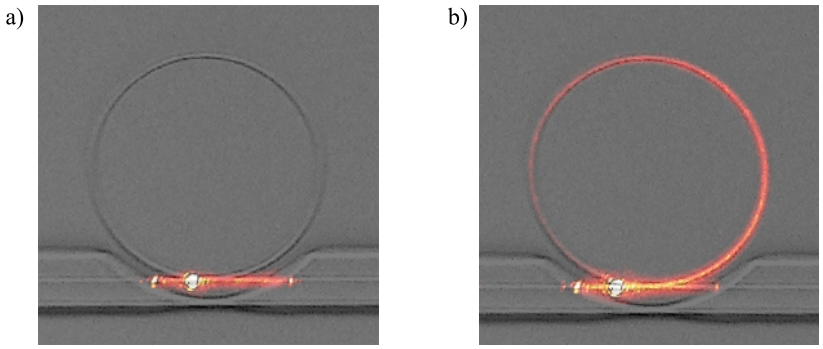

Figure 6.6: Photographs of the ring for an off-resonant situation a) and for $\omega_R \approx \omega_0$ b).The interaction of the evanescent field with the rubidium vapor is directly visible due to the fluorescence light of the atoms, which is color coded in these pictures.

6.3.1 Ring resonance frequency scan

In order to investigate the transmission behavior at different positions within the ring resonance, we performed a series of measurements where we thermally tune the ring resonance frequency to several values of the atom-resonator detuning $\Delta_{\mathrm{AR}} = \omega_0 - \omega_{\mathrm{R}}$, while scanning the probe laser over the rubidium D_2 line. Figure 6.7 presents the results of these measurements for an atom density of $\mathcal{N} \approx 10^{14}\,\mathrm{cm}^{-3}$.

In Figure 6.7 a) the bus waveguide transmission spectra are placed at the corresponding positions of the ring resonance feature, as determined from fits to the data. Figure 6.7 b)-d) show selected transmission data for three values of Δ_{AR} together with their respective fitting curves. In the off-resonant case shown in Figure 6.7 b) the transmission spectrum is dominated by absorption in the uncovered part of the bus waveguide, since there is almost no coupling of the probe light into the ring, which is also clearly visible in Figure 6.6 a). At the slope of the resonance (see Figure 6.7 c)), the signal reveals the dispersive nature of the atoms, since a small change in the real part of the atomic susceptibility involves a shift of the ring resonance and therefore leads to a large modulation of the bus waveguide transmission. Finally, on resonance ($\omega_{\mathrm{R}} \approx \omega_0$) the additional losses induced by the atomic absorption lead to increased transmission since destructive interference of the field in the bus waveguide and the field returning from the ring is diminished. This situation is shown in Figure 6.7 d), where the transmission enhancement amounts approximately 40%.

6.3.2 Saturation measurements

In this section we study the saturation behavior of the atoms in the evanescent field of the ring mode. On resonance, the intensity in the ring can be much larger than the

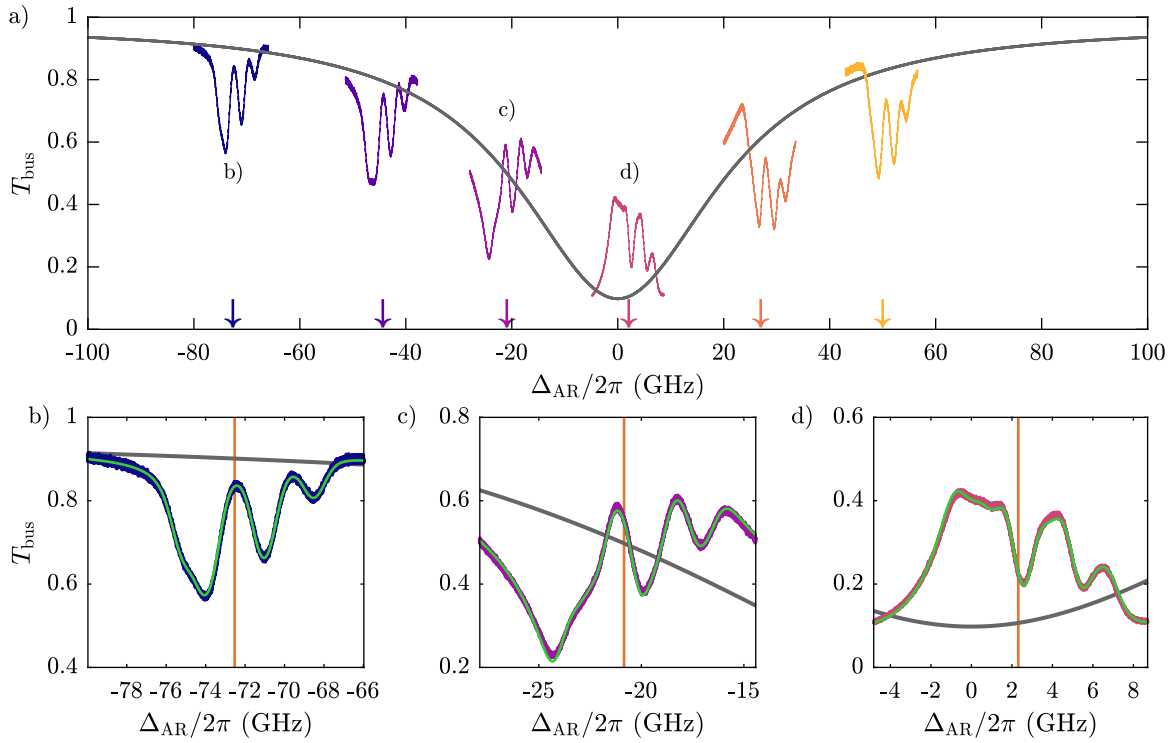

Figure 6.7: Transmission measurements for various atom-resonator detunings Δ_{AR}. a) The gray curve shows the bus waveguide transmission without atomic contribution, as calculated from fit parameters. The superimposed spectra show the transmission for an atomic density of $\mathcal{N} \approx 10^{14}\,\mathrm{cm}^{-3}$ at corresponding Δ_{AR}. b)-d) Individual transmission spectra for an off-resonant ring b), on the slope of the resonance c) and close to resonance $\omega_{\mathrm{R}} \approx \omega_0$ d) with fits of the model (green curves). The vertical lines indicate the positions of the center of mass frequency of the rubidium D_2 line, ω_0.

intensity in the bus waveguide due to constructive interference of the circulating field with the input field. Hence, saturation of the atoms around the ring is expected to happen at lower input powers compared to a regular straight waveguide. The intensity enhancement B can be calculated from equations (6.1) and (6.2) as

$$B = \left|\frac{\mathcal{E}_3}{\mathcal{E}_1}\right|^2 = \frac{\tau^2(1-r^2)}{(1-\tau r)^2}\,. \tag{6.10}$$

If the resonator is lossless and very weakly coupled to the bus waveguide the intensity enhancement is directly linked to the finesse and is given by $B = \mathcal{F}/\pi$ [147].

As the losses of the resonator investigated in this work are rather high we obtain $B = 1.06$, with $r \approx 0.85, \tau \approx 0.74$ as inferred from theory fits, thus there is no considerable intensity buildup in the ring. Nevertheless it is worth studying the saturation with the device at hand since we can derive a few interesting quantities from this measurement

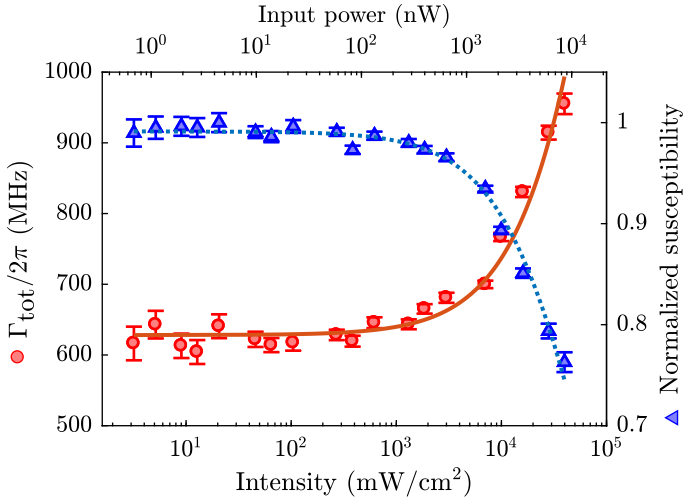

Figure 6.8: Saturation behavior in the ring resonator. Red dots show the Lorentz width versus input probe power (top axis) extracted from fits to the transmission data. Error bars show 95% confidence intervals for the determined widths. The red curve is a fit of $\Gamma_{\mathrm{tot}} = \Gamma(1+P_{\mathrm{in}}/P_{\mathrm{sat}})^{1/2}$ with initial line width $\Gamma/2\pi = 628\,\mathrm{MHz}$ and saturation power $P_{\mathrm{sat}} \approx 5.7\,\mu\mathrm{W}$. From P_{sat} we estimate the corresponding mean intensity of the evanescent field (bottom axis). Blue triangles show the normalized susceptibility. The blue dotted curve is a guide to the eye.

such as the mean photon number inside the ring. Therefore, a sequence of transmission spectra was recorded for different input powers with the ring resonance tuned to the atomic resonance. By fitting these spectra the power dependent Lorentzian line width and the magnitude of the susceptibility of the atoms are extracted and presented in Figure 6.8. The line width clearly exceeds the natural line width of rubidium already at low powers, which is mostly attributed to transit time broadening. In order to determine the input power, at which saturation occurs, we fit the function $\Gamma_{\mathrm{tot}} = \Gamma(1 + P_{\mathrm{in}}/P_{\mathrm{sat}})^{1/2}$ to the data, with initial line width $\Gamma/2\pi = 628\,\mathrm{MHz}$ and saturation power $P_{\mathrm{sat}} \approx 5.7\,\mu\mathrm{W}$.

The knowledge of P_{sat} allows us to estimate a mean intensity of the evanescent field for a given input power, by assuming $I = P_{\mathrm{in}} \times I_{\mathrm{sat}}/P_{\mathrm{sat}}$, where I_{sat} is the saturation intensity of the rubidium D_2 line, assuming a line width of Γ. By simulating the intensity distribution[4] for our waveguide geometry we infer that I_{sat} is reached for an atom located at the position of maximum external electric field strength with a mode power of $P_{\mathrm{m}} \approx 100\,\mathrm{nW}$, which corresponds to a mean photon number of $\langle n \rangle = P_{\mathrm{m}}/(\hbar\omega \times \mathrm{FSR}_\omega) \approx 1.3$ photons being in the ring.

[4]The local intensity is calculated using (2.5) of section 2.1.

6.4 Cavity QED considerations

Achieving strong coupling between light and matter in a regime where individual quanta are involved is of highest interest for both fundamental research and technology. A promising approach is to couple an atom to a resonator mode which is the basic principle of cavity quantum electrodynamics (cavity QED) [55–57]. To implement a whole network where many nodes are linked by single photons, nanophotonic resonators are favored candidates because they can be scalably fabricated and interconnected with waveguides and fibers [58]. Here we analyze the potential performance of our ring resonators in this context and estimate to what extend strong coupling could be achieved between thermal atoms and modes of integrated resonators in general.

6.4.1 Cavity QED concepts

The probability that a photon interacts with an atom is enhanced by placing the atom inside a cavity since the circulating photon passes the atom multiple times. The performance of a cavity QED system therefore depends on the photon lifetime τ inside the cavity which is related to the cavity line width by $\tau = 1/\delta\omega = Q/\omega = 1/(2\kappa)$, where κ is the total cavity field decay rate [150]. Note that κ is composed of an intrinsic decay rate κ_{int} due to absorption or propagation losses and an extrinsic decay rate κ_{ext} which accounts for the coupling between the cavity and the input or output ports.

The atom-photon interaction strength further depends on the energy density of a photon within the mode volume V_{m} of the cavity which is defined as [150]

$$V_{\mathrm{m}} = \frac{\iiint_{V_{\mathrm{Q}}} \epsilon(\boldsymbol{r}) \left|\boldsymbol{\mathcal{E}}(\boldsymbol{r})\right|^2 \mathrm{d}^3\boldsymbol{r}}{\left|\boldsymbol{\mathcal{E}}_{\mathrm{max}}\right|^2}\,, \tag{6.11}$$

where ϵ is the material dielectric constant and the integration is performed over a volume V_{Q} [5]. The mode volume determines the spatial confinement of the photon. Hence, the smaller the mode volume the larger the interaction strength. The coupling between an atom at position $\boldsymbol{r}$ and the cavity mode is described by the coupling rate $g(\boldsymbol{r})$, with [55]

$$g(\boldsymbol{r}) = \boldsymbol{d}\left|\frac{\boldsymbol{\mathcal{E}}(\boldsymbol{r})}{\boldsymbol{\mathcal{E}}_{\mathrm{max}}}\right|\sqrt{\frac{\omega_0}{2\hbar\epsilon_0 V_{\mathrm{m}}}}\,, \tag{6.12}$$

where $\boldsymbol{d}$ is the dipole moment of the atomic transition and $|\boldsymbol{\mathcal{E}}(\boldsymbol{r})/\boldsymbol{\mathcal{E}}_{\mathrm{max}}|$ is the normalized electric field strength at the atom's position. The parameter g describes the coherent, reversible exchange of excitation between an atom and a single mode and is related to the single photon Rabi frequency $\Omega = 2g$ [150].

[5] The cross section of the integration volume for our calculations was chosen to be a rectangular region with several µm side length such that the electric field of the mode is practically zero at the boundaries.

In order to achieve a controlled (coherent) coupling, the rate g has to be larger than all involved dissipation rates in the system. This defines the strong coupling regime with the requirement $g > [\Gamma_\perp, \kappa, T^{-1}]$, where $\Gamma_\perp$ is the atomic dephasing rate and T is the interaction time between the atom and the cavity field (e.g. transit time). In cavity QED, the coupling strength relative to the geometric mean of the damping rates is described in a dimensionless (single-atom) cooperativity parameter C which is usually defined as [151]

$$C = \frac{g^2}{2\kappa\Gamma_\perp}\,. \tag{6.13}$$

If $C > 1$, the atom-cavity coupling is considered to be strong. Note that the standard definition eq. (6.13) of the cooperativity does not account for a limited transit time which should in case of moving atoms be incorporated into $\Gamma_\perp$. Also, the condition for strong coupling, $C > 1$, is less stringent than $g > [\Gamma_\perp, \kappa, T^{-1}]$ since C can be large although the coupling rate is much smaller than one of the damping rates.

Two more parameters are in general used to characterize a cavity QED system [150]:

$$n_0 = \frac{\Gamma_\perp^2}{2g^2}\,, \qquad N_0 = \frac{2\Gamma_\perp\kappa}{g^2} = \frac{1}{C}\,, \tag{6.14}$$

where n_0 is the the critical photon number, which is the number of photons required to saturate an atom in the cavity field, and N_0 is the critical atom number, which is the number of atoms required to observe critical effects in the cavity transmission, such as the splitting of cavity resonances, known as vacuum Rabi splitting [152]. Note, that this splitting is not an inherently quantum phenomenon but can already be described by a classical theory based on linear atomic absorption and dispersion [153].

6.4.2 Evaluation of ring resonators

We now want to make a rough estimation of the performance of the atom-resonator system presented in section 6.3 with regard to the concepts of cavity QED. To determine the coupling rate g, the mode volume was calculated using COMSOL and eq. (6.11) to be $V_\mathrm{m} = 143\,\mu\mathrm{m}^3$. The resulting position dependent coupling rate for the Rb D_2 transition is shown in Figure 6.9 a). Close to the waveguide surface a maximum coupling rate of $g_\mathrm{max}/2\pi = 193\,\mathrm{MHz}$ is obtained, but also a huge surface-induced line shift. At a distance of 20 nm the Casimir–Polder shift is on the order of $\Delta_\mathrm{CP}/2\pi \approx 1\,\mathrm{GHz}$ and comparable to the linewidth Γ of the measured transmission spectra. In this case, the coupling rate is $g/2\pi \geq 85\,\mathrm{MHz}$ across the total width of the waveguide (see Figure 6.9 b)).

Due to the large cavity field decay rate and atomic linewidth this first realization of a thermal atom-cavity system on a chip is far from being in the strong coupling regime ($g \ll \kappa, \Gamma$). This is also reflected in the low single-atom cooperativity on the

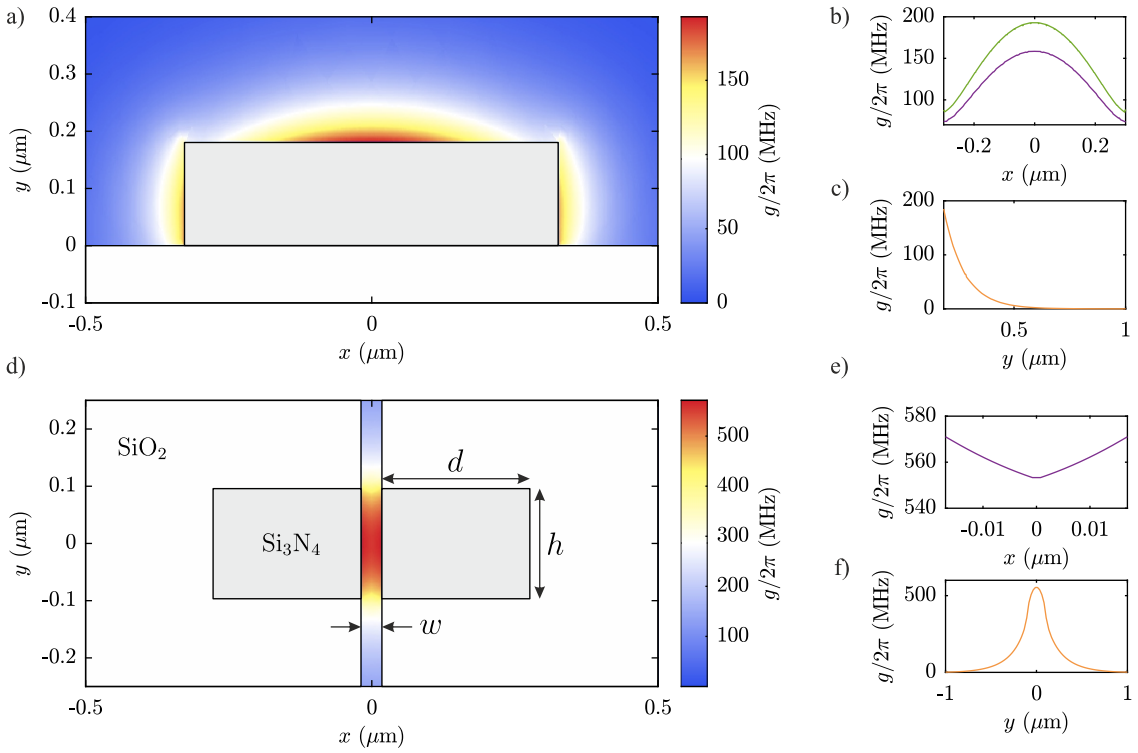

Figure 6.9: Coupling rate g for an atom near a ring resonator. a) Cross-section of the experimentally investigated ridge waveguide ring resonator showing the coupling rate $g(x, y)$. b) Coupling rate along the waveguide surface (green line) and in 20 nm distance above the waveguide, where $\Delta_{\mathrm{CP}} \approx \Gamma$. c) Coupling rate as a function of distance from the waveguide surface for $x = 0$ and $y > h$. d) Cross-section of a slot ring resonator embedded in SiO_2. e) Coupling rate across the center of the slot ($y = 0$) and f) along the vertical center ($x = 0$).

order of $C \approx 10^{-3}$, and a correspondingly large critical atom number $N_0 = 1/C \approx 1000$. To estimate the mean number of atoms interacting with the resonator under the experimental conditions of section 6.3.1, we assume the atom density in the evanescent field to be identical with the Rb density $\mathcal{N} \approx 1 \times 10^{14}\,\mathrm{cm}^{-3}$ inside the cell volume. An external mode volume outside the ring waveguide of $V_{\mathrm{m}}^{\mathrm{e}} = 5.6 \times 10^{-18}\,\mathrm{m}^3$ suggest that $\overline{N} \approx 1250$ atoms are within the resonator mode, which is similar to the critical atom number N_0. Hence, the *collective* cooperativity is on the order $\overline{N}C \sim 1$, provided that every atom interacts with the mode. However, a distinct splitting of the ring resonance in Figure 6.7 is spoiled by averaging over coupling rates $g(\boldsymbol{r}) \leq g_{\mathrm{max}}$, the contributions of multiple transitions and the superimposed absorption signal from the bus waveguide.

For the critical photon number we obtain $n_0 \approx 1.3$ assuming the maximum coupling rate g_{max} which is in agreement with the average photon number $\langle n \rangle \approx 1.3$ derived

from the saturation measurement in section 6.3.2, likewise for the position of maximum electric field strength.

Although ring resonators are not ideal candidates to enter the strong coupling regime, creating the ring from a slot waveguide (see section 7) instead of a ridge (solid core) waveguide can increase the coupling rate significantly. Figures 6.9 d)-e) show the coupling rate for a TE slot mode of a Si_3N_4 ring resonator with $R = 80\,\mu m$, which is the same radius as for the investigated ridge waveguide ring above. Here, the slot width $w = 35\,nm$, core width $d = 260\,nm$ and core height $h = 190\,nm$ are chosen, as these parameters result in an optimal field confinement inside the slot. Furthermore, the domains outside the slot are masked with a thick SiO_2 layer to restrict atom-light interaction mainly to the slot region.

The strong mode confinement in the slot region leads to a reduction of the mode volume compared to the ridge waveguide ring resonator with the same radius, which results in a coupling rate of $g/2\pi > 500\,MHz$. A smaller ring radius of $R = 20\,\mu m$ would roughly double the coupling rate to $g/2\pi \approx 1\,GHz$ and therefore become comparable to the atomic linewidth, though a larger transit time broadening is expected in the narrow slot. For κ to be on the same order, a quality factor of $Q \approx 2 \times 10^5$ would be required at $\lambda = 780\,nm$. An intrinsic Q of 3×10^6 has been measured for a $20\,\mu m$ Si_3N_4 ring resonator at $\lambda = 1540\,nm$ [154], however, alkali induced losses are currently limiting the quality factor in our system. If this obstacle could be overcome by, e.g., using a different waveguide material or optimizing the protection coating, it might be possible to reach the strong coupling regime with slot ring resonators and single atoms at room temperature.

6.4.3 Towards strong coupling

Coherent coupling between a thermal atom and a cavity mode is mainly limited by the short interaction time T due to the motion of the atom and the small mode volume required to achieve an appreciable coupling rate. This implies that the bandwidth for photons to enter and leave the cavity has to be large compared to the inverse interaction time in order to utilize the interaction mechanism for any processing. Also, there is no benefit to be gained from a photon circulating in the cavity while the atom is already gone. Therefore, we can specify an upper limit for a useful quality factor $Q \leq \omega T/2\pi$, determined by the exchange rate κ_{ext} and assuming $\kappa_{int} \to 0$. For a light field at $\lambda = 780\,nm$ and an interaction time of $1\,ns$ we obtain $Q \leq 3.8 \times 10^5$. Consequently, the condition for strong coupling with moving atoms is $g \gg \kappa > \Gamma$, where Γ incorporates all atomic decoherence effects. For the coupling strength to be large, the cavity mode volume has to be as small as possible and the electric field at the position of the atom as large as possible. These requirements are met by photonic crystal (PC) microcavities where the atom could interact with the field in the air hole of the PC [155].

To estimate achievable cavity QED numbers, we consider the Si_3N_4 nanobeam PC presented in [156] with a mode volume of $V_m = 0.55(\lambda/n)^3$ and measured quality factor $Q \approx 5.5 \times 10^4$ at $\lambda = 624\,\mathrm{nm}$ (theoretical $Q = 2.3 \times 10^5$) which translates to a cavity loss rate $\kappa/2\pi = 4.4\,\mathrm{GHz}$ (theoretical $\kappa/2\pi = 1\,\mathrm{GHz}$). The nanobeam has a thickness of 200 nm and the radius of the central lattice hole is 50 nm. A rubidium atom at 100 °C with mean velocity $330\,\mathrm{m\,s^{-1}}$ transits the cavity hole vertically (radially) in 606 ps (150 ps), corresponding to an atom loss rate of $\Gamma/2\pi = 1.6\,\mathrm{GHz}$ ($\Gamma/2\pi = 6.6\,\mathrm{GHz}$). The extremely small mode volume of the PC results in a maximum coupling rate of $g_{\max}/2\pi = 5.7\,\mathrm{GHz}$ for the Rb D_2 transition.

Although $g_{\max}$ slightly exceeds κ and for nearly vertically transiting atoms also Γ, the presented example is on the border of being in the strong coupling regime. An even higher interaction strength would require a further reduction of the mode volume which in turn shortens the transit time. The influence of surface induced level shifts is not considered in this estimation and constitutes a further critical issue when coupling atoms to a nanophotonic resonator. However, a demonstration of strong coupling of atoms transiting the PC hole at moderate velocities and favorable trajectories should be possible in such a system when using real-time detection as presented in [62, 157]. To establish the feasibility of quantum information processing with thermal atoms and on-chip cavities, a more thorough analysis is required which is beyond the scope of this thesis.

7 Spectroscopy with slot waveguides

In this chapter we study the interaction of thermal rubidium atoms with the guided mode of slot waveguides. A slot waveguide consist of two parallel ridge waveguides which are separated by a distance smaller than the decay length of the evanescent field. These devices provide strong confinement of the light field in the slot between the two individual waveguides, which is accessible by the atomic vapor. The region of high optical intensity inside the slot enables enhanced atom-light coupling as compared to, e.g., nanofibers [158–160] or solid core waveguides [41, 44, 140], where the atoms interact only with the tail of the evanescent field while the major part of the mode resides in the core material.

We investigate the transmission of these waveguides depending on the slot width, which determines the fraction of transmitted light power interacting with the atomic vapor. For narrow slot widths, the mode is strongly confined inside the slot with high electric field amplitude at the position of the atoms, while for increasing slot widths, the mode is more and more confined to the individual cores. One would therefore expect to observe decreasing atom-light coupling for growing slot widths. Due to limitations in the fabrication process of the optical chip, the investigated structures exhibit a gradual transition from a single ridge waveguide to fully opened slot waveguides. To comprehend the complex atom-light interaction around the imperfect structures, we compare the measured line shapes to Monte Carlo simulations including the specific waveguide geometries and associated atom-surface interactions.

Furthermore, we examine density dependent effects on the line widths and line shifts of the rubidium atoms in the sub-wavelength interaction region of a slot waveguide. Optical waveguides, and in particular slot waveguides, offer the possibility to study resonant dipole-dipole interactions in a quasi-one-dimensional system. Initial experimental investigations in this direction are presented at the end of this chapter.

7.1 Slot waveguide basics

A slot waveguide is a comparatively novel light guiding structure which was first proposed in 2004 [69] and subsequently demonstrated in an experiment [161]. The slot waveguide consist of two high-index material strips of width d and height h separated by a low-index gap of size w, see Figure. 7.1 a). At the interface between high- and

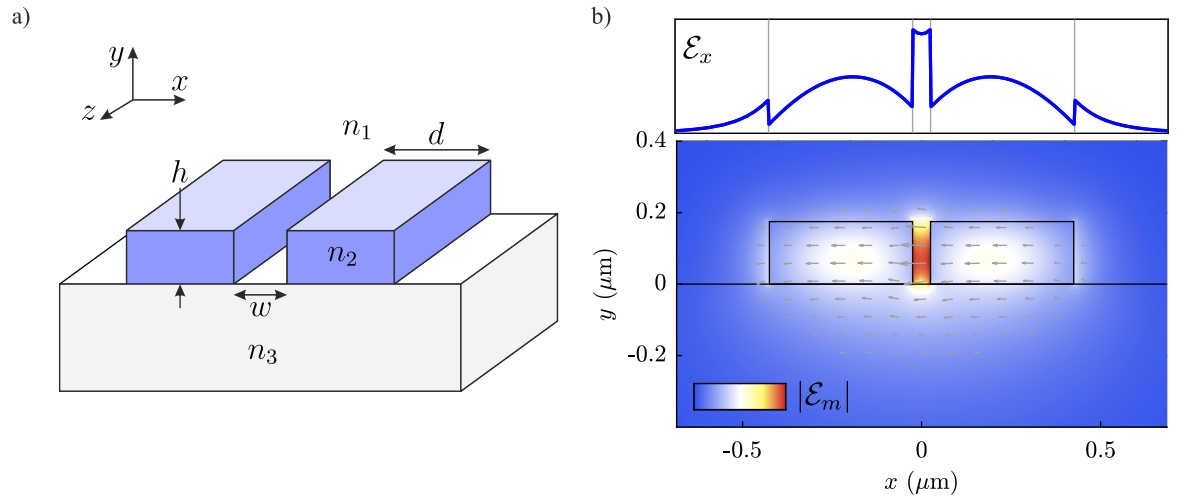

Figure 7.1: Slot waveguide structure and mode profile. a) Geometry of a slot waveguide. The two waveguide cores of refractive index n_2 are placed on a substrate of index n_3 and surrounded by a cladding of index n_1. b) Simulated electric field profile $|\boldsymbol{\mathcal{E}}_m(x,y)|$ of the fundamental mode for a $w = 50\,\mathrm{nm}$ Si_3N_4 waveguide ($h = 180\,\mathrm{nm}$, $d = 400\,\mathrm{nm}$) on an SiO_2 substrate. The gray arrows indicate the direction and strength of the electric field, representing the polarization direction. The top panel shows a horizontal cut of the transverse electric field component $\mathcal{E}_x$ through the center of the structure.

low-index regions the electric displacement field[1] has to satisfy the boundary condition [162]

$$(\boldsymbol{D}_2 - \boldsymbol{D}_1) \cdot \boldsymbol{n}_{21} = 0\,, \tag{7.1}$$

where $\boldsymbol{n}_{21}$ is a unit vector normal to the interface. Thus, the boundary condition for the normal component of the electric field reads

$$\epsilon_2 E_2^{\perp} = \epsilon_1 E_1^{\perp}\,, \tag{7.2a}$$
$$n_2^2 E_2^{\perp} = n_1^2 E_1^{\perp}\,. \tag{7.2b}$$

Consequently, the electric field of a TE-like mode undergoes a discontinuity at the sidewall interface of the waveguide. Right at the interface the electric field inside the slot is enhanced by n_2^2/n_1^2 compared to the electric field at the boundary inside the waveguide core. For a Si_3N_4 waveguide core and a vacuum cladding we get $n_2^2/n_1^2 \approx 4$. If the separation of the two strips is smaller than the evanescent decay length of the individual strip modes, a high electric field amplitude is maintained across the slot, as can be seen in Figure 7.1 b). This electric field enhancement makes slot waveguides particularly attractive for applications in nonlinear optics and as an interface for light and quantum emitters [163].

[1] In absence of free surface charge.

7.2 Slot width dependent measurements

The most fascinating feature of a slot waveguide is the sub wavelength confinement of the light field in the low index region which offers enhanced coupling between atoms and photons. To study the behavior of thermal atoms coupled to a slot waveguide mode we performed various spectroscopic measurements as a function of the slot width which determines the fraction of optical power at the positions of the atoms.

7.2.1 Waveguide design and description of the experiment

The slot waveguides consist of two Si_3N_4 strips with height and width designed to be $h = 175\,\text{nm}$ and $d = 400\,\text{nm}$, respectively. The height has been confirmed by measuring the Si_3N_4 layer thickness using refractometry. The strips are separated by a gap of width w, which is varied for the different devices, see Figure 7.2. The slot waveguide section is on both ends transformed into 650 nm wide ridge waveguides via Y junctions which are connected to grating couplers. Both couplers and the Y junctions are covered with an 800 nm thick layer of HSQ (SiO_2) in order to restrict the atom-light interaction only to the slot waveguide region. The uncovered domains which are accessible for the atoms have a length of $l = 200\,\mu\text{m}$. To protect the structures from Rb atoms sticking to the waveguide surface and potential chemical reactions, the devices are additionally covered with a 7 nm thick Al_2O_3 coating via atomic layer deposition.

The chip[2] used for the presented measurements contains several slot waveguides designed to have slot widths in the range $w_\text{d} = 30\,\text{nm} - 250\,\text{nm}$. After the experiments have been conducted, the chip was removed from the cell and a focused ion beam (FIB) was used to cut a trench into the structures to expose their cross-sections which have subsequently been examined by scanning electron microscopy (SEM). Samples of the images obtained with this method are shown in Figure 7.2 c) for the $w_\text{d} = 40\,\text{nm}$ (i), $w_\text{d} = 75\,\text{nm}$ (ii) and $w_\text{d} = 125\,\text{nm}$ (iii) slot waveguides. The bright rough layer covering the surface of the sample in this micrograph is a sputtered gold layer which forms a conducting film on the Si_3N_4/borosilicate sample required for the FIB/SEM treatment. Analysis of the cross-sections revealed that the waveguides with a designed slot width of 30 nm and 40 nm do not actually exhibit a gap but are solid ridge waveguides instead. This is caused by the resolution limit of the negative tone e-beam resist used for the lithography process. Furthermore, the plasma etching process is impeded in very small openings and therefore the gaps of the devices with $50\,\text{nm} \leq w_\text{d} \leq 125\,\text{nm}$ are not etched all the way to the substrate but have a remaining base of decreasing height h_b with increasing gap size. Nevertheless, all slot waveguides with $w_\text{d} \geq 150\,\text{nm}$ turned out to be completely developed. Figure 7.2 b) shows a top view SEM micrograph of the $w_\text{d} = 125\,\text{nm}$ device which reveals a homogeneous profile along the longitudinal

[2]NGJ35, see Appendix D.4.

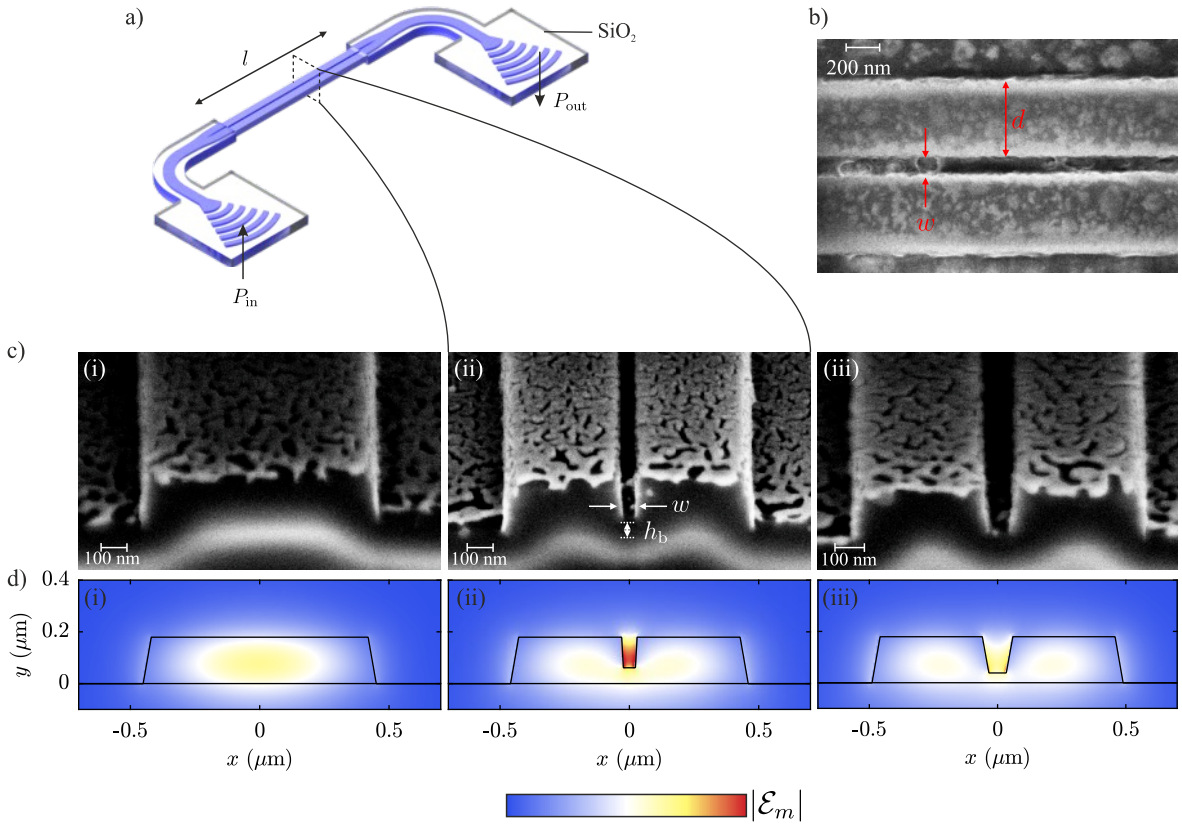

Figure 7.2: Waveguide structure and mode profiles. a) Schematic of the slot waveguides. The probe light P_{in} is coupled into a ridge waveguide via a grating coupler and guided to a Y junction which transforms the ridge waveguide into a slot waveguide. Couplers and splitters are covered with an SiO_2 layer. The uncovered region of length l is accessible to the atoms. The output P_{out} is detected with a photo multiplier tube. b) Top view SEM image of the $w_{\mathrm{d}} = 125\,\mathrm{nm}$ slot waveguide. The white patches and craters are due to an "ESpacer" coating to prevent charge buildup during imaging. c) FIB/SEM images showing the cross-sections of the $w_{\mathrm{d}} = 40\,\mathrm{nm}$ (i), $w_{\mathrm{d}} = 75\,\mathrm{nm}$ (ii) and $w_{\mathrm{d}} = 125\,\mathrm{nm}$ (iii) slot waveguides [164]. The white patches are sputtered gold to prevent charge buildup. d) Mode profiles of the fundamental TE mode corresponding to the devices shown in b).

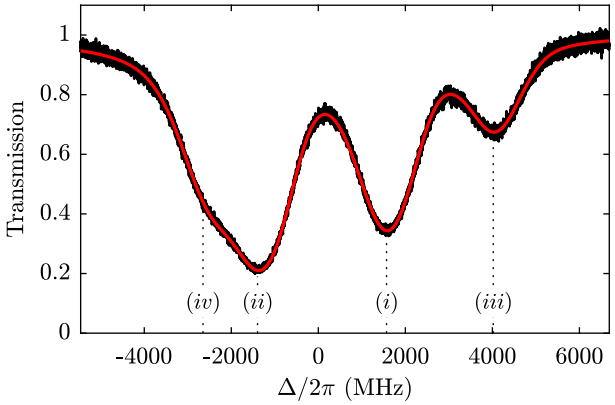

Figure 7.3: Transmission spectrum of the $w_\mathrm{d} = 75\,\mathrm{nm}$, $l = 200\,\mu\mathrm{m}$ slot waveguide with an atom density of $\mathcal{N} \approx 3.5 \times 10^{14}\,\mathrm{cm}^{-3}$. The red curve is an asymmetric Voigt fit. The dotted lines indicate the transition frequencies from the Rb^{85} $\mathrm{S}_{1/2}$ F = 2 (*i*), F = 3 (*ii*) and Rb^{87} $\mathrm{S}_{1/2}$ F = 1 (*iii*), F = 2 (*iv*) to the $\mathrm{P}_{3/2}$ states.

direction of the waveguide. The rough surface structure in this image is due to an "ESpacer" which forms a conductive polymer layer on the chip to prevent charge up during imaging.

The waveguide modes for the geometries deduced from the FIB/SEM analysis have been calculated with a finite element method using COMSOL Multiphysics. Due to the rectangular geometries of the waveguides all modes mentioned here are TE-like and TM-like modes exhibiting a small fraction of the respective field also in the other components[3]. The waveguides can in principle support up to three modes, however, as discussed below, we believe that only the fundamental TE mode is guided in all the structures. The electric field profiles of the fundamental mode are shown in Figure 7.2 d) for three different design widths w_d.

For each slot width a transmission spectrum has been recorded by scanning the laser over the Rb D_2 line, an example of which is shown in Figure 7.3 for the $w_\mathrm{d} = 75\,\mathrm{nm}$ slot waveguide at an atom density of $\mathcal{N} \approx 3.5 \times 10^{14}\,\mathrm{cm}^{-3}$. We fit the spectra with an asymmetric Voigt profile [165], see Appendix B, to account for the distribution of red-shifts due to atom-surface interactions which results in an asymmetric line shape. An excellent agreement between this model and the data is also shown in Figure 7.3. Note that the signal obtained from a slot waveguide originates from contributions of atoms in the slot itself but also from atoms in the evanescent field of the remaining geometry, see Figure 7.2 c).

The expected saturation intensity for the transit time broadened linewidth is reached for an atom located at the position of maximum intensity in the $w_\mathrm{d} = 50\,\mathrm{nm}$ slot with

[3]For the sake of brevity, we hereafter label them as TE and TM modes

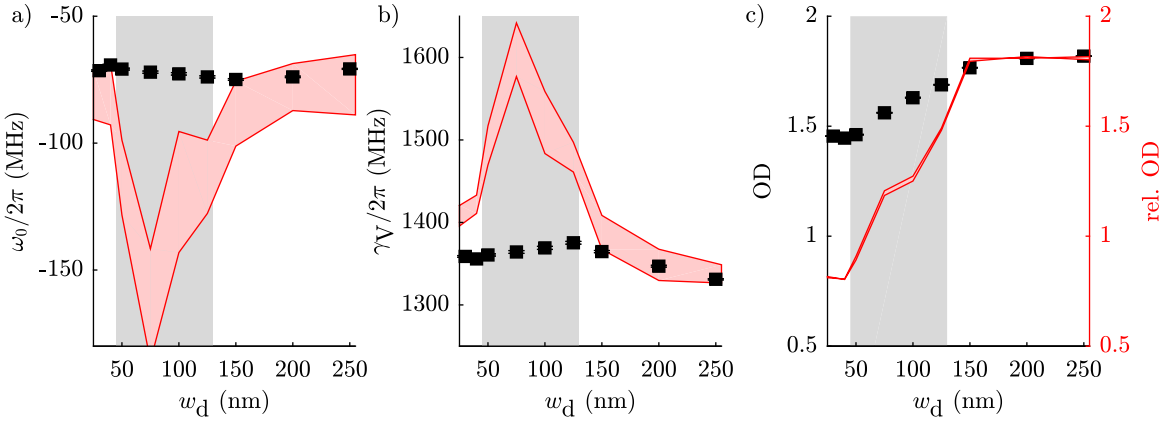

Figure 7.4: Lineshape parameters of the experimental spectra and Monte Carlo simulation results versus design slot width w_d. Black squares show experimental data and the red areas correspond to simulation results taking into account the uncertainty of the CP potential calculations. The gray shaded area indicates the interval $50\,\text{nm} \leq w_d \leq 125\,\text{nm}$ where the slot is not yet completely developed. a) Center frequency ω_0 of the D_2 spectrum relative to the center frequency obtained in a reference cell. b) Voigt width γ_V (FWHM). c) Optical depth of the Rb^{85} $5S_{1/2}, F = 3 \rightarrow 5P_{3/2}, F = 4$ transition. The simulation results for the OD are normalized to the maximum values of the measured OD and presented as relative OD (right ordinate) for a better comparison with the experimental data.

a mode power of $\sim 15\,\text{nW}$. In a power dependent measurement series we found the atoms to saturate at an input power of $\sim 12\,\mu\text{W}$, in agreement with the estimated mode power, taking into account coupling losses and the intensity distribution of the mode. The input power for the experiments presented in this section was $P_{in} \approx 400\,\text{pW}$, and therefore well below the power required to reach the saturation intensity. The atom density was set to $\mathcal{N} \approx 3.5 \times 10^{14}\,\text{cm}^{-3}$.

7.2.2 Results

The results of the slot width dependent measurements are shown as black squares in Fig. 7.4. As the atoms are probed in close vicinity to the waveguide, Casimir–Polder potentials lead to a red shift of the resonance on the order of $2\pi \times 70\,\text{MHz}$, see panel a). A shift of this magnitude would be experienced by an atom in $\sim 30\,\text{nm}$ distance to waveguide surface[4]. For comparison, the $1/e$ decay length of the evanescent field is on the order of $\sim 80\,\text{nm}$. The linewidth shown in b) increases for a growing slot width

[4] Calculated using the infinite plane approach (see section 4.2) for a material stack as "seen" by an atom above the top surface of the waveguide.

up to $w_\mathrm{d} = 125\,\mathrm{nm}$ and drops again for larger slot widths. The rise in linewidth can be explained by a growing slot volume and therefore more and more atoms from inside the slot region contribute to the signal. Because these atoms have very little time to interact with the light field, they exhibit a large transit time broadened linewidth. At $w_\mathrm{d} = 125\,\mathrm{nm}$ the dimensions become similar to the decay length of the evanescent field of the remaining cladding and, therefore, the linewidth reaches its maximum. The further trend of the linewidth is determined by the Doppler width, which is decreasing for growing slot widths as the effective mode index declines. The OD for the Rb^{85} $5\mathrm{S}_{1/2}, F = 3 \rightarrow 5\mathrm{P}_{3/2}, F = 4$ transition is shown in panel c) and is an indicator for the strength of the atom-light interaction assuming a fixed number density and waveguide length. For atoms at rest and in the limit of low saturation, the OD is proportional to the percentage of power outside the waveguide η, see eq. (2.4). According to our mode simulations, η increases for growing slot widths up to its maximum at $w_\mathrm{d} = 125\,\mathrm{nm}$ and then slightly decreases for higher slot widths (see Appendix C.3). This behavior is reproduced by the measured OD only to some degree but, as we have thermal atoms in our experiment, the OD is influenced by motional effects and a deviation from the cold atom picture is expected.

To understand the interaction of a thermal vapor with the waveguide mode depending on the exact slot geometry, we developed a model based on Monte Carlo simulations of atomic trajectories to account for the various effects arising in this system, see section 4.3 for details on the simulation method. In this model, the waveguide geometry is implemented with the dimensions inferred from the FIB-SEM measurements described earlier, and the corresponding modes are used to calculate position dependent Rabi frequencies and decay rates into these modes. Casimir–Polder potentials as well as the spontaneous emission rate, which is spatially modified due to the presence of the dielectric, are calculated with the DDA approach[5], see section 4.2.

The results of these simulations and the experimental data for the different slot widths are shown in Figure 7.4. Since we are only interested in the relative change of the OD as a function of slot width, we normalize the ODs of the simulations to the maximum measured OD value for easier comparison to the experimental behavior. Here, the trend of increasing OD with growing slot size is reproduced by the simulation, however, the relative difference between maximum and minimum OD is slightly larger for the simulation results. For the strip waveguides ($w_\mathrm{d} \leq 40\,\mathrm{nm}$) and the completely resolved slots ($w_\mathrm{d} \geq 150\,\mathrm{nm}$) we achieve good agreement in the line shifts and Voigt widths, even quantitatively. There are obvious discrepancies for the four slots with $50\,\mathrm{nm} \leq w_\mathrm{d} \leq 125\,\mathrm{nm}$. This interval corresponds to the devices where the slot starts to form but is not yet etched all the way to the substrate. Possible causes for the deviations between experiment and simulations are discussed in the following subsection.

[5]DDA = Discrete Dipole Approximation.

7.2.3 Discussion

The outliers in the line shift and line width within the gray shaded area of Figure 7.4 suggest that the atom-light interaction might be overestimated in the slot itself. This could be caused by either a reduced atom density inside the slot in comparison to the surrounding volume or by deviations in the mode profile. The likelihood for the presence of higher order modes is discussed in Appendix C.1 with the outcome that the fundamental mode should be dominant. Also, the Doppler widths extracted from fits to the experimental spectra follow the trend of the effective indices of the fundamental mode quite well, which is a further indication that the atoms interact with this mode since the Doppler width is proportional to the effective mode index.

The mode profile could be altered by Rb sticking to the waveguide surface and therefore creating a metallic layer. In order to investigate this situation, we simulated the transmission properties of the slot waveguides with a thin metal layer on top using COMSOL (see Appendix C.2). The metal layer was set up to have the optical properties of Rb and its thickness was adjusted such that the transmission losses were corresponding to experimentally obtained values before and after exposing the waveguides to Rb vapor (see section 4.5). The result suggests a Rb layer thickness of $\sim 1\,\mathrm{nm}$ which however does not influence the mode profile perceptibly.

Adsorbed Rb atoms on top of the Al_2O_3 layer can also give rise to static electric fields due to dipole moments caused by partial charge transfer between the Rb adatom and the surface atoms [166–168]. The interaction of the probed atoms with these electric fields manifests itself in a Stark shift of the atomic energy levels. While the top surface of the waveguides is generally smooth, the rough slot sidewalls[6] offer a larger effective surface which could accommodate a higher number of adatom dipoles and therefore lead to a lower signal contribution from the slot itself by shifting the atoms out of resonance. In Appendix C.4 we model the effects of surface dipoles on the transmission spectrum of the $w_\mathrm{d} = 75\,\mathrm{nm}$ device, which exhibits the largest discrepancies between experiment and simulation in the previous section. We consider two scenarios: the first one corresponds to a uniform distribution of dipoles on the entire chip, whereas in the second one only the sidewalls are covered with dipoles. In both cases the dipoles lead to an increased shift and broadening compared to the situation without dipoles. Consequently, surface dipoles can not reduce the atomic response within the slot region sufficiently to explain the above discussed deviations, at least for the two studied examples and the underlying assumptions.

Another reason for less signal contribution from the slot would be a reduced atom number density within the slot as compared to the volume around the waveguide which can arise if the adsorption rate of atoms onto the waveguide surface is much larger than the desorption rate. In this case most of the atoms had to make it through the narrow

[6] The quality of the waveguide top surface is usually determined by the layer growth process resulting in a smooth surface, whereas the etching process creates rough sidewalls.

slot opening to enter the slot region, which is restricted due to the geometrical obstructions. Simulations with different ratios of ad- and desorption rates showed indeed much better agreement when desorption becomes negligible compared to adsorption but it is unclear to what extent this constructed behavior reflects the real experimental conditions.

Besides the rate also the directions of desorbing atoms influences their interaction with the slot mode. Various experiments in surface science have reported on non-cosine distributions for the directions of desorbing molecules (see e.g. [115] and references therein). They find distributions which are strongly peaked around the surface normal and can be usually described by a $\cos^n \theta$ function. Hence we checked the influence of the angle distribution of atoms leaving the surface for several exponents ($1 \leq n \leq 100$) but could not obtain a better agreement between simulation and experimental results compared to the usual cosine distribution. The roughness of the waveguide surface could also lead to an anomalous ad- and desorption behavior, not accounted for in our simulations.

The determination of the slot waveguide dimensions via SEM images of their cross sections involves further uncertainties due to possible distortions caused by electrostatic charging of the chip. Also, as one can sense from Figure 7.2 c), it is difficult to pinpoint the borders of the structure in theses images. In order to improve the quality of this model, a better knowledge of the actual waveguide geometry would be necessary, especially if the contours are rather complex as it is the case for the narrow slot waveguides. In addition, an experimental characterization of the guided modes, e.g., using 3-D near-field imaging [169], would provide valuable input data for our simulations.

Further systematic investigations are required to gain more insight into the interaction of thermal atoms with slot waveguides. In particular, covering the top and side domains of the waveguides, e.g., with an SiO_2 mask and etching the substrate underneath the slot, as shown in Figure 6.9 d) in section 6.4.2, would allow to obtain a signal solely originating from atoms inside the slot. Moreover, by fabricating samples with varying etching depth one could study the influence of the pedestal in the narrow underdeveloped slots.

7.3 Atom-atom interactions

In the experiments described so far, atoms have been treated as independent objects. However, if the separation R between two atoms is sufficiently small, interatomic potentials have an effect on the spectral properties, namely a broadening and shift of the resonance line (see, e.g., [170]). Generally, the interaction potential between two atoms is expressed in a multipole expansion [171], where for neutral atoms the leading term is the $1/R^3$ dipole-dipole interaction. Here, we only consider the interaction between

two identical atoms, as it is the case for the experiment described below[7]. A first order term in the interaction energy is obtained if one of them is in the ground state, while the other one is in an excited state and both states are connected via a dipole transition (resonant dipole-dipole interaction). In this case, the interaction strength scales linearly with the atom density $\mathcal{N}$, since $\mathcal{N} \propto R^{-3}$. However, this is only correct if $kR < 1$, where k is the wavenumber corresponding to the transition wavelength, as for larger separations retardation effects become relevant [172], though for $kR \ll 1$ also the dipole approximation breaks down. For the D_2 transition of rubidium, the condition $kR < 1$ is fulfilled when $\mathcal{N} > 8.5 \times 10^{13}\,\mathrm{cm}^{-3}$, corresponding to a temperature $T > 150\,^{\circ}\mathrm{C}$.

The role of dipole-dipole interactions in atomic systems has been studied for many decades but still seems to be not very well understood [67, 68]. The interpretation of experimental results with the existing theory is often unsuccessful or requires additional parameters such as a "collisional shift" in order to find agreement [173]. Therefore, continuing investigations in this field are required on the experimental as well as the theoretical side. An in depth understanding of this subject is not only relevant for a microscopic description of fundamental phenomena, such as light propagation in a medium, but also for atom based applications like atomic clocks [174]. Spectroscopy with integrated photonic structures could offer a valuable contribution to this subject since the transversal dimensions of the probing region can be on a sub-wavelength scale, therefore constituting a quasi one-dimensional system. Here, we take the first steps in this direction by probing line shifts and line broadenings at elevated atom densities with a slot waveguide. Before discussing the results of this measurement we briefly review the relevant shift and broadening mechanisms in a dense atomic gas.

7.3.1 Line shift

In a dielectric medium, the electric field experienced by an atom inside the medium is the sum of the incident electric field and the field generated by the neighboring dipoles. Standard textbooks [162, 175] treat the surrounding dipoles as a continuous polarization, which results in a local field correction. A consequence thereof is a density dependent red shift of the atomic resonance, known as the Lorentz–Lorenz shift [176], given by [35]

$$\Delta_{\mathrm{LL}} = -\frac{\mathcal{N} d^2}{3\epsilon_0 \hbar}\,, \tag{7.3}$$

where d is the dipole matrix element. The Lorentz–Lorenz shift has been identified in a number of experiments (e.g. [35, 173, 177]), however, in each case combined with additional contributions to the total line shift.

[7] Apart from different absorption and emission wavelengths of different velocity classes due to the Doppler effect.

A further effect which has until recently been associated with resonant dipole-dipole interactions is the so called "cooperative Lamb shift" (CLS) [178]. For thermal atoms the CLS has been measured in case of a slab geometry using rubidium in a very thin vapor cell [35]. However, it has lately been revealed that the CLS in a slab of atoms arises from an etalon effect due to reflections at the boundary of the slab [66–68].

It has also been pointed out [65] that mean field approximations, such as the local field correction resulting in the Lorentz–Lorenz shift, are not valid in the absence of inhomogeneous broadening due to correlations between nearby atoms, mediated by dipole-dipole interactions. This behavior has been observed in numerical electrodynamics simulations [65, 67] and confirmed experimentally in cold atomics gases [179–181]. Within this theory it is assumed that the presence of inhomogeneous broadening, such as in a thermal gas, leads to a suppression of these correlations and restores the mean field effects.

7.3.2 Self broadening

Atoms in a thermal gas undergo collisions during which they can get very close to each other, thus experiencing strong interactions for a short period of time. If the duration of a collision is short compared with the time between collisions, such a process can be treated in the impact approximation [170, 182]. Here, the assumption is made, that only two atoms are involved in the collision (binary approximation[8]) which move in a straight path with a distance of closest approach defined by an impact parameter ρ. Thus, the dipole-dipole interaction between the two atoms is transient, leading to a dephasing of the dipoles.

Within these approximations, the effect of collisions between identical atoms on the optical response is a broadening of the spectral line shape, commonly known as self broadening. The increase in the Lorentzian line width is predicted to be [170, 184]

$$\Gamma_{\mathrm{col}} = \beta\mathcal{N} \approx 2\pi \times \sqrt{\frac{2J_e+1}{2J_g+1}}\Gamma_0 \left(\frac{\lambda}{2\pi}\right)^3 \mathcal{N}\,, \tag{7.4}$$

where J_g and J_e are the angular momenta of the ground state and the excited state, respectively. In case of the Rb D_2 line we obtain for the self broadening coefficient $\beta/2\pi = 1.03 \times 10^{-7}\,\mathrm{Hz\,cm^3}$.

A line shift due to collisions of identical atoms in the limit of dipole-dipole interactions is expected to vanish in the impact approximation [170, 185, 186]. However, for large impact parameters ρ, corresponding to weaker collisions, a finite line shift remains [182, 186].

[8] The binary approximation remains valid as long as $\mathcal{N}\rho_{\mathrm{W}}^3 \ll 1$, where ρ_{W} is the Weisskopf radius [183], which is $\rho_{\mathrm{W}} = 14\,\mathrm{nm}$ for the Rb D_2 transition [184]. Hence, this approximation breaks down if $\mathcal{N} \geq 1 \times 10^{17}\,\mathrm{cm^{-3}}$, which significantly exceeds the densities investigated here.

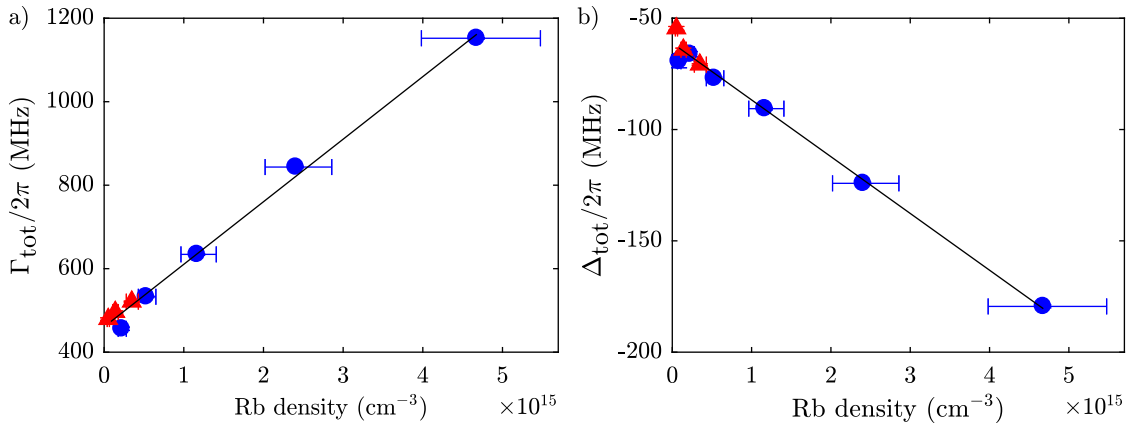

Figure 7.5: Density dependent measurements in the 50 nm slot waveguides. a) Lorentzian linewidth for the $l = 30\,\mu m$ (blue circles) and $l = 200\,\mu m$ (red triangles) devices. b) Corresponding line shift. The black lines are linear fits to the data.

7.3.3 Experimental results

To study atom-atom interactions in the evanescent field of a slot waveguide we recorded number density dependent transmission spectra with two devices which both have a designed slot width of $w_d = 50\,nm$, but different exposed sections with lengths $l = 30\,\mu m$ and $l = 200\,\mu m$, respectively. Both waveguides are realized on the same chip, where the two different lengths are defined by the spatial coverage of the SiO_2 layer, see Figure 7.2 a). The shorter length allows for the investigation of higher number densities without the vapor getting optically thick. Note that the 50 nm slot waveguide does not exhibit a fully developed slot but has a remaining pedestal of $h_b \approx 113\,nm$. This was determined for the $l = 200\,\mu m$ device using FIB/SEM processing and is assumed to be also the case for the $l = 30\,\mu m$ device.

The Rb density was varied by adjusting the reservoir temperature in the range of 150 °C to 250 °C. To extract the line center ω_0 and Voigt width (FWHM) the spectra are fitted with an asymmetric Voigt function as described in section 7.2.1. The Lorentzian contribution to the Voigt width is extracted by assuming a Doppler broadening corresponding to the cell temperature and the simulated effective mode index of the waveguide. The result of these measurements is shown in Fig. 7.5. The large horizontal error bars arise from the uncertainty in the derivation of the Rb density from the reservoir temperature. The density dependence of the Lorentzian width is plotted in part a) and shows a nearly linear increase with growing number density. This behavior is attributed to a self-broadening contribution Γ_{col} to the homogeneous linewidth. Assuming this, the total Lorentzian width is given by

$$\Gamma_{tot} = \Gamma + \Gamma_{TT} + \beta\mathcal{N}\,, \tag{7.5}$$

where Γ_{TT} is the transit time broadening[9]. By fitting a linear function to the data, we find for the self-broadening coefficient $\beta/2\pi = (1.5 \pm 0.3) \times 10^{-7}\,\mathrm{Hz\,cm^3}$ which is somewhat larger than the theoretical prediction of $\beta/2\pi = 1.03 \times 10^{-7}\,\mathrm{Hz\,cm^3}$ calculated in section 7.3.2. However, the theory behind eq. (7.4) includes various approximations and does not account for the inhomogeneous environment of an atom close to a waveguide. Therefore, it might be more appropriate to compare the above result to the Rb D_2 self-broadening coefficient $\beta/2\pi = (1.1 \pm 0.17) \times 10^{-7}\,\mathrm{Hz\,cm^3}$ obtained in an evanescent wave spectroscopy experiment [187]. In this case, the experimental conditions are rather similar to our work and the agreement is within the given uncertainties.

With increasing number density the line also shifts linearly to lower frequencies as shown in Fig. 7.5(b). The gradient of the line shift is determined from a linear fit to be $\Delta_{\mathrm{tot}}/\mathcal{N} = 2\pi \times (-0.25 \pm 0.07) \times 10^{-7}\,\mathrm{Hz\,cm^3}$. Two mechanisms are known to contribute to a density dependent shift in a thermal vapor: a collision induced shift Δ_{col} and a shift induced by dipole-dipole interactions Δ_{dd} between the atoms. Further, the total line shift Δ_{tot} contains an offset for $\mathcal{N} \to 0$ attributed to atom-surface interactions Δ_{CP}, hence,

$$\Delta_{\mathrm{tot}} = \Delta_{\mathrm{CP}} + \Delta_{\mathrm{col}} + \Delta_{\mathrm{dd}}\,. \tag{7.6}$$

The gradient of our line shift is consistent with the collisional shift of $\Delta_{\mathrm{col}}/\mathcal{N} = 2\pi \times (-0.25 \pm 0.01) \times 10^{-7}\,\mathrm{Hz\,cm^3}$ for the Rb D_2 line measured by Keaveney *et al.* [35], assuming that the dipole-dipole contributions are negligible. The Lorentz–Lorenz shift (7.3) would be $\Delta_{\mathrm{LL}}/\mathcal{N} = 2\pi \times -0.728 \times 10^{-7}\,\mathrm{Hz\,cm^3}$ for the Rb D_2 line. One has to be aware, that the local field leading to eq. (7.3) was calculated by Lorentz for a homogeneous and isotropic crystal [176]. However, the penetration depth of the probe field outside the waveguide is on the order $\lambda/2\pi$, so the local field is not fully developed in this situation [188]. Furthermore, atom-surface interactions introduce additional inhomogeneity in the probed region, as dipole-dipole interactions between atom pairs normal to the waveguide surface are not resonant. This would lead to a decreased Δ_{dd}, like we observe in our experiments.

A detailed study of the dipole-dipole interactions would require a (DDA[10]-) simulation of the scattering of the guided mode by the atomic vapor which accounts for correlations and inhomogeneous (Doppler) broadening of the atoms [179, 180]. Further, all dipole-dipole interactions taking place in the vicinity of the waveguide surface would have to incorporate the macroscopic environment requiring an additional scattering simulation for each pair of atoms. The implementation thereof is a complex task.

[9] The line shape arising from transit effects is not exactly Lorentzian, as shown in section 1.2, but we relate it here to the Lorentzian part, since we reject the Doppler part from the total Voigt profile in order to obtain Γ_{tot}.

[10] Discrete dipole approximation.

8 Two-photon waveguide spectroscopy

The spectral linewidth of atoms in a thermal vapor is mostly dominated by Doppler broadening, which is even enhanced in case of waveguide spectroscopy because of the wave vector of the confined probe field being increased by the effective mode index n_{eff} compared to free space. A common technique to determine the Doppler-free linewidth[1] is saturated absorption spectroscopy [73], where a strong pump field is counter-propagating to the probe field at the same frequency and thus a velocity group close to zero is addressed. This method is however not compatible with our integrated spectroscopy setup due to interference effects, as described in more detail below.

Therefore, we perform two photon spectroscopy in a ladder-type configuration involving the $5S_{1/2}$, $5P_{3/2}$ and $5D_{3/2}$ levels of Rb^{85}. Two counter-propagating modes of different wavelength allow us to investigate almost Doppler-free and mostly transit time broadened line profiles in an integrated spectroscopy setup. Furthermore, this experiment demonstrates evanescent waveguide spectroscopy of an excited state higher than the 5P level, which is more prone to atom-surface interactions.

8.1 Three-level system

We consider a three-level system in a ladder configuration as shown in Figure 8.1. A probe field ω_{p} with Rabi frequency Ω_{12} is applied to the $|1\rangle \rightarrow |2\rangle$ transition, separated by ω_{12}, with detuning $\Delta_{12} = \omega_{\text{p}} - \omega_{12}$. Additionally, a coupling field ω_{c} with Rabi frequency Ω_{23} is applied to the $|2\rangle \rightarrow |3\rangle$ transition, separated by ω_{23}, with detuning $\Delta_{23} = \omega_{\text{c}} - \omega_{23}$. The decay rates of level $|2\rangle$ and $|3\rangle$ are given by Γ_{21} and Γ_{32}, respectively. Following the procedure of section 1.1 we obtain the equations of motion for

[1] The residual line width is however saturation broadened depending on the intensities of both pump and probe field.

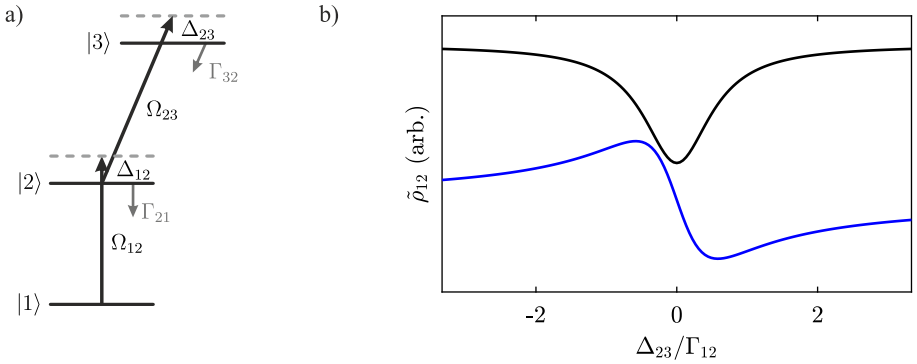

Figure 8.1: Three-level ladder system. a) Atomic level scheme. b) Real part (blue line) and imaginary part (black line) of the coherence between level $|1\rangle$ and $|2\rangle$ as a function of coupling detuning Δ_{23}.

the density matrix elements in the rotating wave approximation:

$$\frac{\partial}{\partial t}\tilde{\rho}_{11} = \Gamma_{21}\tilde{\rho}_{22} - \mathrm{Im}\left(\Omega_{12}^{*}\tilde{\rho}_{12}\right) , \tag{8.1a}$$

$$\frac{\partial}{\partial t}\tilde{\rho}_{12} = -\left(\frac{\Gamma_{21}}{2} + \mathrm{i}\Delta_{12}\right)\tilde{\rho}_{12} - \frac{\mathrm{i}}{2}\left[\Omega_{12}(\tilde{\rho}_{22} - \tilde{\rho}_{11}) - \Omega_{23}^{*}\tilde{\rho}_{13}\right] , \tag{8.1b}$$

$$\frac{\partial}{\partial t}\tilde{\rho}_{13} = -\left[\frac{\Gamma_{32}}{2} + \mathrm{i}\left(\Delta_{12} + \Delta_{23}\right)\right]\tilde{\rho}_{13} + \frac{\mathrm{i}}{2}\left(\Omega_{12}\tilde{\rho}_{23} - \Omega_{23}\tilde{\rho}_{12}\right) , \tag{8.1c}$$

$$\frac{\partial}{\partial t}\tilde{\rho}_{22} = -\Gamma_{21}\tilde{\rho}_{22} + \Gamma_{32}\tilde{\rho}_{33} + \mathrm{Im}\left(\Omega_{12}^{*}\tilde{\rho}_{12}\right) - \mathrm{Im}\left(\Omega_{23}^{*}\tilde{\rho}_{23}\right) , \tag{8.1d}$$

$$\frac{\partial}{\partial t}\tilde{\rho}_{23} = -\left(\frac{\Gamma_{21} + \Gamma_{32}}{2} + \mathrm{i}\Delta_{23}\right)\tilde{\rho}_{23} - \frac{\mathrm{i}}{2}\left[\Omega_{12}^{*}\tilde{\rho}_{13} + \Omega_{23}\left(\tilde{\rho}_{33} - \tilde{\rho}_{22}\right)\right] , \tag{8.1e}$$

$$\frac{\partial}{\partial t}\tilde{\rho}_{33} = -\Gamma_{32}\tilde{\rho}_{33} + \mathrm{Im}\left(\Omega_{23}^{*}\tilde{\rho}_{23}\right) . \tag{8.1f}$$

Under the experimental conditions of this work equations (8.1) need to be modified for two reasons: first, the close proximity to the waveguide surface leads to Casimir–Polder shifts of the energy levels (see section 4.2). Second, in a thermal gas the Doppler shift has to be incorporated into the detunings. If the probe and coupling beams are counter-propagating, the altered detunings are

$$\Delta_{12} \to \Delta_{12} - \Delta_{\mathrm{CP}}^{21} - \frac{\omega_{\mathrm{p}}}{c}v\,, \qquad \Delta_{23} \to \Delta_{23} - \Delta_{\mathrm{CP}}^{32} + \frac{\omega_{\mathrm{c}}}{c}v\,, \tag{8.2}$$

where $\Delta_{\mathrm{CP}}^{ji}$ is the difference of the Casimir–Polder potentials of state $|j\rangle$ and state $|i\rangle$ and c is the speed of light in the given medium. The residual Doppler broadening of the two-photon transition is determined by the frequency difference of the probe and coupling fields. Hence, if the frequencies of the probe and pump fields are similar, the two-photon signal is almost Doppler-free.

We now briefly discuss the spectroscopic features of a probe field propagating through such a three-level medium. In absence of the coupling field, a weak probe field resonant to the lower transition gets absorbed. By adding a strong coupling field resonant to the upper transition, absorption of the probe field gets reduced. This behavior is partially due to electromagnetically induced transparency (EIT) caused by destructive interference in absorption - a comprehensive review on this phenomenon is presented in [189]. Furthermore, the coupling field generates an Autler–Townes splitting [190, 191] of states $|2\rangle$ and $|3\rangle$ which dominates the transparency feature if Ω_{23} is much larger than the residual Doppler linewidth of the two-photon transition [192]. Figure 8.1 b) shows the steady state solution of $\tilde{\rho}_{12}$, eq. (8.1b), as a function of coupling field detuning Δ_{23} and $\Delta_{12} = 0$. The imaginary part of $\tilde{\rho}_{12}$ is proportional to the probe field absorption, whereas the real part determines the dispersive properties of the medium. The effect of the coupling field is to reduce the absorption around $\Delta_{23} = 0$. This transparency feature is associated with a steep dispersion in a region of low absorption.

If the $|2\rangle \rightarrow |3\rangle$ transition is not closed, population can be transfered to a hyperfine ground state other than $|1\rangle$ via optical pumping. In this case, the coupling field can also produce a transparency feature [193]. However, this process is only effective if the interrogation time by the probe field is much larger than the lifetimes of the upper states. Because this condition is not fulfilled for thermal atoms in the evanescent field of a waveguide, we can neglect this pumping effect in our experiments.

8.2 Experimental realization

For this experiment, we use the Rb^{85} transitions shown in Figure 8.2 a). The 780 nm probe light is locked to the $5S_{1/2}$, $F = 3 \rightarrow 5P_{3/2}$, $F = 4$ transition using DAVLL [194] in a reference vapor cell, while the 776 nm coupling light is scanned over the $5P_{3/2}$, $F = 4 \rightarrow 5D_{3/2}$, $F = 3, 4$ transitions. The hyperfine splitting between the $F = 3$ and 4 levels in the $5D_{3/2}$ state is $2\pi \times 18.6$ MHz [195] and the natural linewidth is about $2\pi \times 0.66$ MHz [196]. The probe and coupling fields are counter-propagating and have similar wavelengths which results in an almost Doppler-free two-photon signal. Nevertheless, the large transit time broadened linewidth implies a contribution of atoms with a large range of non-zero longitudinal velocities to the two-photon signal.

8.2.1 Photonic circuit and experimental procedure

A schematic of the two-photon spectroscopy device is shown in Figure 8.2 b). The whole device is covered with a 600 nm thick HSQ layer except for a section of length $l = 1$ mm where the atoms can interact with the evanescent light fields. The circuit consists of ridge Si_3N_4 waveguides of height $h = 175$ nm and width $w = 450$ nm. A

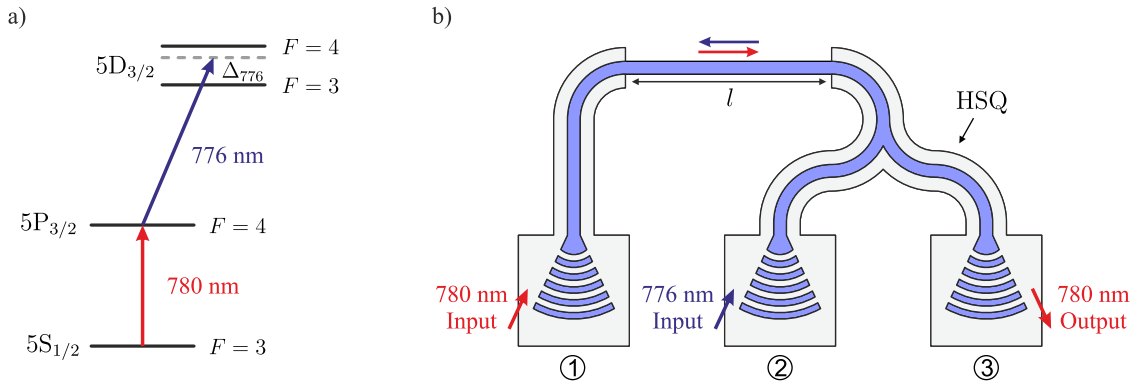

Figure 8.2: Two-photon spectroscopy. a) Relevant transitions of Rb^{85}. b) Schematic of the photonic circuit which allows for counter-propagating modes of the probe and coupling fields.

relatively narrow width was chosen in order to slightly increase the evanescent decay length at the side walls of the core ($\gamma_x = 94\,\text{nm}$ instead of $\gamma_x = 81\,\text{nm}$ for a $w = 1100\,\text{nm}$ waveguide). The 780 nm probe light is injected into the waveguide via grating coupler 1. After passing the uncoated section, the probe light is split into two arms via a 50:50 Y junction. Each arm is connected to an individual grating coupler, where the 776 nm coupling light is injected into coupler 2 and the probe light is collected from coupler 3. In doing so, the probe and coupling modes are counter-propagating in the uncoated section, whereas the probe light can be detected without being directly spatially overlapped with the input coupling beam. However, since the input power of the coupling beam is much larger than the output power of the weak probe light, a fraction of the scattered coupling light is collected together with the probe light from port 3. The 776 nm coupling light can be sufficiently suppressed using a narrow 780 nm bandpass filter[2] in front of the PMT. When performing saturated absorption spectroscopy with this device, the pump light (which would replace the coupling light from above) can not be suppressed via frequency filtering since it has the same wavelength as the probe light. Therefore, potential lamb dips in the probe signal are masked by strong interference features when scanning the laser frequency which makes this spectroscopy method inapplicable in our setup. To improve the signal to noise ratio of the recorded spectra we modulate the amplitude of the 776 nm light using an acousto-optic modulator (AOM) and extract the probe signal using a lock-in amplifier.

[2]Semrock MaxLine LL01-780-12.5

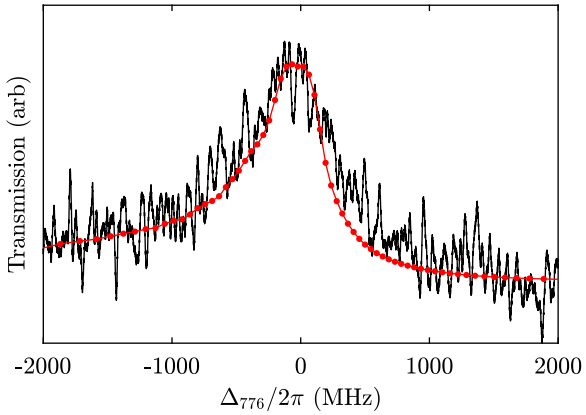

Figure 8.3: Probe transmission signal of a $w = 450\,\text{nm}$ waveguide with counter propagating coupling field (black curve) and corresponding Monte Carlo Simulation (red curve). For the simulated spectrum, the center frequency has been shifted by $+2\pi \times 164\,\text{MHz}$ to the center position of the measured feature and the amplitude is normalized for a better comparison between the experimental and simulated line shapes.

8.2.2 Results

An exemplary two-photon spectrum obtained with the photonic circuit described above is shown in Figure 8.3 for an atom density of $\mathcal{N} \approx 5 \times 10^{13}\,\text{cm}^{-3}$. The probe and coupling input power[3] were set to 70 nW and 400 µW, respectively. Assuming input coupling losses of $\sim 10\,\%$ these powers correspond to Rabi frequencies of $\Omega_\text{p}/2\pi \approx 48\,\text{MHz}$ and $\Omega_\text{c}/2\pi \approx 528\,\text{MHz}$ at the position where the evanescent field drops to its $1/e$ value[4]. The probe signals shows a transmission feature with a total line width (FWHM) of $\sim 2\pi \times 860\,\text{MHz}$ and is asymmetric with a tail towards lower coupling frequency. Note, that both transitions involving the $5\text{D}_{3/2}$, $F = 3$ and $F = 4$ levels contribute to the signal, however, the hyperfine splitting of $2\pi \times 18.6\,\text{MHz}$ can not be resolved because of the large line width. The line width is smaller than in the Doppler broadened D_2 spectra (FWHM $\sim 2\pi \times 1300\,\text{MHz}$) but still larger than the purely transit time broadened line width of $2\pi \times 440\,\text{MHz}$ obtained by Monte Carlo simulations, as described below. This additional broadening is partially due to distortion of the line shape caused by atom-surface interactions, which we will examine in the next paragraph. Furthermore, the large Rabi frequencies required to observe the two-photon signal give rise to power broadening.

The peak of the feature is shifted by $-2\pi \times 90\,\text{MHz}$ with respect to the center of

[3] Power of the laser focused onto the grating coupler.

[4] The peak Rabi frequencies at the surface of the waveguide are $\Omega_\text{p}/2\pi \approx 132\,\text{MHz}$ and $\Omega_\text{c}/2\pi \approx 1436\,\text{MHz}$.

gravity of the $5D_{3/2}$, $F = 3, 4$ EIT signals in the reference cell. This red shift is attributed to Casimir–Polder (CP) interactions of the atoms with the nearby surfaces, see section 4.2. Atoms at different positions within the evanescent field experience different CP shifts, leading to the asymmetric line shape. The CP shifts are quite different for the involved energy levels, since the $5D_{3/2}$ state has a larger polarizability as the $5P_{3/2}$ state. Additionally, for the $5D_{3/2}$ a larger number of virtual transition to nearby states exists. For atoms close to the top surface of the waveguide[5] the effective C_3 coefficient[6] of the $5S_{1/2} \rightarrow 5P_{3/2}$ transition is given by $C_3 = 1.18\,\mathrm{kHz\,\mu m^3}$, whereas for the $5P_{3/2} \rightarrow 5D_{3/2}$ transition we have $C_3 = 14.3\,\mathrm{kHz\,\mu m^3}$. These values have been obtained using the infinite plane approach, see section 4.2.1.

To model the 780 nm probe transmission in presence of a counter-propagating 776 nm coupling mode, we performed Monte Carlo simulations as detailed in section 4.3 extended by the optical Bloch equations (8.1) of a three level system. This simulation allows us to take into account the atomic motion and effects of spatial dispersion, as well as the involved CP potentials and mode distribution for the specific waveguide geometry. To obtain the probe field transmission, we use a different approach to the one described in section 4.3.3 in order to account for any coherent effects involved in EIT: the Monte Carlo simulation generates a time averaged position dependent local susceptibility $\chi_{\mathrm{loc}}(x, y, z) \propto \tilde{\rho}_{12}(x, y, z)$ for a set of detunings Δ_{776}. Subsequently, we calculate the complex propagation constant β of the waveguide with a cladding material determined by χ_{loc} using COMSOL. The probe transmission signal for a waveguide with an interaction region of length l can then be obtained via

$$T(\Delta_{776}) = \exp\left[-2\beta(\Delta_{776})l\right] . \tag{8.3}$$

The red curve in Figure 8.3 shows a fit of the simulation result to the measured transmission spectrum, where the absorption level, feature amplitude and center frequency position are free fit parameters. A frequency shift of $+2\pi \times 160\,\mathrm{MHz}$ of the simulation result is required to match the experimental data, which means that the simulation predicts a larger red shift than experimentally observed. This discrepancy might be caused by uncertainties in the calculation of the CP potentials for the $5D_{3/2}$ state. Due to the larger polarizability and the increased number of relevant transitions compared to the $5P_{3/2}$ state, this state is more sensitive to the actual condition of the waveguide surface which is by far not well defined in this experiment. Moreover, the physical properties of the involved materials might not exactly agree with the material data utilized in this calculation in the relevant wavelength ranges. While the line width of $\sim 2\pi \times 700\,\mathrm{MHz}$ is slightly smaller than in the experiment, the overall line shape including the asymmetric tail on the red side of the spectrum is well reproduced.

[5] These atoms "see" a material stack of 7 nm Al_2O_3, 175 nm Si_3N_4 and 1.1 mm SiO_2.

[6] Recalling eq. (4.27), the CP shift of an atomic level at a distance z to the surface is given by $U_{\mathrm{CP}}(z) = -\frac{C_\alpha}{z^\alpha}$, where close to the surface ($z \ll \lambda/2\pi$) $\alpha \approx 3$. The quantity which is actually measured in the experiment is the relative shift of the energy levels i, j involved in the transition. Hence, the effective C_3 coefficient is a constant given by $C_3 = \left[U^j_{\mathrm{CP}}(z) - U^i_{\mathrm{CP}}(z)\right] z^3$.

Although a sub-Doppler line width could be achieved in this experiment, there are possibilities to further decrease the line width of the spectroscopy signal. Improvement of the modulation, filtering and detection techniques should allow to obtain a signal at lower probe and coupling powers, thus reducing the effect of power broadening. In principle, transit time broadening could be diminished by increasing the waveguide width and involving additional atomic transitions. For example, using a resonant 780 nm pump beam aligned in the vertical direction perpendicular to the waveguide populates the $5P_{3/2}$ level of atoms which do not move substantially along the beam axis. Starting from the $5P_{3/2}$ level, V-type EIT could be performed between the $5D_{3/2}$ and $5D_{5/2}$ levels using counter-propagating 776 nm modes within the waveguide. This way, only atoms moving horizontally across the waveguide induce a transit time broadening, which again depends on the waveguide width. Finally, it should be noted that in reference [41] a transit time limited line width of $\sim 2\pi \times 300$ MHz has been observed in a 500 nm wide Si_3N_4 waveguide via the same excitation scheme as described above. However, they do not report any effects due to atom-surface interactions, which is surprising.

Summary

In this thesis, we have presented the integration of thermal alkali atoms with chip-based photonic waveguide structures. This hybrid approach combines the best of two worlds: on the one hand, alkali vapor cells offering a simple and flexible framework to study and utilize the properties of atoms, which represent a quantum system with well defined and narrow transition frequencies. On the other hand, integrated photonic circuits allowing for dense arrays of miniaturized optical devices on a chip, which enable the manipulation of light on a sub-micron scale within a stable and scalable architecture. The marriage of these two disparate technologies provides a platform for a wide variety of practical applications but also for fundamental studies of light-matter interaction. We have undertaken the first steps to realize this idea at our institute and developed considerable experimental and theoretical know-how which is collected in this work.

The experiments conducted during this thesis were based on Si_3N_4 photonic structures realized on a glass chip which was anodically bonded to a Rb vapor cell, except for the measurements with the Mach–Zehnder interferometer, which were performed in a vacuum chamber. The waveguide structures were equipped with grating couplers to couple between the guided and the free space mode, allowing us to flexibly arrange and address devices on the two dimensional chip surface. We could arbitrarily define volumes for the evanescent atom-light interaction to take place by masking the remaining chip with an SiO_2 layer. These waveguide cells already constitute fairly small devices which are convenient to work with and offer a huge potential for even further miniaturization. Several photonic circuits realized on different chips have been investigated in combination with Rb vapor during the course of this thesis. A summary of the results obtained with the individual devices is presented hereafter.

Ridge waveguide transmission

As a first proof of principle and to characterize the atomic vapor spectroscopy with integrated structures we performed transmission measurements using a simple ridge waveguide. A frequency scan over the Rb D_2 line revealed absorption of the guided light via the evanescent tail of the mode at moderate atom densities. The spectra exhibit additional line broadening compared to conventional free space spectroscopy. This is due to the larger wave vector of the guided mode which leads to enhanced Doppler broadening, and because of the short interaction time of the atoms with the evanescent

field which reveals itself in transit time broadening. Moreover, the entire spectrum is red shifted with respect to a reference measurement, which is a manifestation of Casimir–Polder interactions of the atoms with the dielectric surface, a consequence of probing the atoms in close proximity to the waveguide.

To model this system numerically, we have adapted the effective susceptibility method known from the work on selective reflection spectroscopy. This allowed us to simulate the light propagation in a waveguide surrounded by a homogeneous macroscopic medium with a complex refractive index corresponding to the properties of the Rb vapor including quenching collisions with the waveguide surface. Using this model, we could reproduce the ridge waveguide transmission spectra with excellent agreement. The same method also proved to be appropriate for different devices, if the specific waveguide geometry is not a critical aspect.

After exposing the chip to an alkali atmosphere, we witnessed transmission losses of the structures. A discussion within this work indicates, that the propagating mode is most likely attenuated by metallic alkali deposit on the waveguide surface. Quite some improvement could be achieved via an Al_2O_3 protection layer, although a residual attenuation remained.

Integrated Mach–Zehnder interferometer

Besides the absorptive properties of the atomic vapor, we also determined the associated phase shift of the guided mode. To perform phase sensitive measurements, we utilized an integrated MZI comprised of two waveguide arms, one of which is exposed to the atoms. The obtained spectra clearly exhibit dispersive features dictated by the real part of the atomic vapor susceptibility. Again, the experimental data could be very well reproduced using the effective susceptibility model. With this, we were able to extract a phase shift of up to $0.15 \times \pi$ caused by the surrounding atoms at low density. Because of the mentioned losses due to Rb deposit on the waveguide surface, we did not further increase the density to avoid condensation on the chip. This experiment was performed in the vacuum chamber setup with relatively poor temperature control and this chip did not have a protection coating such that we kept the reservoir temperature well below the chamber temperature.

Coupling to ring resonators

In the next step, we investigated the interaction of thermal Rb atoms with photonic ring resonators in view of potential scalable atom-cavity systems. Our first attempts have been unsuccessful, since increased transmission losses after Rb exposure caused the resonances to disappear. An additional 9 nm thick Al_2O_3 protection coating enabled us to study these devices subsequently, although with residual round trip attenuation. By

varying the chip temperature, we could thermally tune a ring resonance of a resonator with 80 µm radius to the Rb D_2 transition and observe coupling of the atoms to the resonant mode. An entire frequency scan of the ring resonance was performed to characterize the interaction between the atoms and the ring mode at different positions of the ring resonance. Thereby, the influence of both real and imaginary part of the vapor's complex refractive index was observed in the transmission spectra, which were again very well reproduced with the effective susceptibility method.

We further studied the saturation behavior of the atoms when coupled to the ring mode. A power dependent measurement series revealed no substantial lowering of the saturation threshold in case of a resonant ring, compared to an off-resonant ring (essentially the bus waveguide). Therefore the intensity buildup in the ring and hence the coupling strength were negligible in this device. This is explained by the remaining losses due to Rb on the ring surface and the relatively large mode volume of this resonator, which was chosen for a reasonable temperature tunability.

Following up on this, we discussed the performance of the ring resonator in the context of cavity QED, where a cooperativity parameter of $C \approx 10^{-3}$ and a critical photon number of $n_0 \approx 1.3$ have been determined. Clearly, this system is far from being in the critical coupling regime. Therefore, we also discussed the feasibility to achieve strong coupling with thermal atoms and integrated photonic structures with the outcome, that the extremely small mode volume of photonic crystal cavities could provide a coupling strength large enough to surpass the dephasing caused by the atomic motion.

Slot waveguides

The investigation of slot waveguides turned out to be quite complex but likewise very educative. We designed devices with varying slot widths, with the intention to change the intensity of the waveguide mode inside each individual slot, thereby altering the coupling strength to the atoms. Transmission spectra of the Rb D_2 line have been recorded for each device and the line shape parameters have been extracted from the corresponding Voigt fits. We witnessed variations in the line shifts, line widths and amplitudes which were deviating from our original expectations.

To gain a better understanding of the actual behavior, a Monte Carlo simulation has been developed, which accounts for the motion of the atoms around the specific waveguide geometry. We included the original cross sectional dimension of the devices obtained from FIB/SEM measurements from which we also learned, that some of the slots were not fully developed or not existing at all. Casimir–Polder potentials and modified atomic decay rates have been calculated for the individual structures which we incorporated into the simulation as well. For the limiting cases of a single strip waveguide and a fully developed slot waveguide this model adequately reproduced the line shifts and line widths of the measured transmission spectra. However, there was

a discrepancy between experiment and simulations for the incompletely developed devices. We have discussed several reasons these deviations, but could not draw definite conclusions yet as there are still a couple of uncertainties left. These include, i.a., the exact dimensions of the structures and their surface conditions, the ad- and desorption dynamics and the role of Rb deposits and how they affect the mode profiles, the Casimir–Polder potentials and the surface dipole electric fields.

Furthermore, we have investigated atom-atom interaction at high densities within the sub-wavelength confinement of these waveguides. The interaction manifests itself in a line broadening and shift which both increase linearly with the atomic density. The line broadening can be attributed to self broadening and its magnitude is in agreement with the one observed in a comparable selective reflection experiment. However, the magnitude of the line shift is not consistent with the prevailing theory on dipole-dipole interactions and needs further clarification.

Two-photon spectroscopy

Using a two photon transition to the Rb $5D_{3/2}$ level, we performed evanescent spectroscopy with two counter-propagating modes in a waveguide. The similar wavelengths of the probe and coupling fields resulted in a reduced Doppler width of the two-photon signal. A residual line width of $\sim 2\pi \times 860\,\mathrm{MHz}$ in comparison to the full Doppler line width of $\sim 2\pi \times 1300\,\mathrm{MHz}$ was determined. The width of the observed feature is still dominated by transit time broadening and distortion of the line shape due to atom-surface interactions. A further consequence of the atom-surface interactions is a red shift of $-2\pi \times 90\,\mathrm{MHz}$ of the entire resonance. This shift is larger than the one observed in the D_2 spectra, since the excitation scheme here involves the higher lying $5D_{3/2}$ level, which is more sensitive to the presence of the dielectric surface. The asymmetric two-photon feature could be reproduced by Monte Carlo simulations of the three level system including the Casimir–Polder potentials for each involved energy level, although with a discrepancy in the absolute line shift.

Outlook

After exploring the fundamental properties of this new type of atom-light interface, there are still many challenges to be addressed in this system. Likewise, the large potential of this approach indicates towards a multitude of exciting and revealing future experiments.

Silicon photonics

At this time, the experiment is undergoing a change with respect to the material of the photonic circuits. While the experiments performed in this thesis were based on Si_3N_4 structures, the performance of silicon (Si) photonics in combination with Rb vapor will be investigated with the next chip generation. In the field of integrated optics, a huge effort is put into the research on Si photonics [197], driven by the idea of monolithic integration with the existing CMOS[7] technology. Hence, a wide variety of devices with extraordinary quality compared to other material systems is available. Since Si is not transparent for 780 nm light, a different strategy has to be implemented to interface Rb atoms with the guided mode. The current idea is to populate the $5P_{3/2}$ level with a free space pump laser via the D_2 line and probe the $5P_{3/2} \rightarrow 4D_{5/2}$ transition at 1529 nm for which Si is transparent, see Figure 8.4 a). First proof of principle experiments based on total internal reflection inside a Si waver bonded to a vapor cell approved the feasibility of this approach. An exemplary absorption signal of the 1529 nm probe light transmitted through the waver from this experiment is shown in Figure 8.4 b).

Besides the benefits to be gained from the established Si photonics community, the 1529 nm transition wavelength of the probe light is also at the edge between the telecommunication S-band and C-band[8] such that potential devices would be readily compatible with the existing global fiber network infrastructure.

Another advantage of this approach lies in the refractive index of Si ($n \sim 3.5$) which is larger than for Si_3N_4 ($n \sim 2$). This enables stronger light confinement and hence larger coupling strength. The coupling strength is even further increased by the nearly two times larger dipole matrix element of the $5P_{3/2} \rightarrow 4D_{5/2}$ transition ($d = 10.63\, a_0 e$

[7] Abbreviation for complementary metal-oxide-semiconductor, the current technology used in microprocessors and other digital electronic circuits.

[8] S-band: 1460 nm to 1530 nm; C-band: 1530 nm to 1565 nm [198].

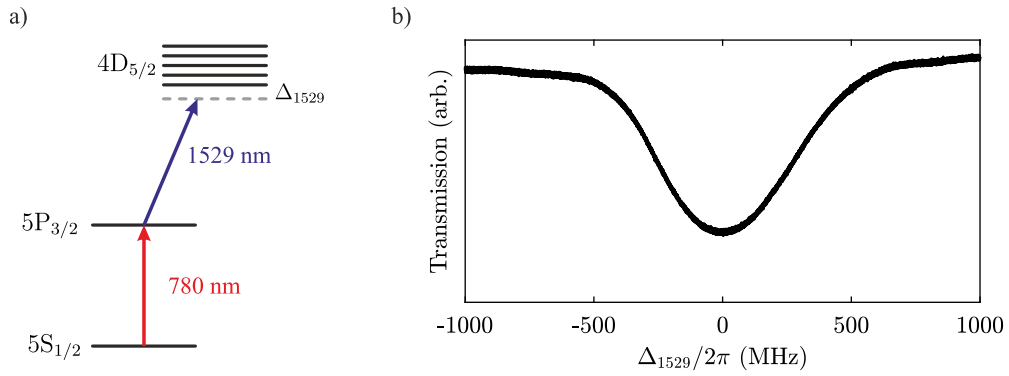

Figure 8.4: Two-photon spectroscopy using a Si waver bonded to a Rb vapor cell. a) Level scheme for the excitation. The $5P_{3/2}$ level is pumped with a free space 780 nm beam, while the 1529 nm light propagates in the Si and is scanned over the $5P_{3/2} \rightarrow 4D_{5/2}$ transitions. b) The signal shows absorption of the evanescent infrared light. The line width is Doppler- and transit time broadened and contains a series of hyperfine transitions.

[199]) compared to the D_2 transition ($d = 5.96\, a_0 e$ [199]). These points are especially interesting in view of potential cavity QED experiments.

Diminishing Rb induced transmission losses

In all experiments so far, we witnessed increased transmission losses after exposing the waveguide structures to Rb vapor, even with an Al_2O_3 protection coating, albeit to a lesser extent. This issue needs to be addressed, particularly if high quality factor cavities are to be built.

Choosing different core materials or protection layers seem the most obvious things to try. Potentially even different atomic or molecular species. Switching to silicon photonics might improve this situation. However, *if* ionic bonding of the Rb atoms to the oxygen atoms of the waveguide surface and the metallic properties of the adlayer are responsible for the losses, on has to be aware that Si develops a native oxide layer at ambient conditions [200] just as it is the case for Si_3N_4. Even on clean Si surfaces, alkali adsorption leads to metalization of the surface [201], which might cause residual ohmic losses.

Clearly, a way more thorough understanding of the underlying surface physics and chemistry than the present one are necessary in order to identify an efficient solution. This involves systematic studies of the actual attenuation mechanism as well as potential desorption strategies.

Increasing the interaction time

Probing thermal atoms on a sub-micron scale naturally implies very short interaction times which is detrimental for high precision sensing or cavity QED applications. A common technique to in increase the interaction time in clock or light storage experiments is the use of buffer gases and anti-relaxation coating. First estimations suggest however, that extremely high buffer gas pressures would be required in order to extend the stay of atoms in these small volumes, which would certainly involve additional decoherence effects. Nevertheless, one should analyze this topic more closely and consider various types of buffer gases. Perhaps, a balance can be found to minimize decoherence due to motion or collisions.

A different, maybe more promising strategy is proposed in reference [40]. Here, the small waveguide mode is converted to a larger one via a taper section and subsequently released into the vapor as a radiating mode via a grating coupler. Applying a reflection coating to the cell substrate opposite to the optical chip, one could couple the light which has passed the vapor back into a guided mode using the same (or a different) grating coupler. Thereby, one could increase the interrogation volume significantly while still keeping most of the benefits of integrated photonic circuits. Of course, this approach is not very useful with regards to strong coupling, however, it would allow narrower line widths for sensing and referencing applications. In this respect, the counter-propagating back reflected beam would also permit measurement of sub-Doppler features. Finally, the transformation into a free space mode and back might render possible to probe Rydberg atoms with integrated optics, which would broaden the range of sensing applications. It has been shown, that it is feasible to excite Rydberg atoms in a thermal vapor in less than a micron distance to a surface [34].

Appendix

A Wave equation

The wave equation determines the propagation of electromagnetic waves through a medium or in vacuum. It is derived from Maxwell's equations, which are given by [162]

$$\nabla \cdot \boldsymbol{E} = \frac{\rho}{\epsilon_0}\,, \tag{A.1a}$$

$$\nabla \cdot \boldsymbol{B} = 0\,, \tag{A.1b}$$

$$\nabla \times \boldsymbol{E} = -\frac{\partial \boldsymbol{B}}{\partial t} \tag{A.1c}$$

$$\nabla \times \boldsymbol{B} = \mu_0 \left(\boldsymbol{J} + \epsilon_0 \frac{\partial \boldsymbol{E}}{\partial t} \right)\,, \tag{A.1d}$$

where ρ is a charge density, $\boldsymbol{J}$ is a current density, ϵ_0 is the vacuum permittivity and μ_0 is the vacuum permeability. By substituting eq. (A.1a) into the curl of eq. (A.1c) we arrive at the inhomogeneous wave equation for the electric field

$$\left(\frac{1}{c^2} \frac{\partial^2}{\partial t^2} - \nabla^2 \right) \boldsymbol{E} = -\left(\frac{1}{\epsilon_0} \nabla \rho + \mu_0 \frac{\partial \boldsymbol{J}}{\partial t} \right)\,, \tag{A.2}$$

where $c^2 = (\epsilon_0 \mu_0)^{-1}$.

Vector and scalar potentials

The wave equation (A.2) has a rather complicated form which can be simplified by the introduction of electromagnetic potentials. The magnetic vector potential $\boldsymbol{A}$ and the electric scalar potential Φ are defined as [162]

$$\boldsymbol{B} = \nabla \times \boldsymbol{A} \tag{A.3a}$$

$$\boldsymbol{E} = -\nabla \Phi - \frac{\partial \boldsymbol{A}}{\partial t}\,. \tag{A.3b}$$

Using this definition, the four Maxwell equations reduce to two equations:

$$\nabla^2 \Phi + \frac{\partial}{\partial t} (\nabla \cdot \boldsymbol{A}) = -\frac{\rho}{\epsilon_0} \tag{A.4a}$$

$$\nabla^2 \boldsymbol{A} - \frac{1}{c^2} \frac{\partial^2 \boldsymbol{A}}{\partial t^2} - \nabla \left(\frac{1}{c^2} \frac{\partial \Phi}{\partial t} + \nabla \cdot \boldsymbol{A} \right) = -\mu_0 \boldsymbol{J}\,. \tag{A.4b}$$

The set of equations is now reduced, though they are still coupled and the wave term has a complicated form. However, the definition of the potentials in eq. (A.3) is not unique but there is gauge freedom. A common gauge condition for the calculation of electromagnetic waves is the Lorenz condition:

$$\nabla \cdot \boldsymbol{A} + \frac{1}{c^2}\frac{\partial \Phi}{\partial t} = 0\,. \tag{A.5}$$

Using eq. (A.5) with eq.s (A.4) leads to the uncoupled inhomogeneous wave equations for the potentials:

$$\left(\nabla^2 - \frac{1}{c^2}\frac{\partial^2}{\partial t^2}\right)\boldsymbol{A} = -\mu_0 \boldsymbol{J}\,, \tag{A.6a}$$

$$\left(\nabla^2 - \frac{1}{c^2}\frac{\partial^2}{\partial t^2}\right)\Phi = -\frac{\rho}{\epsilon_0}\,. \tag{A.6b}$$

We now consider a monochromatic polarization density given by $\boldsymbol{P}(\boldsymbol{r},t) = \boldsymbol{P}(\boldsymbol{r})e^{-\mathrm{i}\omega t}$. This time varying polarization creates an effective current density $\boldsymbol{J} = \partial \boldsymbol{P}/\partial t$ and eq. (A.6a) yields

$$\left(\nabla^2 + k^2\right)\boldsymbol{A} = \mathrm{i}\omega\mu_0 \boldsymbol{P}\,, \tag{A.7}$$

which is the (inhomogeneous Helmholtz) wave equation used in section 4.1 to calculate the electric field due to an arbitrary monochromatic dipole polarization.

From the Lorenz condition eq. (A.5) we get for monochromatic potentials

$$\nabla \cdot \boldsymbol{A} = \mathrm{i}\omega\mu_0\epsilon_0\Phi\,. \tag{A.8}$$

Using this result together with eq. (A.3b) we can calculate the electric field, once we know the vector potential:

$$\boldsymbol{E} = \mathrm{i}\omega\left(\boldsymbol{A} + \frac{1}{k^2}\nabla\nabla\cdot\boldsymbol{A}\right)\,. \tag{A.9}$$

A.1 Green's function for the wave equation

To calculate the electric field for the problem stated in section 4.1, we first need to solve the wave equation eq. (A.7). The method of Green's function will be used to accomplish this task. A detailed treatment can be found for example in the book on dyadic Green's functions by Tai [202].

Since the geometry under consideration is translationally invariant in the xy plane and we chose the plane of incidence to be the xz plane, the polarization can be separated

into a scalar function $P(z)$ and a phase factor $\exp(\mathrm{i}\alpha kx)$. Therefore the corresponding Green's function solves

$$\left(\frac{\partial^2}{\partial z^2} + k^2\right) G(z, z') = \delta(z - z') \exp(\mathrm{i}\alpha kx)\,, \tag{A.10}$$

and it must also satisfy the same boundary conditions as the solution $\boldsymbol{A}(\boldsymbol{r})$ does. In eq. (A.10), the Green's functions $G(z, z')$ can be interpreted as the influence experienced at point z caused by a point source at z'.

We can write eq. (A.10) away from the source point z' as

$$\left(\frac{\partial^2}{\partial z^2} + k^2\right) G(z, z') = 0\,, \qquad z > z'\,, \tag{A.11a}$$

$$\left(\frac{\partial^2}{\partial z^2} + k^2\right) G(z, z') = 0\,, \qquad z < z'\,. \tag{A.11b}$$

The general solution of equations (A.11) is

$$G(z, z') = c_1 \exp(\mathrm{i}kz) + c_2 \exp(-\mathrm{i}kz)\,. \tag{A.12}$$

Taking into account the angle dependence of the x and z components of the wave vector (determined by α and ξ, see section 4.1), we obtain for eq (A.10) the general solution

$$G(z, z') = \begin{cases} c_1 \exp(\mathrm{i}\xi kz + \mathrm{i}\alpha kx)\,, & z > z'\,, \\ c_2 \exp(-\mathrm{i}\xi kz + \mathrm{i}\alpha kx)\,, & z < z'\,, \end{cases} \tag{A.13}$$

where the Sommerfeld radiation condition [203] has been used to determine the proper sign in the exponential function. This condition mathematically excludes unphysical incoming waves from infinity and is given by

$$\lim_{z \to \pm\infty} \left(\pm \frac{\partial G}{\partial z} - \mathrm{i}kG\right) = 0\,. \tag{A.14}$$

To determine the coefficients c_1, c_2, we want to see how $G(z, z')$ behaves around the point z'. Formal integration of equations (A.11) gives in each case

$$\frac{\partial}{\partial z} G(z, z') = \Theta(z - z') + f(z)\,, \tag{A.15}$$

where $\Theta(z - z')$ is the Heaviside step function[1] and $f(z)$ is some continuous function. This means that the derivative of G must have a jump discontinuity at z', whereas

[1] The distributional derivative of $\Theta(z - z')$ is $\delta(z - z')$.

further integration of eq. (A.15) yields that G itself must be a continuous function. Hence we get the connection conditions at z':

$$\lim_{z\to z'_+} \frac{\partial G}{\partial z} - \lim_{z\to z'_-} \frac{\partial G}{\partial z} = 1\,, \quad \lim_{z\to z'_+} G - \lim_{z\to z'_-} G = 0\,. \tag{A.16}$$

Using these conditions leads to

$$G(z,z') = \begin{cases} \frac{1}{2\mathrm{i}\xi k} \exp(\mathrm{i}\xi k(z-z') + \mathrm{i}\alpha k x)\,, & z > z'\,, \\ \frac{1}{2\mathrm{i}\xi k} \exp(-\mathrm{i}\xi k(z-z') + \mathrm{i}\alpha k x)\,, & z < z'\,, \end{cases} \tag{A.17}$$

which can be combined to

$$G(z,z') = \frac{1}{2\mathrm{i}\xi k} \exp(\mathrm{i}\xi k|z-z'| + \mathrm{i}\alpha k x)\,. \tag{A.18}$$

B Asymmetric pseudo Voigt function

In a conventional vapor cell experiment, the line shape of the absorption profile is given by a Voigt function. However, if atom-surface interactions are relevant, the resonance frequency of an atom at a certain distance is shifted relative to the resonance frequency of an unperturbed atom. When we probe an ensemble of atoms close to a surface, the signal therefore will be a sum of many individual lines which are shifted according to the distribution of atoms-surface distances. This results in an asymmetric line shape which can be approximated by an asymmetric pseudo Voigt function, given by [165]:

$$S(\Delta) = (1-m)\sqrt{\frac{4\ln(2)}{\pi\gamma(\Delta)^2}}\exp\left[-\frac{4\ln(2)\Delta^2}{\gamma(\Delta)^2}\right] + \frac{m}{2\pi}\frac{\gamma(\Delta)}{\gamma(\Delta)^2/4+\Delta^2}\,. \tag{B.1}$$

Equation (B.1) constitutes a sum of a Gaussian and Lorentzian function where the line width is replaced by a sigmoidal function $\gamma(\Delta)$, introducing the asymmetry. The parameter m controls the relative weight of the Gaussian and Lorentzian contribution and $\gamma(\Delta)$ is given by

$$\gamma(\Delta) = \frac{2\gamma_0}{1+\exp[-a(\Delta-b)]}\,, \tag{B.2}$$

where γ_0 is the full width half maximum (FWHM) of S in the symmetric case, a is the asymmetry parameter and b shifts the sigmoid relative to zero detuning.

In order to get an estimate for the deviation between the pseudo Voigt approximation and the convoluted Voigt function we compare both versions in Figure B.1 and show the residuals. The deviations get the most significant when the Lorentzian and the Gaussian line widths become comparable, but are nevertheless in a reasonable range.

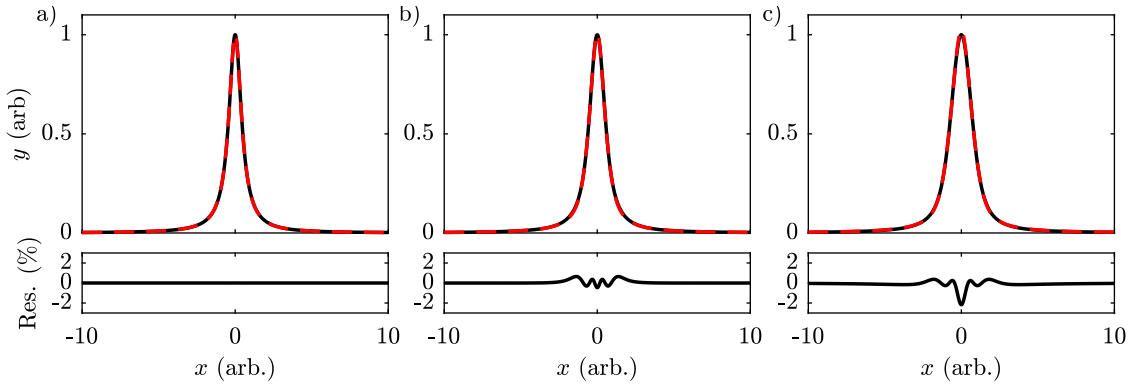

Figure B.1: Pseudo Voigt function (red dotted line) vs. real Voigt function (black solid line) for different ratios of Gaussian width Γ_G to Lorentzian width Γ_L. a) $\Gamma_G = 0$. b) $\Gamma_G = 1/2\Gamma_L$. c) $\Gamma_G = \Gamma_L$. The lower panels show the difference between the two functions.

C Further information on slot waveguides

This chapter provides some additional investigations on the slot waveguides presented in chapter 7.

C.1 Likelihood of higher order modes

We begin the discussion on higher order modes at the input section of the device. Light is coupled into a ridge waveguide (width $w = 650\,\text{nm}$ and height $h = 180\,\text{nm}$) via a grating coupler and guided to a Y splitter which transforms the ridge waveguide into a slot waveguide. The coupler, ridge waveguide and splitter are covered with a 800 nm thick layer of HSQ[1]. To determine which modes are guided in the ridge waveguide section we performed a mode analysis using COMSOL, the results of which are shown in Figure C.1 a). At a width of $w = 650\,\text{nm}$ the fundamental TE mode and the fundamental TM mode are supported with a large difference in the effective indices. Modes below the cutoff (determined by the refractive index of the substrate) are not guided but scattered into the substrate. The TE_1 mode is very close to the cutoff very likely not guided. Furthermore, the effective index separation to the TE mode is quite large, therefore the wavelengths required to fulfill the coupling condition at the grating are well separated for a fixed grating period and angle. Since the polarization of the input beam was set be parallel to the grating, the TM mode is highly suppressed at the grating coupler. Additionally, the different effective index would require a different coupling angle or wavelength. Due to the polarization control of the input light and the separation of the waveguide modes in their effective index, it can be assumed that light is only coupled into the fundamental TE mode of the ridge waveguide.

The ridge waveguide is continuously transformed into a slot waveguide via a Y splitter with a length of 10 µm within the HSQ covered section. Effective indices of the supported modes of the uncovered slot section are shown in Figure C.1 b) where the cross sections inferred from the FIB/SEM analysis were taken into account. The devices with $w_\text{d} = 30\,\text{nm}$ and $w_\text{d} = 40\,\text{nm}$ which do not exhibit a slot support the fundamental TE mode, and much closer to cutoff, also the TM and TE_1 mode. For

[1]HSQ = Hydrogen silesquioxane.

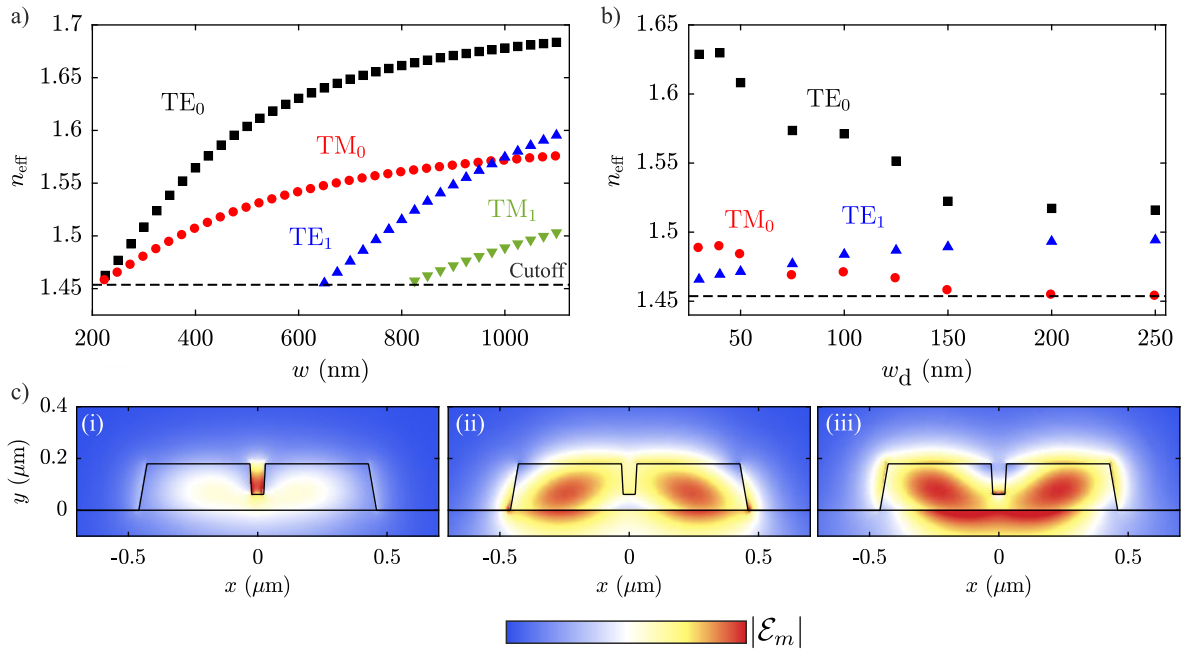

Figure C.1: Higher order modes in the investigated slot waveguide devices. a) Effective mode indices n_{eff} of supported modes in a $h = 180\,\text{nm}$ ridge Si_3N_4 waveguide with HSQ cladding versus core width w . b) Effective mode indices of supported modes in the slot region for the different design widths w_{d}. c) Mode profiles of supported modes in the $w_{\text{d}} = 75\,\text{nm}$ slot: fundamental TE (i) , TE_1 (ii), and fundamental TM mode (iii). For better visibility the field strength is individually normalized for the different modes.

$50\,\text{nm} \leq w_{\text{d}} \leq 125\,\text{nm}$ a slot is gradually developed until a fully opened slot is achieved for devices with $w_{\text{d}} \geq 150\,\text{nm}$. The mode profiles of the supported modes for the example of the $w_{\text{d}} = 75\,\text{nm}$ device are shown in Figure C.1 c). While the slot develops, the TE_0 mode is squeezed into the slot which leads to a lowering of the effective index. With the slot width growing further, the mode is more and more bound to the individual Si_3N_4 strips and approaches the TE_1 mode which has its field maxima within the two strips. At further separation of the strips, corresponding to a larger slot width, the TE_1 mode merges into two separated fundamental TE modes of the independent strip waveguides. The TM mode also gets split with increasing slot size and finally squeezed out of the structure into the substrate since the two strips separately do not support a TM mode.

Since we conclude from the above considerations that we most likely excite the fundamental TE mode in the ridge waveguide, we now consider how this mode is transformed during the splitting into the slot section. The effective mode index of the TE_0 mode gets continuously transformed from the value in the ridge waveguide to the value of

the TE mode in the slot section during the waveguide splitting, while there is a large mismatch to the higher order modes. Additionally polarization conversion would be required to transform the TE_0 mode into the TM_0 mode. To further analyze the mode conversion in the splitter section, we performed 3D simulations of this segment using COMSOL. First, it was confirmed that the mode profiles and effective indices after the splitter agree with the ones calculated for the slot section separately (Figure C.1 b) and c)). Additionally, the power conversion into the individual modes in the slot section was monitored. The results for the individual devices are shown in Figure C.2 a). The majority of the input mode power is converted into the TE_0 mode in the slot, whereas only a negligible fraction is converted into the higher order modes. The remaining losses are caused by either back-scattering, e.g., at the point where the waveguide splits and the end of the HSQ cover, or due to out-of-plane scattering losses. Hence, the transformation into TE_0 slot mode strengthens the argumentation above that this is the only relevant mode in the experiment.

Experimentally, multi-mode contributions can be identified in the transmission profile of the coupling structures of the photonic circuits. The grating period enables coupling between light falling on the coupler and a desired waveguide mode with a certain effective refractive index. The transmission spectrum of a particular waveguide mode shows a Gaussian-like profile in this configuration. Thus for a waveguide that only supports a single mode, only a single Gaussian-like peak is observed, when scanned over a wider wavelength range. In contrast, several of such peaks can be observed when multiple modes are supported in a waveguide. After the fabrication, transmission spectra were recorded over a wide spectral range using a broadband white light source in combination with a spectrometer. For the slot waveguide devices, the transmission peak of the grating couplers was centered at a wavelength of 781 nm with a width of ~ 30 nm. Only a single transmission peak was observed and within this peak and no beating between different modes was found. The transmission spectra have been compared to reference devices with single mode waveguides without a slot. No additional features in the spectra were found when comparing the slot devices to solid core single mode waveguides. Furthermore, ring resonator devices with identical grating couplers and the same width of the bus waveguide and resonator as the ridge waveguide above have been investigated. Here, only a single set of resonances was observed , indicating that light is coupled into a single mode only. In presence of further modes, additional sets of resonances with different free spectral range would have been observed owing to the difference in the effective mode indices.

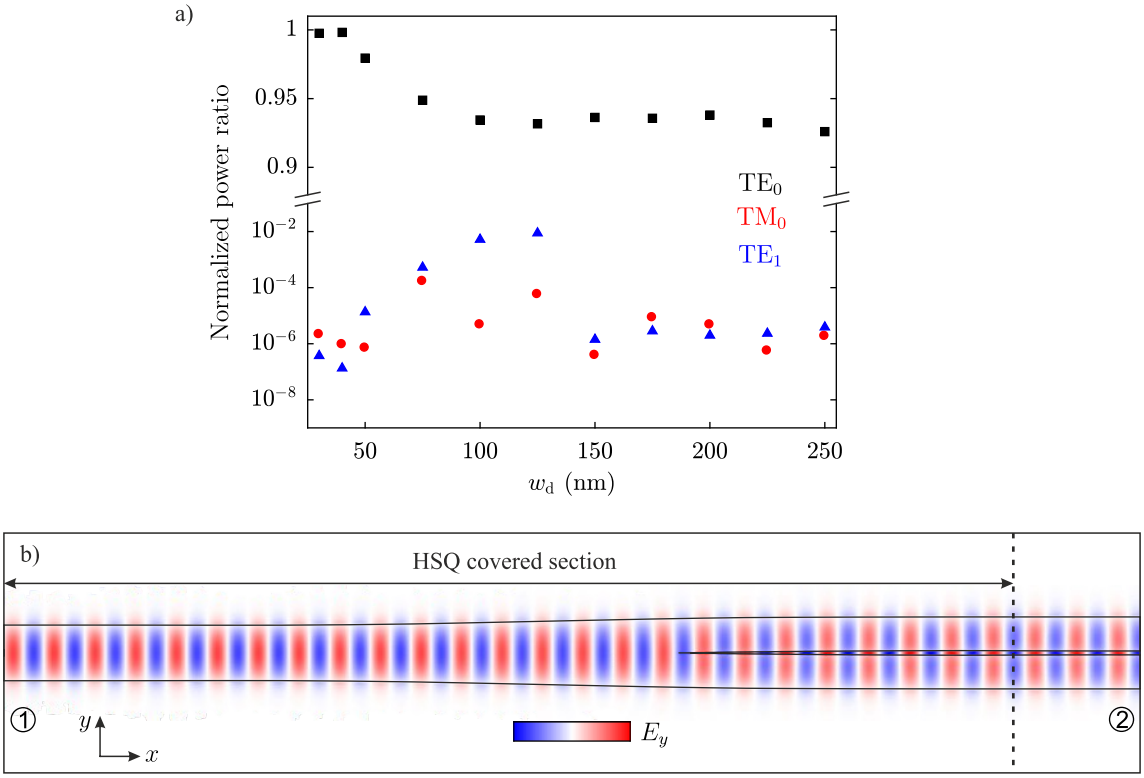

Figure C.2: Simulation of mode conversion at the Y splitter of a slot waveguide device. a) Power of the individual modes in the slot section normalized by the input power of the TE_0 mode in the ridge waveguide for the design slot widths w_d of the experiment. The ordinate is divided into a logarithmic scale in the lower part and a linear scale in the upper part. b) Top view of the simulation geometry for the $w_d = 75\,nm$ device showing the y-component of the electric field. At port 1 the TE_0 mode is excited in the ridge waveguide while the power of each mode in the slot section is monitored at port 2. The dashed line indicates the end of the region which covered with HSQ.

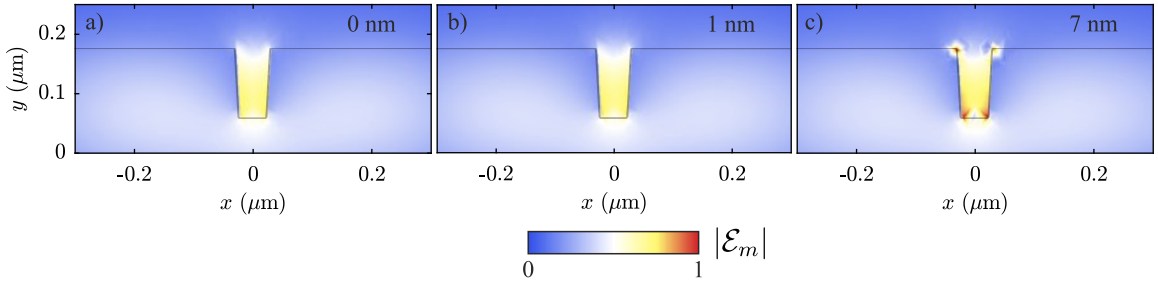

Figure C.3: Simulated mode profiles of the $w_\mathrm{d} = 75\,\mathrm{nm}$ slot waveguide covered with a metallic Rb layer. The plots show a close-up of the slot region. a) Without Rb. b) With a 1 nm and c) 7 nm thick Rb layer. The electric field amplitudes in all panels are normalized to the maximum field amplitude in c).

C.2 Influence of a metallic Rb layer on the mode profile

Here we investigate how a metallic Rb layer covering a slot waveguide changes its mode profile. As discussed in section 4.5, we have observed attenuation of the waveguide transmission when exposing them to an alkali vapor atmosphere. This might be caused by metallic Rb adsorbed on the waveguide surface. If this assumption is valid, a continuous Rb layer of $\sim$ 1 nm thickness could give rise to the typically observed transmission losses.

The mode profiles of the $w_\mathrm{d} = 75\,\mathrm{nm}$ slot waveguide have been simulated for a 3D geometry using COMSOl, were we have covered the entire waveguide surface with a metallic layer. This layer has been implemented via transition boundary conditions with the dielectric function of Rb at $\lambda = 780\,\mathrm{nm}$ [125]. A close up of the mode profiles in the slot region for different thicknesses of the Rb layer are shown in Figure C.3. Panel a) shows the original mode without any Rb coating for comparison. In panel b) a thickness of 1 nm was assumed, corresponding to the layer thickness required to explain the average transmission losses observed in our other experiments (see section 4.5). In this case, the mode does not significantly change compared to the uncovered waveguide. The relative difference in the electric field amplitude is $\sim 3\,\%$ in the corners of the waveguide and well below 1 % elsewhere. Finally, panel c) shows the mode profile for a 7 nm thick Rb layer. Here, the local field enhancement in the corners of the slot are obvious, however the major part of the mode profile does not change considerably.

These results suggest that a realistic Rb layer thickness of $\sim$ 1 nm cannot alter the mode profile of a slot waveguide sufficiently the discrepancies between experiment and Monte Carlo simulations reported in section 7.2 for the underdeveloped devices. A layer thickness of $\sim$ 7 nm, leading to noticeable modifications of the mode profile would involve additional transmission losses of $\sim 22\,\mathrm{dB}$ which was not observed in the experiment.

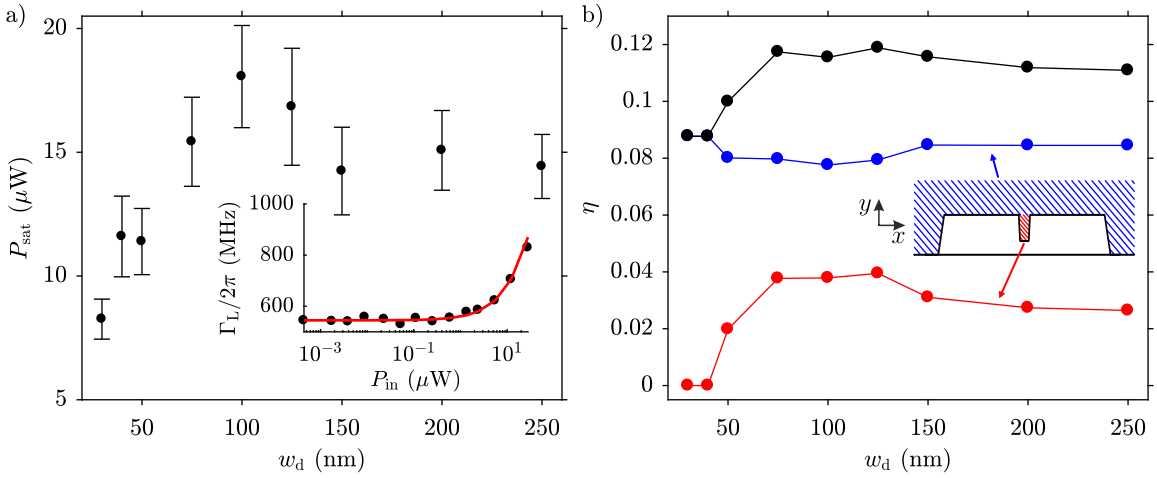

Figure C.4: Saturation in slot waveguides. a) Input power P_{sat} required to achieve saturation of the atomic transition versus design slot width w_d. The inset shows the power dependent Lorentzian line width obtained with the $w_d = 100\,\text{nm}$ slot. b) Fraction of the mode power in the atomic vapor region. The red curve corresponds to the inside of the slot, the blue curve corresponds to the remaining cladding and the black curve is the total power fraction outside the waveguide (slot + remaining cladding). The inset illustrates a cross section of the waveguide with color codes of the domains.

C.3 Slot width dependent saturation behavior

The key feature of slot waveguides is the large optical intensity inside the slot region which overlaps with the atomic vapor. One would therefore expect saturation of the atomic transition to occur at lower input power as compared to a conventional ridge waveguide, where the atoms only interact with the tail of the evanescent field.

To verify this assumption we recorded transmission spectra of the Rb D_2 line over a range of input powers for each slot waveguide with different design width w_d. By fitting these spectra with the model described in section 7.2.1 and assuming a Doppler width corresponding to the effective index we can extract the power dependent Lorentzian line width as shown in the inset of Figure C.4 a) for the example of the $w_d = 100\,\text{nm}$ device. We obtain the input power P_{sat} at which saturation occurs by fitting the function

$$\Gamma_L = \Gamma\sqrt{1 + P_{in}/P_{sat}} \tag{C.1}$$

to the data. Here, Γ is the initial line width, mostly determined by transit time broadening. The results of these fits for the individual devices are plotted in Figure C.4 a). The $w_d = 30\,\text{nm}$ device, which is actually a ridge waveguide and does not exhibit a slot, requires the lowest power to saturate the transition. Conversely, the $w_d = 100\,\text{nm}$ device with an almost completely developed slot requires the largest input power. This

behavior is in contrast to the previous assumption that saturation should be achieved with lower powers in a slot waveguide than in a ridge waveguide.

Further insight can be gained from Figure C.4 b) which shows simulation results of how the mode power is distributed within different domains of the waveguide geometry. Here, the quantity η is determined by

$$\eta = \frac{\iint\limits_{C} I_m(x,y)\mathrm{d}x\mathrm{d}y}{\iint\limits_{-\infty}^{+\infty} I_m(x,y)\mathrm{d}x\mathrm{d}y}\,, \tag{C.2}$$

where I_m is the intensity distribution of the mode and C denotes the area of a certain domain (see section 2.1 for details). The total power fraction in the vapor region, i.e. in the slot and the remaining cladding, is increasing when the slot starts to develop ($w_\mathrm{d} \geq 50\,\mathrm{nm}$) and slightly decreases for larger slot widths since the mode is stronger confined to the individual strips. Moreover, the separation into individual domains reveals that the power fraction in the slot is always smaller than in the remaining cladding. Therefore, the largest portion of the waveguide transmission signal, from which Γ_L is derived, originates from the outer cladding and only a small fraction from within slot. Also the transit time broadening in the narrow slots ($w_\mathrm{d} \leq 125\,\mathrm{nm}$) is larger than in the remaining cladding, which increases the saturation intensity inside the slot. Based on these facts, the trend of P_sat roughly following the inverse power fraction in the cladding (blue curve) appears reasonable. To separate the contributions from atoms inside the slot from the remaining cladding one could mask the individual strips with an SiO_2 cladding, as for example shown in Figure 6.9 d).

C.4 Surface dipole layer

As we have discussed in section 4.5, the initial layer of adsorbed alkali atoms on oxide surfaces is relatively strongly bonded. This bond is associated with a charge transfer between the adatom and the surface atom(s) resulting in a static surface dipole, see inset of Figure C.5 a). Atoms located in the electric field of these dipoles experience Stark shifts of their energy levels. The presence of such stray electric fields from polarized adsorbates has been observed in several experiments involving Rydberg atoms [166–168, 204].

The electric field strength at a given position depends on the magnitude of the surface dipole moment, which is determined by the nature of the chemical bond and the density of surface dipoles. For the slot waveguides examined in section 7.2, the outermost layer consists of Al_2O_3. To our knowledge, dipole moments for the Al_2O_3-Rb bond are not available in the literature, however for the SiO_2-Rb-bond a dipole moment

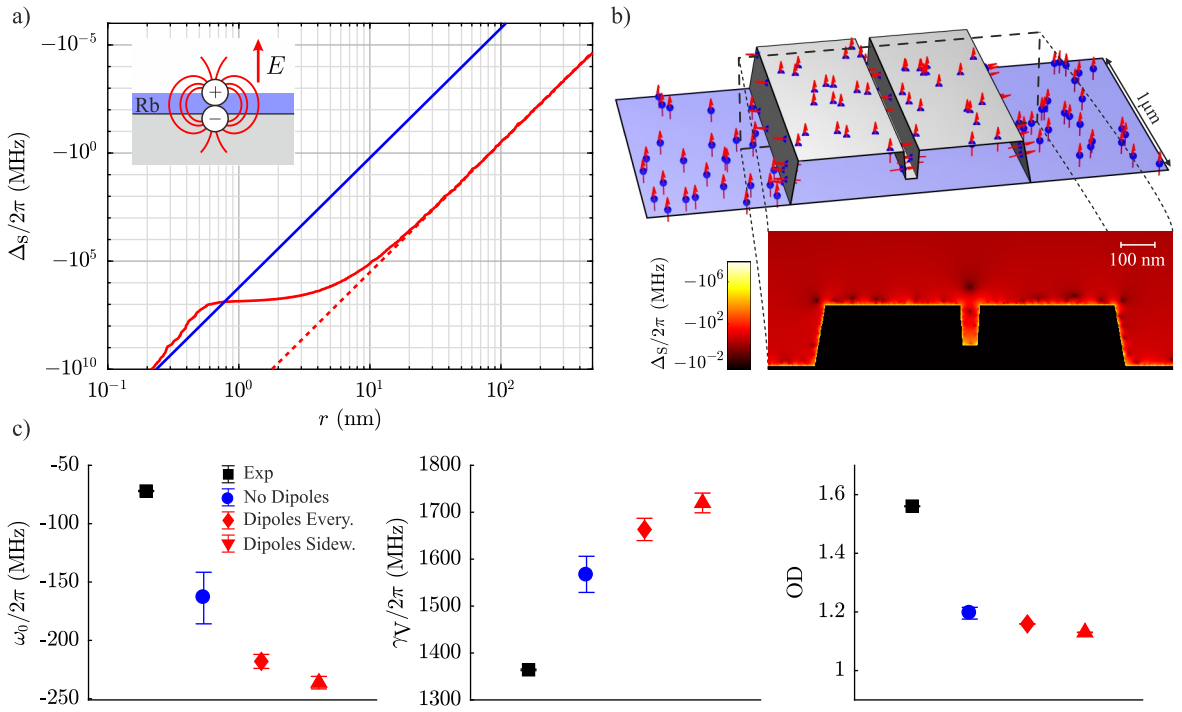

Figure C.5: Effects of surface dipole moments. a) Stark shift of the Rb D_2 levels at distance r caused by a single 10 D dipole (blue line) and an array of the same dipoles (red line) along the axis above the center dipole. b) Simulation of a random distribution of surface dipoles and the consequential Stark shift in a cut plane perpendicular to the $w_d = 75$ nm slot waveguide. c) Comparison of the frequency shift ω_0, line width γ_V and optical depth (OD) obtained from the experiment (black squares) and simulations without surface dipoles (blue circles), a uniform dipole distribution (red diamonds) and dipoles only on the sidewalls (red triangles).

on the order of $p_0 \approx 10\,\mathrm{D}^2$ has been determined both experimentally [166–168] and theoretically [166] in the limit of small surface coverage. With increasing coverage, the dipole moment of the individual bonds decreases due to the mutual interactions between the dipoles in the layer [205, 206], where the reduction of the dipole moment depends on the polarizability of the bond.

Atoms in the electric field of these dipoles experience a Stark shift of its energy levels. For the Rb D_2 transition the Stark shift is given by [207]

$$\Delta_S = -\frac{1}{2}\Delta\alpha_0 E^2 - \frac{1}{2}\alpha_2 E^2 \left(m_j^2 - \frac{5}{4}\right) , \tag{C.3}$$

where $\Delta\alpha_0 = \alpha_0\left(5P_{3/2}\right) - \alpha_0\left(5S_{1/2}\right) = 0.134\,\mathrm{Hz/(V/cm)^2}$ is the D_2 scalar polarizability

[2] $1\,\mathrm{D} = 1\mathrm{Debye} \approx 3.335\,64 \times 10^{-30}\,\mathrm{C\,m}$.

and $\alpha_2 = -0.0406\,\mathrm{Hz/(V/cm)^2}$ is the tensor polarizability of the $5P_{3/2}$ state [208]. The effect of a single dipole is shown by the blue line in Figure C.5 a), where a dipole moment of $p_0 = 10\,\mathrm{D}$ is assumed, according to the reported values for Rb on SiO_2. Despite the comparatively small polarizability of the Rb D_2 levels, the Stark shift can get substantial for an atom-dipole distance below 10 nm. The range of the electric field increases in case of an array of surface dipoles as shown by the red curve in Figure C.5 a). Here, a patch of $10 \times 10\,\mathrm{nm}^2$ consisting of an array of 21×21 dipoles, roughly corresponding to the density of one mono layer[3] (ML) with $p_0 = 10\,\mathrm{D}$ is assumed. Interaction between the dipoles is neglected. For separations larger than the patch size ($r > 10\,\mathrm{nm}$), the atom "sees" a large dipole with a dipole moment of $21^2 \times 10\,\mathrm{D}$, showing the same $1/r^3$ scaling of the electric field, as the single dipole. If the distance to the surface is smaller than the extent of the patch, the situation becomes similar to a charged plane and the field gradient flattens until the distance is smaller than the separation of the dipoles where the total field is again dominated by the field of a single dipole.

The study the effect of a surface dipole layer on the atom-light interaction around a slot waveguide, we performed 3D Monte Carlo simulations for the $w_\mathrm{d} = 75\,\mathrm{nm}$ device with a random distribution of dipoles with a density of 0.1 ML, see Figure C.5 b). The dipole moment of each dipole is $p_0 = 10\,\mathrm{D}$ and is oriented perpendicular to the surface. Depolarization effects among the dipoles are not included since we do not know the polarizability of the Al_2O_3-Rb bond. Since the sidewalls of the waveguide exhibit a higher roughness than the top surfaces due to the etching process, the effective area of the sidewalls is larger and could therefore accommodate a larger number of dipoles per unit length of the waveguide. Hence, we simulated two scenarios to examine whether an increased dipole density within the slot could lead to less signal contribution from the narrow slots as we observed in section 7.2.2: In the first case, the entire chip is covered with randomly distributed dipoles, in the second case only the sidewalls of the waveguide are occupied. Figure C.5 b) shows the Stark shift in a cut plane perpendicular to the waveguide corresponding to an electric field distribution of dipoles on the entire chip. In Figure C.5 c) we show the relevant parameters of the transmission spectrum when simulating the atom-light interaction around the $w_\mathrm{d} = 75\,\mathrm{nm}$ slot waveguide including surface dipoles and compare them to the experimental values and simulations without dipoles. The dipole field leads to an increased line shift and broadening which reduces the optical depth (OD) for both scenarios.

The outcome of these simulations implies that surface dipoles in the considered configurations are not able to reduce the signal contribution from the slot region. Given that the measured shifts and line widths for the ridge waveguides and completely developed slots agree very well with the simulations including only Casimir–Polder potentials,

[3] The density of a mono layer of Rb is taken to be $\sigma_0 \approx (1.57 \times d_\mathrm{Rb}^2)^{-1} = 3.3 \times 10^6\,\mu\mathrm{m}^{-2}$, where $d_\mathrm{Rb} \approx 440\,\mathrm{pm}$ is the covalent diameter of Rb [132] and the factor of 1.57 accounts for a hexagonal close-packed arrangement of the atoms [209].

strong electric fields do not seem to be present in the experiment. However, these findings do not rule out the presence of adsorbed Rb on the Al_2O_3 surface. As mentioned above, for increasing coverage of the surface, electrostatic interaction between the adatoms will result in a depolarization of the adatom which was not taken into account in our simulation. Furthermore, in reference [127] it was reported that cesium atoms on Al_2O_3 usually do not form a uniform layer but rather metallic clusters which nucleate at defect sites. Additional adatoms on top of the initially bonded atoms are subject to little charge transfer, thus reducing the dipole strength.

D Chip Designs

Several photonic chips have been investigated during the course of this work. The material compositions of the chips of which experimental result are reported in this thesis are given in the following sections. Additionally, CAD drawings of the relevant devices are shown.

D.1 NGE08

The substrate of the NGE08 chip consists of a 1.1 mm thick 1.5 in diameter fused silica vacuum window which was mounted into a CF flange via a metal seal (Helicoflex) and connected to a UHV chamber.

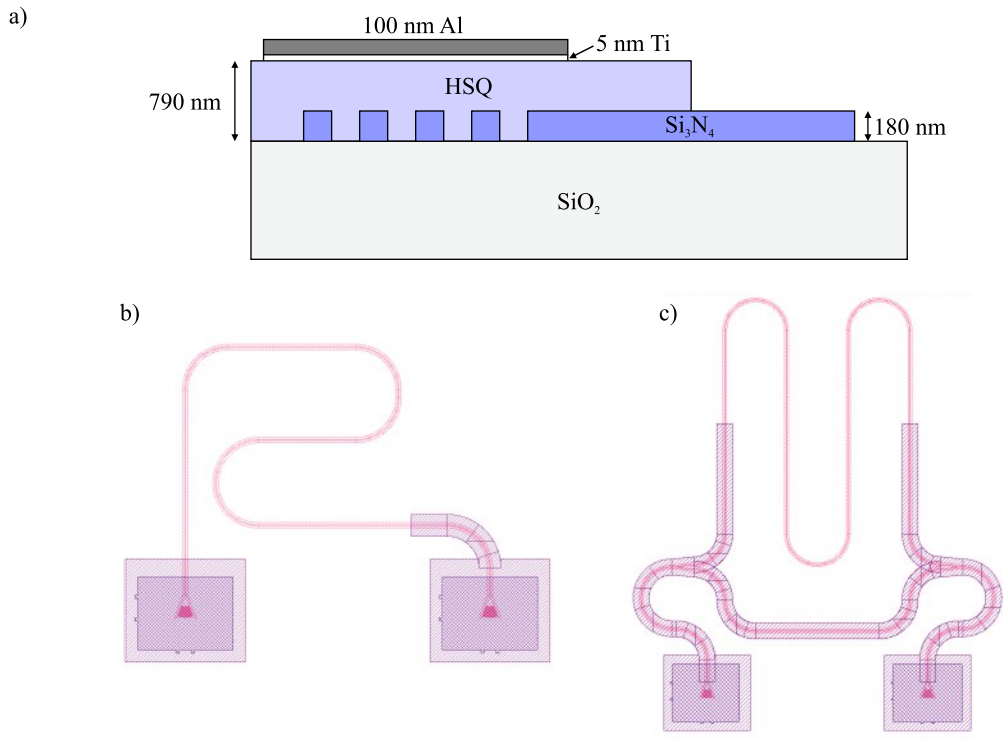

Figure D.1: NGE08 chip. a) Layer composition. b) Ridge waveguide. c) MZI.

D.2 NGJ21

The substrate of the NGJ21 chip consists of a 1.1 mm borosilicate window. This chip was mainly used for measurements on ring resonators. However, this chip did not yet have an Al_2O_3 coating, such that losses due to Rb on the waveguide surface caused the resonances to disappear.

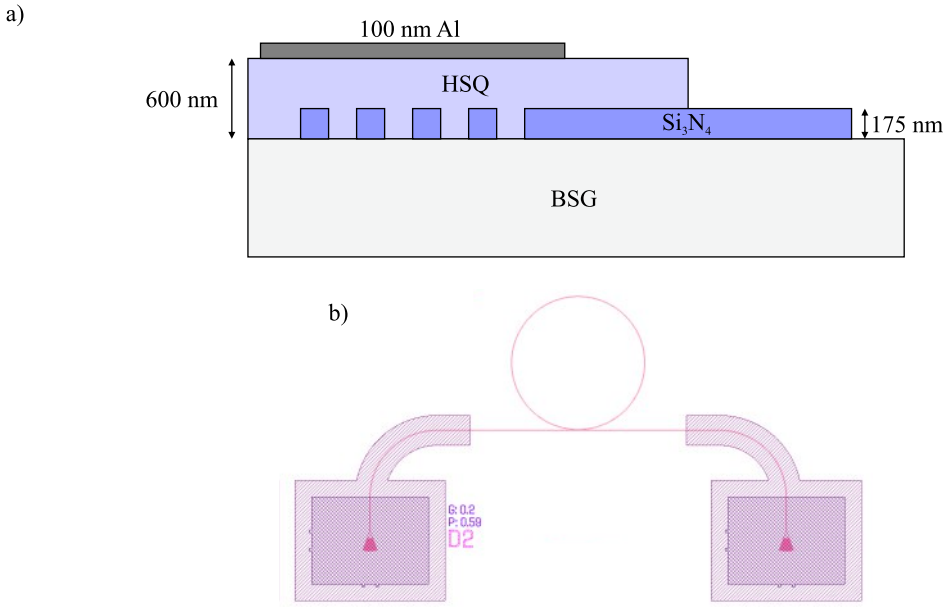

Figure D.2: NGJ21 chip. a) Layer composition. b) Ring resonator.

D.3 NGJ30-II

The substrate of the NGJ30-II chip consists of a 1.1 mm borosilicate window. It was the first chip with an Al_2O_3 protection coating. It was therefore mainly used to perform measurements on some ring resonators and two-photon spectroscopy.

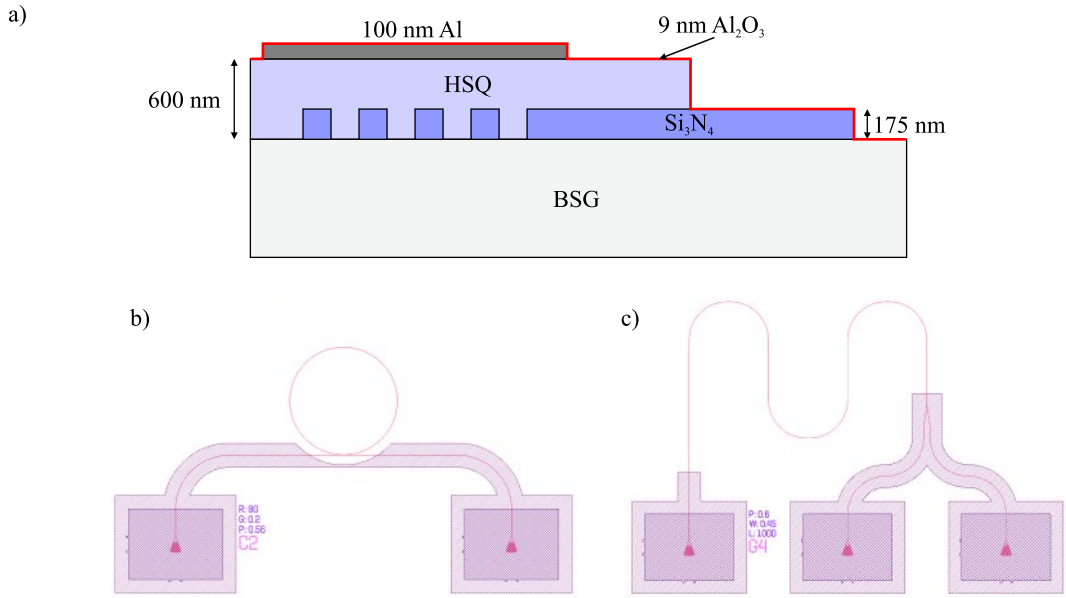

Figure D.3: NGJ30-II chip. a) Layer composition. b) Ring resonator. c) Two-photon spectroscopy circuit.

D.4 NGJ35

The substrate of the NGJ35 chip consists of a 1.1 mm borosilicate window. This chip has been used for slot waveguide measurements.

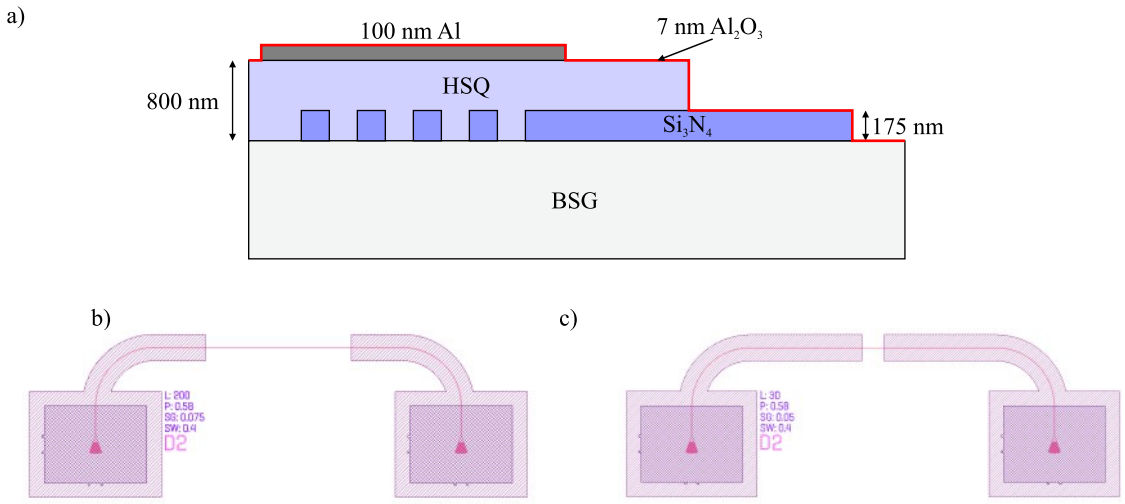

Figure D.4: NGJ35 chip. a) Layer composition. b) Slot waveguide with long interaction region ($l = 200\,\mu m$). c) Slot waveguide with short interaction region ($l = 30\,\mu m$).

Bibliography

[1] Camparo, J. "The rubidium atomic clock and basic research". Physics Today **60**, 11 (2007).

[2] Re, E. & Ruggieri, M. "Satellite Communications and Navigation Systems". Springer US (2008).

[3] Riehle, F. "Frequency Standards: Basics and Applications". Wiley (2006).

[4] Mohapatra, A. K., Bason, M. G., Butscher, B., Weatherill, K. J. & Adams, C. S. "A giant electro-optic effect using polarizable dark states". Nat. Phys. **4**, 11, 890 (2008).

[5] Sedlacek, J. A. *et al.* "Microwave electrometry with Rydberg atoms in a vapour cell using bright atomic resonances". Nat. Phys. **8**, 11, 819 (2012).

[6] Sedlacek, J. A., Schwettmann, A., Kübler, H. & Shaffer, J. P. "Atom-Based Vector Microwave Electrometry Using Rubidium Rydberg Atoms in a Vapor Cell". Phys. Rev. Lett. **111**, 063001 (2013).

[7] Horsley, A. *et al.* "Imaging of relaxation times and microwave field strength in a microfabricated vapor cell". Phys. Rev. A **88**, 063407 (2013).

[8] Horsley, A., Du, G.-X. & Treutlein, P. "Widefield microwave imaging in alkali vapor cells with sub-100 μm resolution". New J. Phys. **17**, 11, 112002 (2015).

[9] Kominis, I., Kornack, T., Allred, J. & Romalis, M. "A subfemtotesla multichannel atomic magnetometer". Nature **422**, 6932, 596 (2003).

[10] Budker, D. & Romalis, M. "Optical magnetometry". Nat. Phys. **3**, 4, 227 (2007).

[11] Bison, G., Wynands, R. & Weis, A. "Dynamical mapping of the human cardiomagnetic field with a room-temperature, laser-optical sensor". Opt. Express **11**, 8, 904 (2003).

[12] Bison, G. *et al.* "A room temperature 19-channel magnetic field mapping device for cardiac signals". Appl. Phys. Lett. **95**, 17, 173701 (2009).

[13] Alem, O. *et al.* "Fetal magnetocardiography measurements with an array of microfabricated optically pumped magnetometers". Phys. Med. Biol. **60**, 12, 4797 (2015).

[14] Xia, H., Ben-Amar Baranga, A., Hoffman, D. & Romalis, M. "Magnetoencephalography with an atomic magnetometer". Appl. Phys. Lett. **89**, 21, 211104 (2006).

[15] Wyllie, R., Kauer, M., Wakai, R. T. & Walker, T. G. "Optical magnetometer array for fetal magnetocardiography". Opt. Lett. **37**, 12, 2247 (2012).

[16] Shah, V. K. & Wakai, R. T. "A compact, high performance atomic magnetometer for biomedical applications". Phys. Med. Biol. **58**, 22, 8153 (2013).

[17] Boto, E. *et al.* "A new generation of magnetoencephalography: Room temperature measurements using optically-pumped magnetometers". NeuroImage **149**, 404 (2017).

[18] Schmidt, J. *et al.* "An optogalvanic gas sensor for nitric oxide based on Rydberg excitations". arXiv preprint arXiv:1801.09453 (2018).

[19] Donley, E. A. *et al.* "Nuclear quadrupole resonances in compact vapor cells: The crossover between the NMR and the nuclear quadrupole resonance interaction regimes". Phys. Rev. A **79**, 013420 (2009).

[20] Kitching, J., Knappe, S. & Donley, E. A. "Atomic Sensors - A Review". IEEE Sens. J **11**, 9, 1749 (2011).

[21] Löw, R. & Pfau, T. "Magneto-optics: Hot atoms rotate light rapidly". Nat. Photonics **3**, 4, 197 (2009).

[22] Müller, M. M. *et al.* "Room-temperature Rydberg single-photon source". Phys. Rev. A **87**, 5, 053412 (2013).

[23] Balabas, M. V., Karaulanov, T., Ledbetter, M. P. & Budker, D. "Polarized Alkali-Metal Vapor with Minute-Long Transverse Spin-Relaxation Time". Phys. Rev. Lett. **105**, 070801 (2010).

[24] Hosseini, M., Sparkes, B. M., Campbell, G., Lam, P. K. & Buchler, B. C. "High efficiency coherent optical memory with warm rubidium vapour". Nat. Commun. **2**, 174 (2011).

[25] Michelberger, P. *et al.* "Interfacing GHz-bandwidth heralded single photons with a warm vapour Raman memory". New J. Phys. **17**, 4, 043006 (2015).

[26] Weller, L. *et al.* "Optical isolator using an atomic vapor in the hyperfine Paschen–Back regime". Opt. Lett. **37**, 16, 3405 (2012).

[27] Zentile, M. A., Whiting, D. J., Keaveney, J., Adams, C. S. & Hughes, I. G. "Atomic Faraday filter with equivalent noise bandwidth less than 1 GHz". Opt. Lett. **40**, 9, 2000 (2015).

[28] Uhland, D. *et al.* "Single molecule DNA detection with an atomic vapor notch filter". EPJ Quantum Technology **2**, 1, 20 (2015).

[29] Portalupi, S. L. *et al.* "Simultaneous Faraday filtering of the Mollow triplet sidebands with the Cs-D1 clock transition". Nat. Commun. **7**, 13632 (2016).

[30] Knappe, S. *et al.* "A microfabricated atomic clock". Appl. Phys. Lett. **85**, 9, 1460 (2004).

[31] Balabas, M., Budker, D., Kitching, J., Schwindt, P. & Stalnaker, J. "Magnetometry with millimeter-scale antirelaxation-coated alkali-metal vapor cells". JOSA B **23**, 6, 1001 (2006).

[32] Maurice, V. *et al.* "Microfabricated vapor cells filled with a cesium dispensing paste for miniature atomic clocks". Appl. Phys. Lett. **110**, 16, 164103 (2017).

[33] Baluktsian, T. *et al.* "Fabrication method for microscopic vapor cells for alkali atoms". Opt. Lett. **35**, 12, 1950 (2010).

[34] Kübler, H., Shaffer, J. P., Baluktsian, T., Löw, R. & Pfau, T. "Coherent excitation of Rydberg atoms in micrometre-sized atomic vapour cells". Nat Photon **4**, 112 (2010).

[35] Keaveney, J. *et al.* "Cooperative Lamb Shift in an Atomic Vapor Layer of Nanometer Thickness". Phys. Rev. Lett. **108**, 173601 (2012).

[36] Kitching, J. *et al.* "Microfabricated atomic frequency references". Metrologia **42**, 3, S100 (2005).

[37] Knappe, S., Alem, O., Sheng, D. & Kitching, J. "Microfabricated optically-pumped magnetometers for biomagnetic applications". In Journal of Physics: Conference Series. IOP Publishing (2016), vol. 723, p. 012055.

[38] Schwindt, P. D. *et al.* "Chip-scale atomic magnetometer". Appl. Phys. Lett. **85**, 26, 6409 (2004).

[39] Sheng, D. *et al.* "A microfabricated optically-pumped magnetic gradiometer". Appl. Phys. Lett. **110**, 3, 031106 (2017).

[40] Kitching, J. *et al.* "NIST on a Chip: Realizing SI units with microfabricated alkali vapour cells". In Journal of Physics: Conference Series. IOP Publishing (2016), vol. 723, p. 012056.

[41] Stern, L., Desiatov, B., Goykhman, I. & Levy, U. "Nanoscale Light-Matter Interactions in Atomic Cladding Waveguides". Nat Commun **4**, 1548 (2013).

[42] Stern, L. & Levy, U. "Transmission and time delay properties of an integrated system consisting of atomic vapor cladding on top of a micro ring resonator". Opt. Express **20**, 27, 28082 (2012).

[43] Stern, L., Zektzer, R., Mazurski, N. & Levy, U. "Enhanced light-vapor interactions and all optical switching in a chip scale micro-ring resonator coupled with atomic vapor". Laser Photonics Rev. **10**, 6, 1016 (2016).

[44] Stern, L., Desiatov, B., Mazurski, N. & Levy, U. "Strong coupling and high-contrast all-optical modulation in atomic cladding waveguides". Nat. Commun. **8**, 14461 (2017).

[45] Hunsperger, R. G. "Integrated optics", vol. 4. Springer (1995).

[46] Onishi, T. *et al.* "Monolithically integrated 780-nm-band high-power and 650-nm-band laser diodes with real refractive index guided self-aligned structure". IEEE Photon. Technol. Lett. **13**, 6, 550 (2001).

[47] Klehr, A. *et al.* "High-power 894 nm monolithic distributed-feedback laser". Opt. Express **15**, 18, 11364 (2007).

[48] Krishnamoorthy, A. *et al.* "Vertical-cavity surface-emitting lasers flip-chip bonded to gigabit-per-second CMOS circuits". IEEE Photon. Technol. Lett. **11**, 1, 128 (1999).

[49] Krishnamoorthy, A. V. *et al.* "16 x 16 vcsel array flip-chip bonded to cmos vlsi circuit". IEEE Photon. Technol. Lett. **12**, 8, 1073 (2000).

[50] Geis, M. *et al.* "CMOS-compatible all-Si high-speed waveguide photodiodes with high responsivity in near-infrared communication band". IEEE Photon. Technol. Lett. **19**, 3, 152 (2007).

[51] Masini, G., Sahni, S., Capellini, G., Witzens, J. & Gunn, C. "High-speed near infrared optical receivers based on Ge waveguide photodetectors integrated in a CMOS process". Advances in Optical Technologies **2008** (2008).

[52] Ishikura, N. *et al.* "Photonic crystal tunable slow light device integrated with multi-heaters". Appl. Phys. Lett. **100**, 22, 221110 (2012).

[53] Dennis, T., Curtis, E., Oates, C. W., Hollberg, L. & Gilbert, S. L. "Wavelength references for 1300-nm wavelength-division multiplexing". J. Light. Technol. **20**, 5, 776 (2002).

[54] Zhao, K. & Wu, Z. "Evanescent wave magnetometer". Appl. Phys. Lett. **89**, 26, 261113 (2006).

[55] Kimble, H. J. "Strong interactions of single atoms and photons in cavity QED". Phys. Scr. **1998**, T76, 127 (1998).

[56] Haroche, S. & Raimond, J.-M. "Cavity quantum electrodynamics". Sci. Am. **268**, 54 (1993).

[57] Haroche, S. "Nobel Lecture: Controlling photons in a box and exploring the quantum to classical boundary". Rev. Mod. Phys. **85**, 1083 (2013).

[58] Kimble, H. J. "The quantum internet". Nature **453**, 1023 (2008).

[59] Cirac, J. I., Zoller, P., Kimble, H. J. & Mabuchi, H. "Quantum State Transfer and Entanglement Distribution among Distant Nodes in a Quantum Network". Phys. Rev. Lett. **78**, 3221 (1997).

[60] Duan, L.-M. & Kimble, H. J. "Scalable Photonic Quantum Computation through Cavity-Assisted Interactions". Phys. Rev. Lett. **92**, 127902 (2004).

[61] Vernooy, D. W., Furusawa, A., Georgiades, N. P., Ilchenko, V. S. & Kimble, H. J. "Cavity QED with high-Q whispering gallery modes". Phys. Rev. A **57**, R2293 (1998).

[62] Aoki, T. *et al.* "Observation of strong coupling between one atom and a monolithic microresonator". Nature **443**, 671 (2006).

[63] Tiecke, T. G. *et al.* "Nanophotonic quantum phase switch with a single atom". Nature **508**, 241 (2014).

[64] Goban, A. *et al.* "Atom–light interactions in photonic crystals". Nat Commun **5**, 3808 (2014).

[65] Javanainen, J., Ruostekoski, J., Li, Y. & Yoo, S.-M. "Shifts of a Resonance Line in a Dense Atomic Sample". Phys. Rev. Lett. **112**, 113603 (2014).

[66] Javanainen, J. & Ruostekoski, J. "Light propagation beyond the mean-field theory of standard optics". Opt. Express **24**, 2, 993 (2016).

[67] Javanainen, J., Ruostekoski, J., Li, Y. & Yoo, S.-M. "Exact electrodynamics versus standard optics for a slab of cold dense gas". Phys. Rev. A **96**, 033835 (2017).

[68] Peyrot, T. *et al.* "The Collective Lamb Shift of a Nanoscale Atomic Vapour Layer within a Sapphire Cavity". arXiv:1801.01773 (2018).

[69] Almeida, V. R., Xu, Q., Barrios, C. A. & Lipson, M. "Guiding and confining light in void nanostructure". Opt. Lett. **29**, 11, 1209 (2004).

[70] Blum, K. "Density Matrix Theory and Applications". Springer US (1996).

[71] Mølmer, K., Castin, Y. & Dalibard, J. "Monte Carlo wave-function method in quantum optics". J. Opt. Soc. Am. B **10**, 3, 524 (1993).

[72] Cohen-Tannoudji, C., Dupont-Roc, J. & Grynberg, G. "Atom-photon interactions: basic processes and applications". Wiley-VCH (1998).

[73] Demtröder, W. "Laser Spectroscopy: Basic Concepts and Instrumentation". Springer Berlin Heidelberg (2002).

[74] Chardonnet, C., Guernet, F., Charton, G. & Bordé, C. J. "Ultrahigh-resolution saturation spectroscopy using slow molecules in an external cell". Appl. Phys. B **59**, 3, 333 (1994).

[75] Liu, J.-M. "Photonic devices". Cambridge University Press (2009).

[76] Philipp, H. R. "Optical Properties of Silicon Nitride". J. Electrochem. Soc. **120**, 2, 295 (1973).

[77] Malitson, I. H. "Interspecimen Comparison of the Refractive Index of Fused Silica". J. Opt. Soc. Am. **55**, 10, 1205 (1965).

[78] Suhara, T. & Nishihara, H. "Integrated optics components and devices using periodic structures". IEEE J. Quantum Electron. **22**, 6, 845 (1986).

[79] Waldhäusl, R. *et al.* "Efficient Coupling into Polymer Waveguides by Gratings". Appl. Opt. **36**, 36, 9383 (1997).

[80] VanLaere, F. *et al.* "Focusing Polarization Diversity Grating Couplers in Silicon-on-Insulator". J. Lightwave Technol. **27**, 5, 612 (2009).

[81] Zaoui, W. S. *et al.* "Bridging the gap between optical fibers and silicon photonic integrated circuits". Opt. Express **22**, 2, 1277 (2014).

[82] Somekh, S., Garmire, E., Yariv, A., Garvin, H. L. & Hunsperger, R. G. "Channel Optical Waveguides and Directional Couplers in GaAs–Imbedded and Ridged". Appl. Opt. **13**, 2, 327 (1974).

[83] Soldano, L. B. & Pennings, E. C. M. "Optical multi-mode interference devices based on self-imaging: principles and applications". J. Lightwave Technol. **13**, 4, 615 (1995).

[84] Izutsu, M., Nakai, Y. & Sueta, T. "Operation mechanism of the single-mode optical-waveguide Y junction". Opt. Lett. **7**, 3, 136 (1982).

[85] Barclay, P. E., Srinivasan, K., Painter, O., Lev, B. & Mabuchi, H. "Integration of fiber-coupled high-Q SiNx microdisks with atom chips". Appl. Phys. Lett. **89**, 13, 131108 (2006).

[86] Daldosso, N. *et al.* "Fabrication and optical characterization of thin two-dimensional Si_3N_4 waveguides". Materials Science in Semiconductor Processing **7**, 4, 453 (2004).

[87] Gruhler, N. *et al.* "High-quality Si_3N_4 circuits as a platform for graphene-based nanophotonic devices". Opt. Express **21**, 25, 31678 (2013).

[88] Daschner, R. *et al.* "Triple stack glass-to-glass anodic bonding for optogalvanic spectroscopy cells with electrical feedthroughs". Appl. Phys. Lett. **105**, 4, 041107 (2014).

[89] "Photon LaserOptik GmbH",Ludwigstrasse 13,63110 Rodgau.

[90] Daschner, R. "Addressable rubidium vapor cells for optical and electrical read-out of Rydberg excitations". Dissertation, Universität Stuttgart (2015).

[91] Nienhuis, G., Schuller, F. & Ducloy, M. "Nonlinear selective reflection from an atomic vapor at arbitrary incidence angle". Phys. Rev. A **38**, 5197 (1988).

[92] Schuller, F., Nienhuis, G. & Ducloy, M. "Selective reflection from an atomic vapor in a pump-probe scheme". Phys. Rev. A **43**, 443 (1991).

[93] Ducloy, M. & Fichet, M. "General theory of frequency modulated selective reflection. Influence of atom surface interactions". Journal de Physique II **1**, 12, 1429 (1991).

[94] Born, M. "Quantenmechanik der Stoßvorgänge". Z. Phys. **38**, 11, 803 (1926).

[95] Constanda, C. "Differential Equations". Springer International Publishing (2017).

[96] Buhmann, S. Y. "Dispersion Forces I". Springer Berlin Heidelberg (2012).

[97] Failache, H., Saltiel, S., Fichet, M., Bloch, D. & Ducloy, M. "Resonant van der Waals Repulsion between Excited Cs Atoms and Sapphire Surface". Phys. Rev. Lett. **83**, 5467 (1999).

[98] Lennard-Jones, J. E. "Processes of adsorption and diffusion on solid surfaces". Trans. Faraday Soc. **28**, 333 (1932).

[99] Casimir, H. B. G. & Polder, D. "The Influence of Retardation on the London-van der Waals Forces". Phys. Rev. **73**, 360 (1948).

[100] Buhmann, S. Y. "Dispersion Forces II". Springer Berlin Heidelberg (2012).

[101] Paulus, M., Gay-Balmaz, P. & Martin, O. J. F. "Accurate and efficient computation of the Green's tensor for stratified media". Phys. Rev. E **62**, 5797 (2000).

[102] Yurkin, M. A. & Hoekstra, A. G. "The discrete dipole approximation: an overview and recent developments". J. Quant. Spectrosc. Radiat. Transfer **106**, 1, 558 (2007).

[103] Le Kien, F. & Hakuta, K. "Slowing down of a guided light field along a nanofiber in a cold atomic gas". Phys. Rev. A **79**, 013818 (2009).

[104] Purcell, E. M. "Proceedings of the American Physical Society". Phys. Rev. **69**, 674 (1946).

[105] Khosravi, H. & Loudon, R. "Vacuum field fluctuations and spontaneous emission in the vicinity of a dielectric surface". In Proceedings of the Royal Society of London A: Mathematical, Physical and Engineering Sciences. The Royal Society (1991), vol. 433, pp. 337–352.

[106] Scheel, S. & Buhmann, S. Y. "Macroscopic QED-concepts and applications". Acta Phys. Slovaca **58**, 675 (2008).

[107] Lodahl, P., Mahmoodian, S. & Stobbe, S. "Interfacing single photons and single quantum dots with photonic nanostructures". Rev. Mod. Phys. **87**, 347 (2015).

[108] Creatore, C. & Andreani, L. C. "Quantum theory of spontaneous emission in multilayer dielectric structures". Phys. Rev. A **78**, 063825 (2008).

[109] Søndergaard, T. & Tromborg, B. "General theory for spontaneous emission in active dielectric microstructures: Example of a fiber amplifier". Phys. Rev. A **64**, 3, 033812 (2001).

[110] Chen, Y., Nielsen, T. R., Gregersen, N., Lodahl, P. & Mørk, J. "Finite-element modeling of spontaneous emission of a quantum emitter at nanoscale proximity to plasmonic waveguides". Phys. Rev. B **81**, 12, 125431 (2010).

[111] Gear, C. "Numerical initial value problems in ordinary differential equations". Prentice-Hall series in automatic computation. Prentice-Hall (1971).

[112] Knudsen, M. "Das Cosinusgesetz in der kinetischen Gastheorie". Ann. Phys. **353**, 24, 1113 (1916).

[113] Maxwell, J. "V. Illustrations of the dynamical theory of gases. Part I. On the motions and collisions of perfectly elastic spheres". Philos. Mag. **19**, 124, 19 (1860).

[114] Papoulis, A. & Pillai, S. U. "Probability, Random Variables, and Stochastic Processes". McGraw-Hill Higher Education, 4th ed. (2002).

[115] Comsa, G. & David, R. "Dynamical parameters of desorbing molecules". Surf. Sci. Rep. **5**, 4, 145 (1985).

[116] Bordo, V. G. & Rubahn, H.-G. "Two-photon evanescent-wave spectroscopy of alkali-metal atoms". Phys. Rev. A **60**, 1538 (1999).

[117] Bordo, V. G., Loerke, J. & Rubahn, H.-G. "Two-Photon Evanescent-Volume Wave Spectroscopy: A New Account of Gas-Solid Dynamics in the Boundary Layer". Phys. Rev. Lett. **86**, 1490 (2001).

[118] Grischkowsky, D. "Angular and velocity distribution of desorbed sodium atoms". Appl. Phys. Lett. **36**, 8, 711 (1980).

[119] Kusumoto, Y. "Reflection rules preserving molecular flow symmetry in an arbitrarily shaped pipe". Journal of Vacuum Science & Technology A: Vacuum, Surfaces, and Films **25**, 2, 401 (2007).

[120] Steinruck, H. P., Winkler, A. & Rendulic, K. D. "Angle-resolved thermal desorption spectra for CO and H_2 from Ni(111), Ni(110) and polycrystalline nickel". J. Phys. Condens. Matter **17**, 11, L311 (1984).

[121] Willigen, W. V. "Angular distribution of hydrogen molecules desorbed from metal surfaces". Phys. Lett. A **28**, 2, 80 (1968).

[122] Leuthäusser, U. "Kinetic theory of desorption: Energy and angular distributions". Eur. Phys. J. B **50**, 1, 65 (1983).

[123] Olivero, J. & Longbothum, R. "Empirical fits to the Voigt line width: A brief review". J. Quant. Spectrosc. Radiat. Transfer **17**, 2, 233 (1977).

[124] Ma, J., Kishinevski, A., Jau, Y.-Y., Reuter, C. & Happer, W. "Modification of glass cell walls by rubidium vapor". Phys. Rev. A **79**, 042905 (2009).

[125] Smith, N. V. "Optical Constants of Rubidium and Cesium from 0.5 to 4.0 eV". Phys. Rev. B **2**, 2840 (1970).

[126] Madey, T. E., Yakshinskiy, B. V., Ageev, V. N. & Johnson, R. E. "Desorption of alkali atoms and ions from oxide surfaces: Relevance to origins of Na and K in atmospheres of Mercury and the Moon". J. Geophys. Res. Planets **103**, E3, 5873 (1998).

[127] Brause, M. *et al.* "Cs adsorption on oxide films (Al_2O_3, MgO, SiO_2)". Surf. Sci. **383**, 2, 216 (1997).

[128] Raider, S. I., Flitsch, R., Aboaf, J. A. & Pliskin, W. A. "Surface Oxidation of Silicon Nitride Films". J. Electrochem. Soc. **123**, 4, 560 (1976).

[129] Li, T. K., Hirschfeld, D. A. & Brown, J. J. "Alkali corrosion resistant coatings for Si_3N_4 ceramics". J. Mater. Sci. **32**, 16, 4455 (1997).

[130] Fox, D. S. & Jacobson, N. S. "Molten-Salt Corrosion of Silicon Nitride: I, Sodium Carbonate". J. Am. Ceram. Soc. **71**, 2, 128 (1988).

[131] Maier, S. "Plasmonics: Fundamentals and Applications". Springer US (2007).

[132] Cordero, B. *et al.* "Covalent radii revisited". Dalton Trans. **21**, 2832 (2008).

[133] Slepkov, A. D., Bhagwat, A. R., Venkataraman, V., Londero, P. & Gaeta, A. L. "Diffusion and Redistribution of Rubidium in Hollow-Core Photonic Bandgap Fibers". In Conference on Lasers and Electro-Optics/International Quantum Electronics Conference. Optical Society of America (2009), p. IMC2.

[134] Burchianti, A. *et al.* "Reversible Light-Controlled Formation and Evaporation of Rubidium Clusters in Nanoporous Silica". Phys. Rev. Lett. **97**, 157404 (2006).

[135] Speight, J. G. *et al.* "Lange's handbook of chemistry", vol. 1. McGraw-Hill New York (2005).

[136] Woetzel, S. *et al.* "Lifetime improvement of micro-fabricated alkali vapor cells by atomic layer deposited wall coatings". Surf. Coat. Technol. **221**, 158 (2013).

[137] Karlen, S., Gobet, J., Overstolz, T., Haesler, J. & Lecomte, S. "Lifetime assessment of RbN_3-filled MEMS atomic vapor cells with Al_2O_3 coating". Opt. Express **25**, 3, 2187 (2017).

[138] Volk, C., Frueholz, R., English, T., Lynch, T. & Riley, W. "Lifetime and Reliability of Rubidium Discharge Lamps for Use in Atomic Frequency Standards". Tech. rep., Aerospace Corp El Segundo Ca Chemistry and physics lab (1984).

[139] Alasaarela, T. *et al.* "Reduced propagation loss in silicon strip and slot waveguides coated by atomic layer deposition". Opt. Express **19**, 12, 11529 (2011).

[140] Ritter, R. *et al.* "Atomic vapor spectroscopy in integrated photonic structures". Appl. Phys. Lett. **107**, 4, 041101 (2015).

[141] O'Brien, C., Anisimov, P. M., Rostovtsev, Y. & Kocharovskaya, O. "Coherent control of refractive index in far-detuned Λ systems". Phys. Rev. A **84**, 063835 (2011).

[142] Keaveney, J., Hughes, I. G., Sargsyan, A., Sarkisyan, D. & Adams, C. S. "Maximal Refraction and Superluminal Propagation in a Gaseous Nanolayer". Phys. Rev. Lett. **109**, 233001 (2012).

[143] Simmons, Z. J., Proite, N. A., Miles, J., Sikes, D. E. & Yavuz, D. D. "Refractive index enhancement with vanishing absorption in short, high-density vapor cells". Phys. Rev. A **85**, 053810 (2012).

[144] Ritter, R. *et al.* "Coupling thermal atomic vapor to an integrated ring resonator". New J. Phys. **18**, 10, 103031 (2016).

[145] Yariv, A. "Universal relations for coupling of optical power between microresonators and dielectric waveguides". Electron. Lett. **36**, 4, 321 (2000).

[146] Heebner, J. E., Wong, V., Schweinsberg, A., Boyd, R. W. & Jackson, D. J. "Optical transmission characteristics of fiber ring resonators". IEEE J. Quantum Electron. **40**, 6, 726 (2004).

[147] Rabus, D. G. "Ring Resonators: Theory and Modeling", Springer Berlin Heidelberg, Berlin, Heidelberg, pp. 3–40 (2007).

[148] Elshaari, A. W., Zadeh, I. E., Jöns, K. D. & Zwiller, V. "Thermo-Optic Characterization of Silicon Nitride Resonators for Cryogenic Photonic Circuits". IEEE Photon. J **8**, 3, 1 (2016).

[149] Burkhardt, P. J. & Marvel, R. F. "Thermal Expansion of Sputtered Silicon Nitride Films". J. Electrochem. Soc. **116**, 6, 864 (1969).

[150] Spillane, S. M. *et al.* "Ultrahigh-Q toroidal microresonators for cavity quantum electrodynamics". Phys. Rev. A **71**, 013817 (2005).

[151] Rempe, G., Thompson, R. J., Brecha, R. J., Lee, W. D. & Kimble, H. J. "Optical bistability and photon statistics in cavity quantum electrodynamics". Phys. Rev. Lett. **67**, 1727 (1991).

[152] Thompson, R. J., Rempe, G. & Kimble, H. J. "Observation of normal-mode splitting for an atom in an optical cavity". Phys. Rev. Lett. **68**, 1132 (1992).

[153] Zhu, Y. *et al.* "Vacuum Rabi splitting as a feature of linear-dispersion theory: Analysis and experimental observations". Phys. Rev. Lett. **64**, 2499 (1990).

[154] Gondarenko, A., Levy, J. S. & Lipson, M. "High confinement micron-scale silicon nitride high Q ring resonator". Opt. Express **17**, 14, 11366 (2009).

[155] Vučković, J., Lončar, M., Mabuchi, H. & Scherer, A. "Design of photonic crystal microcavities for cavity QED". Phys. Rev. E **65**, 016608 (2001).

[156] Khan, M., Babinec, T., McCutcheon, M. W., Deotare, P. & Lončar, M. "Fabrication and characterization of high-quality-factor silicon nitride nanobeam cavities". Opt. Lett. **36**, 3, 421 (2011).

[157] Alton, D. *et al.* "Strong interactions of single atoms and photons near a dielectric boundary". Nat. Phys. **7**, 2, 159 (2011).

[158] Garcia-Fernandez, R. *et al.* "Optical nanofibers and spectroscopy". Appl. Phys. B **105**, 1, 3 (2011).

[159] Hendrickson, S. M., Lai, M. M., Pittman, T. B. & Franson, J. D. "Observation of Two-Photon Absorption at Low Power Levels Using Tapered Optical Fibers in Rubidium Vapor". Phys. Rev. Lett. **105**, 173602 (2010).

[160] Spillane, S. M. *et al.* "Observation of Nonlinear Optical Interactions of Ultralow Levels of Light in a Tapered Optical Nanofiber Embedded in a Hot Rubidium Vapor". Phys. Rev. Lett. **100**, 233602 (2008).

[161] Xu, Q., Almeida, V. R., Panepucci, R. R. & Lipson, M. "Experimental demonstration of guiding and confining light in nanometer-size low-refractive-index material". Opt. Lett. **29**, 14, 1626 (2004).

[162] Jackson, J. "Classical Electrodynamics". Wiley (2007).

[163] Rotenberg, N. *et al.* "Small slot waveguide rings for on-chip quantum optical circuits". Opt. Express **25**, 5, 5397 (2017).

[164] SEM images kindly provided by Prof. Wolfram Pernice, Institute of Physics, University of Muenster.

[165] Schmid, M., Steinrück, H.-P. & Gottfried, J. M. "A new asymmetric Pseudo-Voigt function for more efficient fitting of XPS lines". Surf. Interface Anal. **46**, 8, 505 (2014).

[166] Sedlacek, J. A. *et al.* "Electric Field Cancellation on Quartz by Rb Adsorbate-Induced Negative Electron Affinity". Phys. Rev. Lett. **116**, 133201 (2016).

[167] Tauschinsky, A., Thijssen, R. M. T., Whitlock, S., van Linden van den Heuvell, H. B. & Spreeuw, R. J. C. "Spatially resolved excitation of Rydberg atoms and surface effects on an atom chip". Phys. Rev. A **81**, 063411 (2010).

[168] McGuirk, J. M., Harber, D. M., Obrecht, J. M. & Cornell, E. A. "Alkali-metal adsorbate polarization on conducting and insulating surfaces probed with Bose-Einstein condensates". Phys. Rev. A **69**, 062905 (2004).

[169] Ziegler, J. I. *et al.* "3-D near-field imaging of guided modes in nanophotonic waveguides". Nanophotonics **6**, 187 (2017).

[170] Lewis, E. "Collisional relaxation of atomic excited states, line broadening and interatomic interactions". Phys. Rep. **58**, 1, 1 (1980).

[171] Marinescu, M. & Dalgarno, A. "Dispersion forces and long-range electronic transition dipole moments of alkali-metal dimer excited states". Phys. Rev. A **52**, 311 (1995).

[172] Stephen, M. "First-Order Dispersion Forces". J. Chem. Phys. **40**, 3, 669 (1964).

[173] Wang, P., Gallagher, A. & Cooper, J. "Selective reflection by Rb". Phys. Rev. A **56**, 1598 (1997).

[174] Chang, D. E., Ye, J. & Lukin, M. D. "Controlling dipole-dipole frequency shifts in a lattice-based optical atomic clock". Phys. Rev. A **69**, 023810 (2004).

[175] Kittel, C. "Introduction to Solid State Physics". Wiley (2004).

[176] Lorentz, H. A. "The Theory of Electrons". BG Teubner, Leipzig (1909).

[177] Maki, J. J., Malcuit, M. S., Sipe, J. E. & Boyd, R. W. "Linear and nonlinear optical measurements of the Lorentz local field". Phys. Rev. Lett. **67**, 972 (1991).

[178] Friedberg, R., Hartmann, S. & Manassah, J. "Frequency shifts in emission and absorption by resonant systems ot two-level atoms". Phys. Rep. **7**, 3, 101 (1973).

[179] Pellegrino, J. *et al.* "Observation of suppression of light scattering induced by dipole-dipole interactions in a cold-atom ensemble". Phys. Rev. Lett. **113**, 13, 133602 (2014).

[180] Jenkins, S. D. *et al.* "Optical Resonance Shifts in the Fluorescence of Thermal and Cold Atomic Gases". Phys. Rev. Lett. **116**, 183601 (2016).

[181] Jenkins, S. D. *et al.* "Collective resonance fluorescence in small and dense atom clouds: Comparison between theory and experiment". Phys. Rev. A **94**, 023842 (2016).

[182] Thorne, A., Litzén, U. & Johansson, S. "Spectrophysics: principles and applications". Springer Science & Business Media (1999).

[183] Sautenkov, V. A., van Kampen, H., Eliel, E. R. & Woerdman, J. P. "Dipole-Dipole Broadened Line Shape in a Partially Excited Dense Atomic Gas". Phys. Rev. Lett. **77**, 3327 (1996).

[184] Weller, L., Bettles, R. J., Siddons, P., Adams, C. S. & Hughes, I. G. "Absolute absorption on the rubidium D1 line including resonant dipole-dipole interactions". J. Phys. B **44**, 19, 195006 (2011).

[185] Krainov, V. P., Reiss, H. R. & Smirnov, B. M. "Radiative Transitions between Discrete States in Atomic Systems", Wiley-VCH Verlag GmbH & Co. KGaA, pp. 61–118 (2005).

[186] Corney, A. "Atomic and laser spectroscopy". Oxford science publications. Clarendon Press (1977).

[187] Kondo, R., Tojo, S., Fujimoto, T. & Hasuo, M. "Shift and broadening in attenuated total reflection spectra of the hyperfine-structure-resolved D_2 line of dense rubidium vapor". Phys. Rev. A **73**, 062504 (2006).

[188] Leegwater, J. A. & Mukamel, S. "Self-broadening and exciton line shifts in gases: Beyond the local-field approximation". Phys. Rev. A **49**, 146 (1994).

[189] Fleischhauer, M., Imamoglu, A. & Marangos, J. P. "Electromagnetically induced transparency: Optics in coherent media". Rev. Mod. Phys. **77**, 633 (2005).

[190] Autler, S. H. & Townes, C. H. "Stark Effect in Rapidly Varying Fields". Phys. Rev. **100**, 703 (1955).

[191] Gray, H. & Stroud, C. "Autler-Townes effect in double optical resonance". Opt. Commun. **25**, 3, 359 (1978).

[192] Shepherd, S., Fulton, D. J. & Dunn, M. H. "Wavelength dependence of coherently induced transparency in a Doppler-broadened cascade medium". Phys. Rev. A **54**, 5394 (1996).

[193] Urvoy, A. *et al.* "Optical coherences and wavelength mismatch in ladder systems". J. Phys. B **46**, 24, 245001 (2013).

[194] Petelski, T., Fattori, M., Lamporesi, G., Stuhler, J. & Tino, G. "Doppler-free spectroscopy using magnetically induced dichroism of atomic vapor: a new scheme for laser frequency locking". Eur. Phys. J. D **22**, 2, 279 (2003).

[195] Hipke, A. "Dual-Frequency-Comb Two-Photon Spectroscopy". Dissertation, LMU München (2016).

[196] Theodosiou, C. E. "Lifetimes of alkali-metal atom Rydberg states". Phys. Rev. A **30**, 2881 (1984).

[197] Jalali, B. & Fathpour, S. "Silicon photonics". J. Light. Technol. **24**, 12, 4600 (2006).

[198] Paschotta, R. *et al.* "Encyclopedia of laser physics and technology", vol. 1. Wiley-vch Berlin (2008).

[199] Safronova, M. S., Williams, C. J. & Clark, C. W. "Relativistic many-body calculations of electric-dipole matrix elements, lifetimes, and polarizabilities in rubidium". Phys. Rev. A **69**, 022509 (2004).

[200] Morita, M., Ohmi, T., Hasegawa, E., Kawakami, M. & Ohwada, M. "Growth of native oxide on a silicon surface". J. Appl. Phys. **68**, 3, 1272 (1990).

[201] Günster, J., Mayer, T. & Kempter, V. "Study of the electronic structure of Si (100) 2× 1 and CsSi (100) 2× 1 with MIES and UPS (HeI)". Surf. Sci. **359**, 1-3, 155 (1996).

[202] Tai, C.-T. "Dyadic Green functions in electromagnetic theory". Institute of Electrical & Electronics Engineers (IEEE) (1994).

[203] Sommerfeld, A. "Die Greensche Funktion der Schwingungslgleichung". Jahresbericht der Deutschen Mathematiker-Vereinigung **21**, 309 (1912).

[204] Epple, G., Joly, N., Euser, T., Russell, P. S. J. & Löw, R. "Effect of stray fields on Rydberg states in hollow-core PCF probed by higher-order modes". Opt. Lett. **42**, 17, 3271 (2017).

[205] Topping, J. "On the mutual potential energy of a plane network of doublets". Proc. Royal Soc. Lond. A **114**, 766, 67 (1927).

[206] Miller, A. "The variation of the dipole moment of adsorbed particles with the fraction of the surface covered". In Mathematical Proceedings of the Cambridge Philosophical Society. Cambridge University Press (1946), vol. 42, pp. 292–303.

[207] Krenn, C., Scherf, W., Khait, O., Musso, M. & Windholz, L. "Stark effect investigations of resonance lines of neutral potassium, rubidium, europium and gallium". Z. Phys. D **41**, 4, 229 (1997).

[208] Steck, D. A. "Rubidium 87 D Line Data". available online at http://steck.us/alkalidata (revision 2.1.5) (2015) (2015). 13 January 2015.

[209] Bouchiat, M., Guéna, J., Jacquier, P., Lintz, M. & Papoyan, A. "Electrical conductivity of glass and sapphire cells exposed to dry cesium vapor". Appl. Phys. B **68**, 6, 1109 (1999).